Imperial College London

Spirals, defects, rolls and bands;

Transitional Rayleigh-Bénard Poiseuille flows
using spectral/hp element methods

IMPERIAL COLLEGE LONDON
DEPARTMENT OF AERONAUTICS

Author:

Chi Hin Chan

Supervisor:

Professor Spencer J. Sherwin

Co-Supervisor

Professor Yongyun Hwang

April 2025

Ph.D. Thesis

Abstract

Contents

Chapter 1

Introduction

1.1 Living with fluids

1.2 Outline of the thesis

Chapter 2

Background

Rayleigh-Bénard-Poiseuille (RBP) flows describe the motion of fluids confined between two extended parallel plates, heated from below and cooled from the top, with an imposed pressure gradient. This system combines the two paradigmatic flow configurations; the classical Rayleigh-Bénard convection (RBC) and plane Poiseuille flow (PPF), driven by buoyancy and shear forces, respectively. In the limiting cases, the laminar solution can transition to convection rolls (RBC) or shear-driven turbulence (PPF), depending on whether buoyancy or shear forces dominate. While the transition away from the laminar state is well studied over the past decades, the transitional regime where both forces interact remains largely unexplored. For instance, do buoyancy forces promote the transition to shear-driven turbulence?; how does shear influence the convection? Understanding the transition to turbulence in this regime can have implications for applications such as the fabrication of thin uniform films in chemical vapour deposition [Evans and Greif, 1991, Jensen et al., 1991, Fauzi et al., 2018] and the cooling of electronic components [Kennedy and Zebib, 1983, Ray and Srinivasan, 1992]. [PRESENT RBP SETUP] The governing equations of the fluid motion in given by the Navier-Stokes equations with Boussinessq approximations,

$$\frac{\partial \mathbf{u}}{\partial t} + (\mathbf{u} \cdot \nabla)\mathbf{u} = -\frac{1}{\rho}\nabla p + \nu\nabla^2\mathbf{u} + g\beta(T - T_0). \tag{2.1}$$

'

$$\frac{\partial T}{\partial t} + (\mathbf{u} \cdot \nabla)T = \kappa\nabla^2 T, \tag{2.2}$$

$$\nabla \cdot \mathbf{u} = 0. \tag{2.3}$$

with arbitrary Dirichlet and Neumann boundary conditions.

$$\mathbf{u}_d, p_d, T_d \in \Omega_d, \quad \nabla\mathbf{u}_N, p_N, T_N \in \partial\Omega_N. \tag{2.4}$$

where $\mathbf{u}, T, p$ refers to the velocity, temperature and pressure fields, primitive variables that are not known a priori and ρ, ν, κ refers to the properties of the fluid, namely, density, kinematic viscosity and thermal diffusivity. For a given set of fluid properties ρ, ν, κ and geometric

properties L^*, t^*, u^* referring to an arbitrary length-, time- and velocity-scale, we are primarily interested in the behaviour of the fluid i.e if its laminar or turbulent. In other words, we have a six control parameters that describes a fluid flow of interest. To reduce the number of control parameters, we can suitably nondimensionalise the primitive variables by a velocity scale u_c, length scale, L_x, and time scale u_c/L_x, where u_c refers to the centreline velocity of a laminar flow and L_x refers to the streamwise length of the domain. The nondimensional equations with Boussienessq approximations are now given as,

$$\frac{\partial \mathbf{u}}{\partial t} + (\mathbf{u} \cdot \nabla)\mathbf{u} = -\nabla p + \frac{1}{Re}\nabla^2 \mathbf{u} + \frac{Ra}{Re^2 Pr}\theta \tag{2.5}$$

$$\frac{\partial \theta}{\partial t} + (\mathbf{u} \cdot \nabla)\theta = \frac{1}{RePr}\nabla^2 \theta, \tag{2.6}$$

$$\nabla \cdot \mathbf{u} = 0. \tag{2.7}$$

where $\mathbf{u}, \theta, p$ refers to the nondimensionalised velocity, temperature and presure. In this thesis, I am particularly focused on the transition behaviour of fluid flow driven by shear and bouyancy, addressing questions related to the onset of instabilities due to shear and buoyancy, and the (possible) competitive between shear and buoyancy driven instabilities. I would like to preface that while this thesis is dealing with onset of instabilities, it does not clearly indicate that the onset of such instabilities necessarily lead to turbulence, hence, for terminology sake, we shall be looking into transitional regimes where the fluid neither laminar nor turbulent. The main motivations are two-folds, both from an academic and applied point-of-view. Within academia, the onset and transition to turbulence in Rayleigh-Bénard Poiseuille flows remains poorly understand. Whilst there had been significant progress in our understand of transition to turbulence in independent setups, Rayleigh-Bénard convection and plane Poiseuille flows, their combined effects are not known. The thesis is structured into the follow, Chapter 1 is the introduction with literature review, chapter 2 methodology assosicated with the spectral/hp-element method, chapter 3 with results related to the the Rayleigh and Reynolds number sweep, chapter 4 with a specific focus on the bistability between spiral defect chaos and ideal straight rolls and finally chapter 5 with concluding remarks.

1. Academic motivation - flow structures, statistics, transition.

2. Application motivation - shear, heat transfer. Chip cooling, thin-film fabrication and atmospheric boundary layer.

2.1 Rayleigh-Bénard Poiseuille (RBP) flows

The non-dimensionalised parameters that govern RBP flow are the Rayleigh number, $Ra = \eta g d^3 \Delta T / \nu \kappa$, Reynolds number, $Re = W_c h / \nu$, Prandtl number, $Pr = \kappa / \nu$, and the aspect ratio of the flow domain, $\Gamma = L/2d$, where $\eta, g, \Delta T, \nu, \kappa, W_c, h, d, L$ are the thermal expansion

coefficient, acceleration due to gravity, temperature difference between the bottom and top wall, kinematic viscosity, thermal diffusivity, laminar centreline velocity, domain's half-depth, full-depth, length/span respectively.

? first investigated the primary instabilities of RBP flows, which can be determined by Re, Ra, Pr, and the planar x-z perturbations wavenumbers α, β respectively. For a given Ra and Pr, the neutral stability curves are limited by the development of Tollmien-Schlicting waves for $Re \geq Re_{TS} = 5772.22$ [**?**], and convection rolls within $0 \leq Re < Re_{TS}$. Convection rolls can be categorised based on their orientation to the mean flow, namely, longitudinal ($\alpha = 0, \beta \neq 0$), transverse ($\alpha \neq 0, \beta = 0$) and oblique rolls ($\alpha \neq 0, \beta \neq 0$). The linearised system governing the onset of longitudinal rolls is analogous to the linearised RBC system, with a critical Rayleigh number, $Ra_{\parallel} = Ra_{RB} = 1708.8$ and critical wavenumber, $\alpha_{\parallel} = \alpha_{RB} = 3.13$ [**??**], independent of Re and Pr. The critical Rayleigh number for oblique and transverse rolls matches that of RBC at $Re = 0$ due to horizontal isotropy, but increases as Re increases, depending on Pr, i.e., $Ra_{\perp} = f(Re, Pr)$ [**???**]. When spatially developing instabilities are considered, longitudinal rolls are always convectively unstable, and transverse rolls can become absolutely unstable [**???**]. Nonmodal stability analyses of subcritical RBP indicate that the optimal transient growth G_{max} increases gradually with Ra. The wavenumber of the optimal initial conditions, β_{max}, resembles that observed in shear flows [**?**], and gradually approaches the critical wavenumber of convection rolls, $\alpha_{\parallel}$, as Ra increases [**?**]. For $Re > 0$, the longitudinal rolls appear as the dominant primary instability [**?**]. Secondary stability analyses of longitudinal rolls reveal a wavy instability near $Re \sim 100$ [**?**], leading to wavy longitudinal rolls, which are convectively unstable [**??**]. The influence of finite lateral extensions in RBP flows on the stability of longitudinal and transverse rolls [**??**], as well as wavy rolls [**??**], has been reported. In finite streamwise extensions of RBP flows, the onset of convection rolls and the heat flux variations due to entrance effects have been investigated [**???**]. More recently, shear-driven turbulence can enhance heat fluxes in turbulent RBP flows [**??**]. RBP flows with sinusoidal heating and wavy walls have also been studied [**?**]. For an in-depth discussion of RBP flows, see the reviews by **?** and **?**.

1. Linear stability: Transverse, Oblique and Longitudinal rolls. (Gage 1968)

2. Convection stability of transverse rolls (Muller 1992)

3. Non-modal stability analysis of RBP flows (Jerome 2012)

4. Turbulent RBP (Pirozzolli 2015..)

2.2 Rayleigh-Bénard convection (RBC)

Rayleigh-Bénard convection serves as one of the paradigmatic fluid configuration for studying the dynamics of natural convection. It describes the motion of the fluid confined between two infinite-parallel plates simultaneously heated from below and cooled from the top. The two basic physical mechanisms that underpins RBC is the competition between buoyancy due to heating,

and resistance due to viscous forces. As the bottom plate is heated, the bottom layer fluid becomes more buoyant and tends to rise, while the colder top fluid layer is becomes relatively less buoyant and tends to sink, leading to an overturning of layers. Viscous forces between adjacent fluid parcels act to resist the motion. As buoyancy overcomes these viscous forces, the fluid layers overturn, leading to the onset of convection. One of the earliest experimental work is performed by Henri Bénard [Bénard, 1901], who observed the onset of hexagonal convection cells and characterised its properties. Later in 1917, Lord Rayleigh [Rayleigh, 1916] introduced a non-dimensional parameter, Ra, which now bears his name, that quantified the ratio between buoyancy and viscous forces,

$$Ra = \frac{\alpha g d^3 \Delta T}{\kappa \nu}, \tag{2.8}$$

where $Ra, \alpha, g, d\Delta T, \kappa, \nu$ refers to the Rayleigh number, volumetric thermal expansion of the fluid, gravitational constant, width and temperature difference between plates, thermal diffusivity and kinematic viscosity. When Ra exceeds a certain critical Rayleigh number Ra_c, the fluid configuration becomes unstable and convection motion ensures. The analysis from Rayleigh is the earliest record of performing linear stability analysis of a convection. It is worth to pointing out the subtle differences between Bénard's experiment, Rayleigh's linear stability analysis and the configuration of RBC in this thesis. Bénard's experiment considered a thin layer of fluid heated from below which is freely exposed to the air. Unbeknownst to him at that time, Marangoni (surface stresses) effects are important in thin layers of fluid. As the fluid layer becomes thinner, a heated fluid to decreases surface tension creating a dip on the interface, vice versa [?]. This is later known as Bénard-Marangoni (BM) convection. The convection patterns also depend on the top boundaries as demonstrated by ?, where hexgonal cells developed when the fluid is exposed to the free air (in the case of Bénard's experiment) while convection rolls formed when the fluid is bounded by a top plate [?]. Rayleigh's analysis considered a stress-free condition for the fluid velocity on the boundaries ($\frac{\partial u}{\partial n} = 0$), where analytical solutions are admittable, leading to the critical Rayleigh number of $Ra_c = \frac{27}{4}\pi^4 = 657.5$, and a critical wavelength of $q_c = \frac{\pi}{\sqrt{2}d}$. The critical Rayleigh number for no-slip (fixed) velocity at the plates was later computed by ?, which is given as $Ra_c = 1707.8$ and $q_c = 3.12/d$, in which the length of a single convection roll (l_{roll}) is close to the distance separating the plates, $l_{roll} = \frac{1}{2}\lambda = \frac{1}{2}\frac{2\pi d}{3.12} \approx 1.007d$. Furthermore, Ra_c and q_c are indepedent of Pr (Cite?). In this work, I will investigate RBC with no-slip velocity boundary conditions, herein referred to RBC for the rest of the thesis.

Slightly above the onset of convection, described using the reduced Rayleigh number $\varepsilon = (\frac{Ra}{Ra_c} - 1)$, a set of stable convection rolls near q_c are found to exist (CITATIONS?). The theoretical foundations of performing stability analysis using expansion in powers of amplitude (*weakly nonlinear analysis*) was considered by ?, in which he applied it to the problem of parallel shear flows. The important contribution was that slightly above the onset, stable stationary rolls are found within the range of $Ra > Ra_c + 3\eta(\alpha - \alpha_c)^2$, where $\eta = \frac{1}{2}\frac{\partial Ra}{\partial \alpha}|_{Ra_c}$. ? then extended the same technique to Rayleigh-Bénard convection, in which η was found to depend on Pr. Whilst this technique is useful in detailing the stability regions of stationary rolls, it
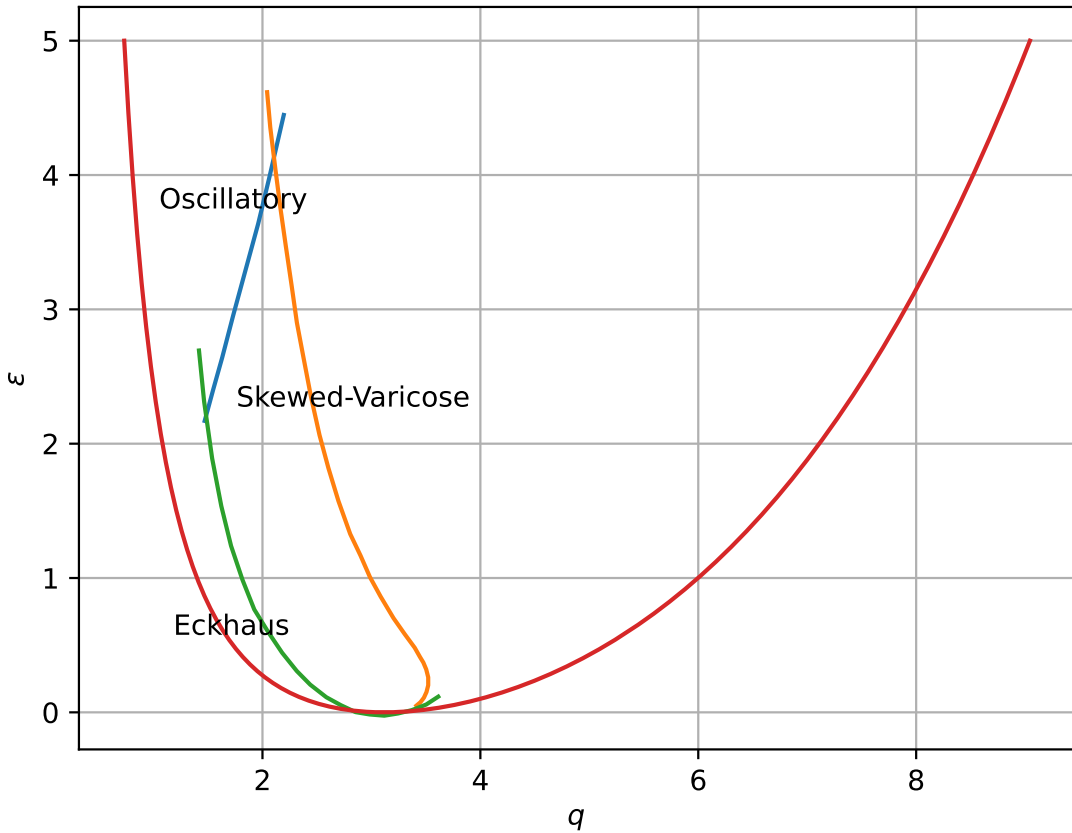
Figure 2.1: The Busse ballon describes the stability boundaries of ISRs in a $\varepsilon - q$ space. For larger wavenumbers, the instability mechanisms is described by the skewed-varicose (SV) instability. For smaller wavenumbers, the instability mechanism is described by the Eckhaus instability. For large ε, the instability is described by the onset of oscillatory instability. Busse balloon diigitised from [?] for $Pr \approx 1$

appears to be limited as it contradict some experiments in which time-dependent oscillatory rolls were discovered [??], which has been found to be a secondary instability of stationary convection rolls with complex eigenvalues. As noted by ?, the applicability of weakly nonlinear analysis is limited to small ε. This limitation is addressed by using directly computing the linear stability of saturated convection rolls computed based on a Galerkin truncation and a root-finding algorithm. The results from linear stability analysis led to the well known Busse balloon which described the stability boundary of the convection rolls in the two dimensional space of $\varepsilon - q$, known as the Busse balloon [??] (figure 2.1).

While the Busse balloon describes the stability boundaries of ISRs over a range of wavenumbers, predicting the wavenumber of an ISR state remains an central challenge [?]. Indeed, experimental investigations of RBC in moderate domain sizes ($\Gamma \geq 7$, where Γ refers to the domain's aspect ratio) in rectangular (straight rolls) and cylinderical (concentric rolls) domains showed that the wavenumbers are confined within the Busse balloon. As ε is was continously modified, the ISRs with wavenumbers that are now outside of the Busse balloon, rolls disloca-

tions and defects spontaneously nucleate, either increasing or decreasing the roll wavenumber, adhering to the the stability boundaries of the Busse balloon. The hysteretic nature of the system implies that the roll wavenumber of the ISRs strongly depends on the system's history [?].

To complicate the subject further, ISRs appear to be an exception rather than the rule [?] as multiple 'non-ISR' states, in the form os squares, travelling/stationary targets, giant rotating spirals and oscillatory convection patterns have been found over the years [???????]. For example, investigations of cylinderical RBC in small aspect-ratio revealed eight stationary statesand two oscillatory states. These findings were later supported by numerical experiments and bifurcation analyses.

1. Saturated States

2. Busse balloon for Pr = 1

3. Skew-varicose, Eckhaus, Cross-roll instabilities

4. Low Pr and high Pr.

5. What happens above the Busse balloon?

1. Statisitical description of spatial-temporal chaos (i.e correlation length, time etc..)

2. Challenge with quantifying the onset

2.3   Plane Poiseuille flows (PPf)

Plane Poiseuille flow belongs to a class of wall-bounded shear flows such as plane Couette flow (pCf), Hagen-Poiseuille flows (or pipe flows) and boundary layer flows. PPf describes the motion of a fluid confined between two infinite-parallel plates driven by a pressure-gradient across the streamwise direction, x. It is a canonical setup for investigating the laminar, transition and turbulent behaviour of the fluid when subjected to shear from the walls.

1. Onset of Tollmien-Schlicting waves

2. Challenges of TS waves, turbulence is subscritical

The critical Reynolds number for the onset of unstable infinitesimal perturbutations in plane Poiseuille flow (PPF) occurs at $Re_c = 5772.2$ [?]. However, turbulence have been consistly observed below Re_c, at $Re \sim 1000 - 2000$, suggesting that the onset of turbulence occurs subcritically. It is now known that at $Re \sim 1000 - 2000$, turbulence behaves intermittently, existing as oblique bands of turbulent and laminar regions. These turbulent-laminar bands have been also observed in shear flow systems such as Couette flow [?], Taylor-Couette flow [?], and pipe flow [?] (as puffs and slugs).

Over the past decade, research efforts have been dedicated to the study of turbulent-laminar bands. The wavelengths of 24° oblique bands been observed to occupy $20h$ at $1900 < Re < 1400$, and $40h$ at $1300 < Re < 800$, suggesting that band widths increases as Re decrease. Between $1300 < Re < 1400$ there appears to be bistable region between bands of both band-widths [?]. [?] observed turbulent-laminar oblique bands tilted by 23.7° at $Re = 1430$. [?] computed probabilities of turbulent-laminar band splitting and decay depending on Re. As Re increases the probability of band decay decreases, while as Re decreases the probability a band splitting event decreases. By extrapolating the estimated mean lifetimes of a splitting and decay event, the crossing point (i.e equal chance of identifying a splitting and decay event after a time-scale of $t = 3 \times 10^6$) occurs at $Re_{cross} \approx 925$, in other words, Re_{cross} acts as a critical Reynolds number.

At $Re \sim 1000 - 2000$, turbulent bands can either decay spontaneously, stabilising into a laminar state, or split, forming more bands whereby turbulent-laminar bands are sustained. The probability of decay and splitting lifetimes strongly depends on the domain size and Re. At $L_z = 100h$, the critical Reynolds number of $Re_{cr} \approx 965$ have been determined statistically, whereby decay and splitting lifetimes intersect more than 10^6 advective time units. It is worth to note that for $Re < Re_{cr}$, the probably of decay is higher than splitting events, vice versa.

We seek to investigate the influence of unstable stratification quantified by Rayleigh number Ra, on the behaviour tuburlent-laminar bands. The onset of convection occurs at a critical Rayleigh number of $Ra_c > 1708$, in the form of a pair of convection rolls. When aligned in the streamwise direction, the convection rolls are seemingly analogous to a pair of counter-rotating vortices, an optimal initial condition for transient growth. Our investigation naturally answers a few questions related to turbulent-laminar bands. For example, does the onset of turbulent-laminar bands, Re_{cr} decrease with increasing Ra? Do Ra-effects influence the structure of turbulent-laminar bands i.e band angle/width?

The answers to our research will have important implications Rayleigh-Bénard Poiseuille flows, ubiquitous in atmospheric, geophysical and engineering flows.

Chapter 3

Numerical Techniques

In this chapter, I will present the numerical methods relevant to this thesis.

3.1   Method of weighted residuals

The incompressible Navier-Stokes equations describe the time- and spatial-varying velocity field and pressure field. To represent the spatially-dependent velocity and pressure fields, spatial discretisation is performed using the spectral/hp element method. Other popular methods of spatial discretisation found in literature are the finite-difference methods, and finite-volume methods. SEMs belong to a general class of methods known as the method of weighted residual, a generic method for approximating a solution of a differential equation. The method of weighted residual will be described with a worked example as follows. Consider that the solution of a differential equation $u(x)$ can be represented as an infinite sum of *trial* functions (also known as basis functions, expansion functions, mode shapes).

$$u(x) = \sum_{i=0}^{\infty} \hat{u}_i \phi_i(x), \tag{3.1}$$

where $\phi_i(x)$ are the *trial* functions and $\hat{u}_i$ are the trial function coefficients to be determined. Typical examples of trial functions are, Fourier series e^{ikx}, Chebyshev polynomials $T(x)$ or Legendre series $L_g(x)$. The choice of basis expansions depends on the given problem. In the context fluid mechanics, the Fourier series can be used to represent isotropic turbulence with homogenenous (periodic) boundary conditions. In a channel flow, Fourier series are used in the homogenenous streamwise ad spanwise directions while Chebyshev or Legendre polynomials are used in the wall-normal direction. Consider equation 3.1 to be a solution of a 1-dimensional Poisson equation, bounded by the domain $\Omega \in [x_a, x_b]$,

$$\mathbb{L}u(x) \equiv \frac{\partial u(x)}{\partial x} - \lambda u(x) = f(x), \qquad x_a \leq x \leq x_b, \tag{3.2}$$

with the appropriate boundary conditions, and $\mathbb{L}$ refers to a linear differential operator. Note that equation 3.1 exactly satisfies the differential equation of 3.2 i.e $\mathbb{L}u(x) - f(x) = 0$. The

exact solution would require a computation of infinite basis coefficients $\hat{u}$ which is practically infeasible. Therefore, an approximate solution $u^\delta(x)$ is sought after by truncating an infinite number of basis expansions to a finite number,

$$u(x) \approx u^\delta(x) = \sum_{i=0}^{K} \hat{u}_i \phi_i(x), \tag{3.3}$$

where there is a finite number of K basis expansions. The approximate solution does not satisfy 3.2 exactly, leading to an 'error' known as a residual,

$$R(u^\delta(x)) = \mathbb{L}u^\delta(x) - f(x) \tag{3.4}$$

where $R(u^\delta)$ is the residual. The residual depends on the approximate solution $u^\delta(x)$, which varies in x. In other words, the error is non-zero and varies within Ω. Although equation 3.2 may not be satisfied everywhere in Ω, it is possible to apply some restrictions (conditions) on the residual so that it tends to zero by the choice of restrictions imposed. An approximate solution has $K + 1$ unknowns $(\hat{u}_0, ..., \hat{u}_K)$, hence, it is natural to impose $K + 1$ restrictions on the residual to form a determined system and the type of restriction defines the numerical method.

The method of weighted residual is a general method that allows for various types the restriction to be implemented. The method "nullifies" the residual by equating the inner product with a *test* function, $v_j(x)$ (also known as a weight function - hence the name 'weighted residual') to zero,

$$(v_j(x), R(u^\delta(x))) = \int_{x_a}^{x_b} v_j \, R(u^\delta(x)) \, \mathrm{d}x = 0, \qquad j = 0, ..., K. \tag{3.5}$$

The type of restriction on the residual is implemented through the choice of *test* function, v_j. For instance, for $v_j = \delta(x - x_j)$, the numerical method becomes the *collocation* method where the differential equation is satisfied on discrete points x_j. Table 3.1 shows the different forms of weight functions and its corresponding numerical method. The choice of *test* function is also commonly known as projection methods, i.e projecting (taking the inner product) the residual onto the *test* functions. It is worth to mention that the method of weighted residual merely describe the projection method but does not specify the type of *trial* functions used. The choice of *trial* functions used in *nektar++* will be elaborated in Section **??**.

Galerkin methods are commonly found in finite/spectral element solvers, used in *nektar++*. The Galerkin method belongs to a general class of weighted residual methods that assumes the *trial* functions take on the same form as the *test* functions (Table 3.1). To describe the method, a worked example is illustrated. The Galerkin method is appplied to solve the Poisson equation 3.2 with the following boundary conditions,

$$B^- = g^- \quad \text{at} \quad x = x_a, \qquad B^+ = g^+ \quad \text{at} \quad x = x_b \tag{3.6}$$

Weight Function	Type of method
$v_j(x) = \delta(x - x_j)$	Collocation
$v_j(x) = \begin{cases} 1 & \text{if } x \in \Omega_j \\ 0 & \text{if } x \notin \Omega_j \end{cases}$	Finite-Volume
$v_j(x) = \phi_j$	Galerkin
$v_j(x) = \frac{\partial R}{\partial \hat{u}_j}$	Least-squares

Table 3.1: Types of weight function

where B^-, B^+ are the boundary conditions which could be either Dirichlet, Neumann or Robin conditions. Equation 3.2 and 3.6 together forms a boundary value problem and is said to be in the *strong* [1] form. The Galerkin method assumes that the trial functions $\phi_i(x)$ satisfies equation 3.2 with homogeneous boundary conditions,

$$\phi_i(x_a) = \phi_i(x_b) = 0. \tag{3.7}$$

Next, the solution $u(x)$ is decomposed into a linear combination of $\tilde{u}(x)$ and $u^H(x)$,

$$u(x) = \tilde{u}(x) + u^H(x), \tag{3.8}$$

where $\tilde{u}(x)$ is any function that satisfy the boundary conditions assosciated with equation 3.6 and $u^H(x)$ is the homogeneous solution that satisfies the homogeneous boundary conditions - $B_H^-(x_a) = B_H^+(x_b) = 0$. The resulting problem for $u^H(x)$ becomes

$$\mathbb{L}u^H(x) - h(x) = 0, \qquad x_a \leq x \leq x_b, \tag{3.9}$$

where $h = f(x) - \mathbb{L}\tilde{u}(x)$. It is worth noting that the steps thus simply mathematical, and no approximation have been made. The solutions of $u(x) = \tilde{u}(x) - u^H(x)$ represented by an infinite expansions (equation 3.1) are exact. Next, the homogeneous solution $u^H(x)$ can be approximated by a finite expansion of *trial* functions,

$$u^H(x) \approx u^{H,\delta}(x) = \sum_{i=0}^{K} \hat{u}_i^{H,\delta} \phi_i(x), \tag{3.10}$$

where $\hat{u}_i^{H,\delta}$ are the coefficients to be determined. Since $\phi_i(x)$ satisfies the homogeneous boundary

---

[1] *strong* loosely mean that the trial functions are required to be both C^0 and C^1 continuous

conditions, $\hat{u}_i^{H,\delta}$ can take on any values and $u^{H,\delta}(x)$ will still satisfy the homogeneous boundary conditions. Substituing the approximate solution of $u^{H,\delta}(x)$ into equation 3.9, and applying the method of weighted resiudal,

$$(R(u^{H,\delta}), v_j(x)) = \int_{x_a}^{x_b} \left(\mathbb{L}u^{H,\delta}(x) - h(x) \right) v_j(x) \, \mathrm{d}x = 0, \qquad j = 0, ..., K, \tag{3.11}$$

where $v_j(x)$ is some *test* function and there are $K+1$ finite expansions. In the Galerkin method (or Bubnov-Galerkin), the weight function $v_j(x)$ takes on the same form as the trial functions $\phi_j(x)$ (Table 3.1). In other words, the differential equation is satisfied when projected on the *test/trial* functions. Substituting equation 3.10 into the residual equation 3.11 and applying $v_j(x) = \phi_j(x)$,

$$\sum_{i=0}^{K} \hat{u}_i^{H,\delta} \int_{x_a}^{x_b} \mathbb{L}\phi_i \phi_j \, \mathrm{d}x = \int_{x_a}^{x_b} \left(f(x) - \mathbb{L}\tilde{u}(x) \right) \phi_j \, \mathrm{d}x, \qquad j = 0, .., K \tag{3.12}$$

Equation 3.12 furnishes a system of $K+1$ linear equations with $K+1$ unknowns i.e $\{\hat{u}_0^{H,\delta}, ..., \hat{u}_K^{H,\delta}\}$. Applying integration by parts to equation 3.12, the equation reduces to,

$$\sum_{i=0}^{K} \hat{u}_i^{H,\delta} \left[\int_{x_a}^{x_b} \frac{\partial \phi_j}{\partial x} \frac{\partial \phi_i}{\partial x} + \lambda \phi_j \phi_i \, \mathrm{d}x \right] = - \int_{x_a}^{x_b} \frac{\partial \tilde{u}}{\partial x} \frac{\partial \phi_j}{\partial x} + (\lambda \tilde{u} + f(x)) \phi_j \, \mathrm{d}x, \tag{3.13}$$

which is known as the *weak*[2] form. The boundary conditions of the *weak* form naturally appears in the right-hand side of equation 3.14, which makes it convenient to implement. Equation 3.12 can be re-written in matrix form,

$$\begin{bmatrix} \int_{x_a}^{x_b} \frac{\partial \phi_0}{\partial x} \frac{\partial \phi_0}{\partial x} + \lambda \phi_0 \phi_0 \, \mathrm{d}x & \dots & \int_{x_a}^{x_b} \frac{\partial \phi_0}{\partial x} \frac{\partial \phi_K}{\partial x} + \lambda \phi_0 \phi_K \, \mathrm{d}x \\ \vdots & \ddots & \vdots \\ \int_{x_a}^{x_b} \frac{\partial \phi_K}{\partial x} \frac{\partial \phi_0}{\partial x} + \lambda \phi_0 \phi_0 \, \mathrm{d}x & \dots & \int_{x_a}^{x_b} \frac{\partial \phi_K}{\partial x} \frac{\partial \phi_K}{\partial x} + \lambda \phi_0 \phi_K \, \mathrm{d}x \end{bmatrix} \begin{bmatrix} \hat{u}_0^{H,\delta} \\ \vdots \\ \hat{u}_K^{H,\delta} \end{bmatrix} =$$
$$\begin{bmatrix} - \int_{x_a}^{x_b} \frac{\partial \tilde{u}}{\partial x} \frac{\partial \phi_0}{\partial x} + (\lambda \tilde{u} + f(x)) \phi_0 \, \mathrm{d}x \\ \vdots \\ - \int_{x_a}^{x_b} \frac{\partial \tilde{u}}{\partial x} \frac{\partial \phi_K}{\partial x} + (\lambda \tilde{u} + f(x)) \phi_K \, \mathrm{d}x \end{bmatrix} \tag{3.14}$$

where $\hat{\mathbf{u}}^{H,\delta} = [\hat{u}_0^{H,\delta}, ..., \hat{u}_K^{H,\delta}]$ is determined by solving the system of linear equations.

3.2 The Spectral/hp element methods

The spectral/hp element method (SEM) is related to the Galerkin method in which the type of *trial* function used. The spectral/*hp* element method combines 2 traditional numerical methods, namely,

---

[2] *trial* functions are only required to be C^0 continuous

1. Finite elements:

   The finite element method decomposes the global domain into a set of non-overlapping subdomains (finite elements), represented by linear shape functions. In a 1D domain, the size of each element is given by h and the approximate solution should covergence as h is decreased - also known as h-refinement. The flexibility of domain decomposition allows for complex engineering geometries to be represented.

2. Spectral method:

   The spectral method performs a global discretisation of the domain. The domain is represented by a linear combination of global continuous functions, such as the Fourier series. Spectral methods benefit from the property of *spectral convergence*, where the solution error decreases by $\mathcal{O}(c^{-N})$, where c is some constant $0 \leq c \leq 1$ and N is the number of polynomials (**?**). In other words, as the number of functions is increased, the error decreases exponentially.

The Spectral/hp element method leverages the advantages of both methods - geometric flexibility and spectral covergence. The spectral/hp method uses a series of high-order polynomials (Lagrange/Legendre) within each element. Considering each element consists of $P + 1$ linearly independent polynomials (where P refers to the highest polynomial order) spanning the polynomial space of $\mathcal{P}_P$, the error of a smooth solution with mesh-size h and polynomial order P has the property of (**?**),
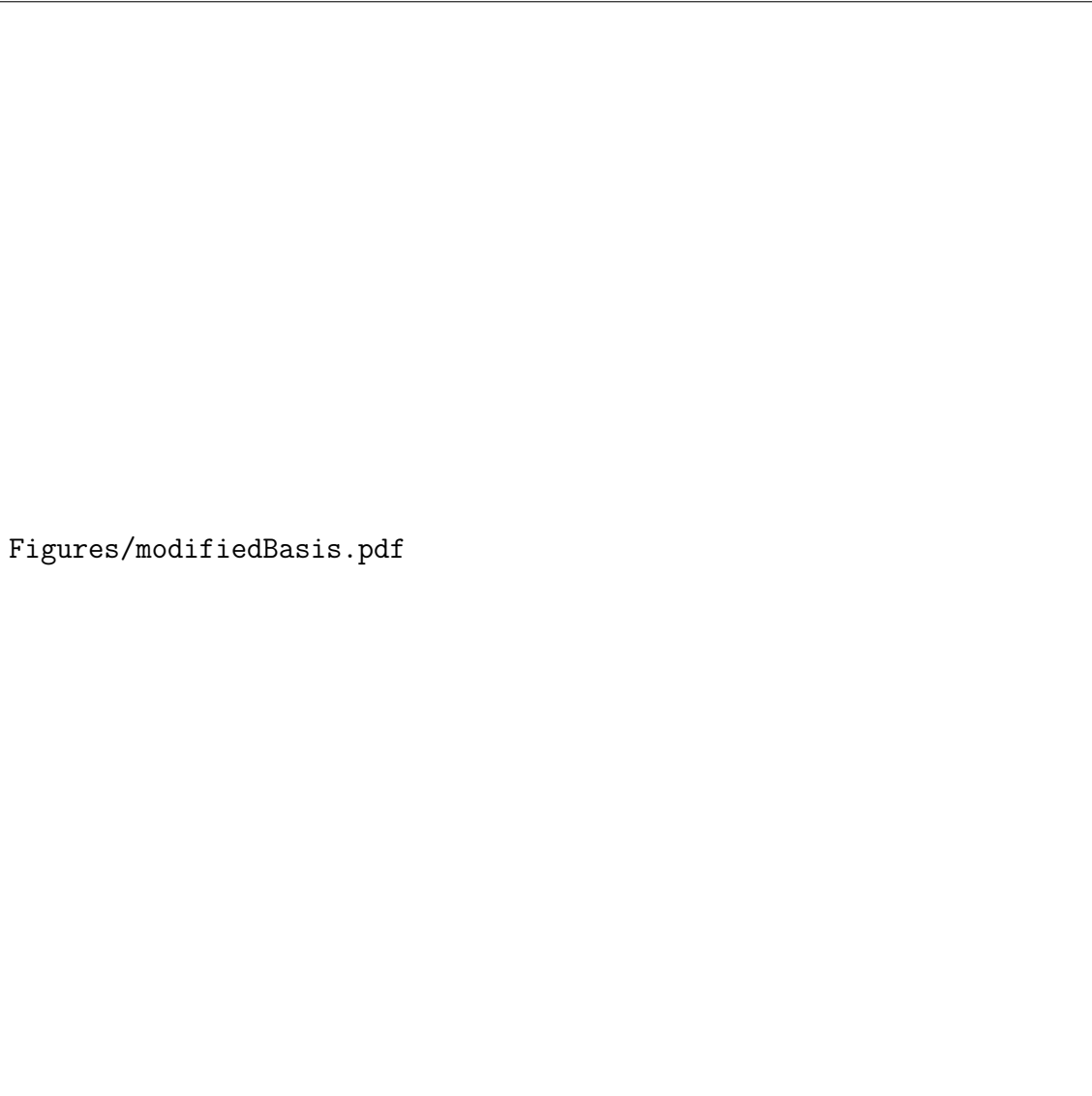
$$||u(x) - u^\delta(x)|| \leq Ch^P ||u(x)|| \approx \mathcal{O}(h^P). \tag{3.15}$$

Equation 3.15 implies that the error decreases as the h is decrease (mesh refinement) or as P is increased using higher-order polynomials.

The *trial* functions ϕ_p (or basis expansions) used in spectral/hp method consist of *boundary* and *interior* modes. *Interior* modes are defined to be zero on all boundaries, and non-zero within the boundary, satisfying homogeneous boundary conditions. *Boundary* modes take on non-zero values on the boundary, satisfying non-homogeneous boundary conditions and providing C^0 continuity between elements (**?**). Within the *nektar++* framework, the Jacobi polynomials $\mathbb{P}_p^{\alpha,\beta}(\xi)$ modified with linear elements are used as the *trial* functions. Using $\alpha = 1$, $\beta = 1$, and linear basis functions as *boundary* modes, the modified Jacobi polynomials are,

$$\phi_p(\xi) = \psi_p(\xi) = \begin{cases} \frac{1-\xi}{2} & \text{for } p = P \\ \frac{1-\xi}{2}\frac{1+\xi}{2}\mathbb{P}_{P-1}(\xi)^{1,1} & \text{for } P \geq 2 \\ \frac{1+\xi}{2} & \text{for } p = P, \end{cases} \tag{3.16}$$

where P denotes the highest polynomial order. Figure 3.1 shows the modified Jacobi polynomials for $p \in [0,5]$ described by equation 3.16. The boundary modes are ψ_0 and ψ_5 while the rest are boundary modes.

Figure 3.1: Modified Jacobi polymoials ψ_p for $p \in [0, 5]$

The Fourier spectral/hp element method uses a combination of Fourier expansions and spectral/hp element method to discretise the spatial domain. In a turbulent channel flow, the Fourier expansions are used to represent the periodic streamwise and cross stream directions, while the spectral/hp elements are used to discretise the wall-normal direction. Within the $nektar++$ framekwork, the Fourier spectral/hp element method (also known as a Quasi-3D approach), can be implemented either with 2D spectral/hp elements and 1D Fourier expansions (3DH1D) or 1D spectral/hp elements and 2D Fourier expansions (3DH2D). In this work, the 2D spectral/hp elements with 1D Fourier expansions are used to discretise the cross stream plane and streamwise flow respectively. The use of 2D spectral/hp elements in the cross stream plane is necessary to represent the riblet geometry (**?**). The time- and spatially-varying velocity and pressure in the cross stream planes are approximated as a finite sum of 2D modified Jacobi

polynomials up to the Pth-order,

$$\begin{bmatrix} \mathbf{u}^{\delta}(y,z,t) \\ p^{\delta}(y,z,t) \end{bmatrix} = \sum_{p=0}^{P} \sum_{q=0}^{P} \psi_p(y)\psi_q(z) \begin{bmatrix} \hat{\mathbf{u}}_{p,q}(t) \\ \hat{p}_{p,q}(t) \end{bmatrix} \tag{3.17}$$

where $\hat{\mathbf{u}}_{p,q}(t)$ and $\hat{p}_{p,q}(t)$ are the time-varying coefficients. Extending equation 3.17 to include the streamwise direction represented by Fourier expansions,

$$\begin{bmatrix} \mathbf{u}^{\delta}(x,y,z,t) \\ p^{\delta}(x,y,z,t) \end{bmatrix} = \sum_{k=0}^{N-1} \sum_{p=0}^{P} \sum_{q=0}^{P} \psi_p(y)\psi_q(z)e^{ik\alpha x} \begin{bmatrix} \hat{\mathbf{u}}_{p,q,k}(t) \\ \hat{p}_{p,q,k}(t) \end{bmatrix} = \sum_{k=0}^{N-1} e^{ik\alpha x} \begin{bmatrix} \mathbf{u}_k(y,z,t) \\ p_k(y,z,t) \end{bmatrix} \tag{3.18}$$

where $\alpha = \frac{2\pi}{L_x}$ is the streamwise wavenumber, L_x is the streamwise domain length and N refers to the number of Fourier expansions. Substituting equation 3.18 into the Navier-Stokes equations and taking the Fourier transform (equivalently to the Galerkin projection with respect to Fourier expansion as a test function) yields N-systems of equations,

$$\frac{\partial \mathbf{u}_k}{\partial t} = -\tilde{\nabla}_k p_k + \nu(\nabla^2_{y,z} - k^2\alpha^2)\mathbf{u}_k - [\widehat{(\mathbf{u} \cdot \nabla)\mathbf{u}}]_k, \qquad \tilde{\nabla}\mathbf{u}_k = 0 \tag{3.19}$$

where, $\tilde{\nabla} = (ik\alpha, \frac{\partial}{\partial y}, \frac{\partial}{\partial z})$, $\nabla^2_{y,z} = (\frac{\partial^2}{\partial y^2}, \frac{\partial^2}{\partial z^2})$ and $[\widehat{(\mathbf{u} \cdot \nabla)\mathbf{u}}]_k$ refers to the Fourier-transformed of the kth nonlinear term.

3.3 Temporal Discretisation

The velocity and pressure fields obtained from the Navier-Stokes equations are time dependent. A separate class of numerical methods used for temporal discretisation will be covered in this section. Temporal discretisation methods, used to solve initial value problems (IVPs) can be broadly categorised into two schemes:

1. Multi-stage schemes that advance the solution from the nth to $n^{th}+1$ time-step through a number of intermediate stages which are not solutions at the previous time-steps. The class of Runge-Kutta schemes is an example of multi-staged schemes. In general, multi-stage schemes are typically computationally intensive as extra intermediate steps are required to be computed.

2. Multi-step schemes that advance the solution from the nth to $n^{th}+1$ time-step using information from the from the previous $n^{th}-1$ time-step. The Adams-Bashforth and Adams-Moulton methods are examples of multi-step schemes. Multi-step schemes are typically more memory intensive as the solution from the previous time-steps are stored.

? proposed the General Linear Method that formalise any multi-stage, multi-step stepping scheme. The general linear method is also flexible to accommodate various implicit, explicit methods. Implicit methods are methods in which the solution at the $n^{th}+1$ time-step depends on some parameters at the $n^{th}+1$ time-step. Explicit methods are methods in which the solution

at time-step $n^{th} + 1$ depends only on parameters from the previous time-steps. In this section, the basic ideas of the generalised linear method will be introduced, followed by the implicity-explicit (IMEX) schemes, which are temporal discretisation schemes used in *nektar++*.

Consider an initial value problem of the following,

$$\frac{d\mathbf{u}}{dt} = \mathbf{f}(\mathbf{u}), \quad \mathbf{u}(t_0) = \mathbf{u}_0, \tag{3.20}$$

where $\mathbf{u}_0$ is the initial condition. The $n^{th} + 1$ step of the genereal linear method consist of r steps and s stages,

$$\mathbf{Y}_i = \Delta t \sum_{j=1}^{s} a_{ij} \mathbf{F}_j + \sum_{j=1}^{r} u_{ij} \mathbf{u}_j^n, \qquad 1 < i < s, \tag{3.21}$$

$$\mathbf{u}_i^{n+1} = \Delta t \sum_{j=1}^{s} b_{ij} \mathbf{F}_j + \sum_{j=1}^{r} v_{ij} \mathbf{u}_j^n, \qquad 1 < i < r, \tag{3.22}$$

where, $\mathbf{Y}_i$, $\mathbf{F}_i$ is known as to the stage values and derivatives respectively related by,

$$\mathbf{F}_i = \mathbf{f}(\mathbf{Y}_i). \tag{3.23}$$

The coefficient matrix $A = a_{ij}$, $B = b_{ij}$, $U = u_{ij}$, $V = v_{ij}$ uniquely defines the time integration scheme and equation 3.21 and 3.22 can be re-written as,

$$\begin{bmatrix} \mathbf{Y} \\ \mathbf{u}^{n+1} \end{bmatrix} = \begin{bmatrix} A \otimes I & U \otimes I \\ B \otimes I & V \otimes I \end{bmatrix} \begin{bmatrix} \Delta t \mathbf{F} \\ \mathbf{u}^n \end{bmatrix}, \tag{3.24}$$

$$\mathbf{Y} = \begin{bmatrix} \mathbf{Y}_1 \\ \vdots \\ \mathbf{Y}_s \end{bmatrix}, \quad \mathbf{F} = \begin{bmatrix} \mathbf{F}_1 \\ \vdots \\ \mathbf{F}_s \end{bmatrix}, \quad \mathbf{u}^{n+1} = \begin{bmatrix} \mathbf{u}_1^{n+1} \\ \vdots \\ \mathbf{u}_r^{n+1} \end{bmatrix}, \quad \mathbf{u}^n = \begin{bmatrix} \mathbf{u}_1^n \\ \vdots \\ \mathbf{u}_r^n \end{bmatrix}. \tag{3.25}$$

It is worth noting that $\mathbf{u}_1^{n+1}$, the first element in $\mathbf{u}^{n+1}$ is the solution at the $n^{th} + 1$ time-step. The other elements in $\mathbf{u}^n$ refer to the intermediate steps of a multi-step scheme. The implicit-explicit (IMEX) scheme is a type of time-integration scheme used in *nektar++*, where different terms in the Navier-Stokes equation are treated either explicitly, or implicitly. Using the generalised linear method, the IMEX method will be illustrated in this section. IMEX schemes are used to integrate an ordinary differential equation (ODE) of the following,

$$\frac{d\mathbf{u}}{dt} = \mathbf{f}(\mathbf{u}) + \mathbf{g}(\mathbf{u}), \quad \mathbf{u}(t_0) = \mathbf{u}_0, \tag{3.26}$$

where $\mathbf{f}(\mathbf{u})$ is the stiff function and integrated implicitly while $\mathbf{g}(\mathbf{u})$ is a non-linear function and integrated explicitly. The IMEX general linear method is rewritten in the form of,

$$\mathbf{Y}_i = \Delta t \sum_{j=1}^{s} a_{ij}^{\text{IM}} \mathbf{F}_j + \Delta t \sum_{j=1}^{s} a_{ij}^{\text{EX}} \mathbf{G}_j + \sum_{j=1}^{r} u_{ij} \mathbf{u}_j^n, \qquad 1 \le i \le s, \tag{3.27}$$

$$\mathbf{u}_i^n = \Delta t \sum_{j=1}^{s} b_{ij}^{\text{IM}} \mathbf{F}_j + \Delta t \sum_{j=1}^{s} b_{ij}^{\text{EX}} \mathbf{G}_j + \sum_{j=1}^{r} v_{ij} \mathbf{u}_j^n, \qquad 1 \leq i \leq r, \tag{3.28}$$

where $\mathbf{F}_i$ and $\mathbf{G}_i$ are the stage derivatives given as,

$$\mathbf{F}_i = \mathbf{f}(\mathbf{Y}_i), \qquad \mathbf{G}_i = \mathbf{g}(\mathbf{Y}_i). \tag{3.29}$$

Similar to equation 3.24, the above equations can be re-written in matrix form,

$$\begin{bmatrix} \mathbf{Y} \\ \mathbf{u}^{n+1} \end{bmatrix} = \begin{bmatrix} A^{\text{IM}} \otimes I & A^{\text{EX}} \otimes I & U \otimes I \\ B^{\text{IM}} \otimes I & B^{\text{EX}} \otimes I & V \otimes I \end{bmatrix} \begin{bmatrix} \Delta t \mathbf{F} \\ \Delta t \mathbf{G} \\ \mathbf{u}^n \end{bmatrix}, \tag{3.30}$$

The family of stiffly stable schemes (**?**) which are IMEX in nature, are used in to time-integrate the incompressible Navier-Stokes equations in *nektar++*. The partitioned matrix for the second-order stiffly stable schemes is given as,

$$\begin{bmatrix} A^{\text{IM}} \otimes I & A^{\text{EX}} \otimes I & U \otimes I \\ B^{\text{IM}} \otimes I & B^{\text{EX}} \otimes I & V \otimes I \end{bmatrix} = \begin{bmatrix} \frac{2}{3} & 0 & \frac{4}{3} & -\frac{1}{3} & \frac{4}{3} & -\frac{2}{3} \\ \frac{2}{3} & 0 & \frac{4}{3} & -\frac{1}{3} & \frac{4}{3} & -\frac{2}{3} \\ 1 & 0 & 0 & 0 & 0 & 0 \\ 0 & 1 & 0 & 0 & 0 & 0 \\ 0 & 0 & 0 & 0 & 1 & 0 \end{bmatrix}, \quad \text{with} \quad \mathbf{u}^{n+1} = \begin{bmatrix} \mathbf{u}^{n+1} \\ \mathbf{u}^n \\ \Delta t \mathbf{F}^{n+1} \\ \Delta t \mathbf{F}^n \end{bmatrix}. \tag{3.31}$$

3.4 Velocity correction scheme for incompressible Navier Stokes equations

While methods for temporal and spatial discretisation have been discussed, it is not possible to apply these techniques in a straight-forward manner to the incompressible Navier-Stokes equations. This is because of the unique role of the pressure field which ensures that the time-dependent velocity field is divergence-free. However, the velocity and the pressure fields form a coupled-system through the continuity and momentum equations which requires the solution of both fields simultaneously. In general, there are 3 ways to deal with velocity-pressure coupling: (1) Coupled methods (*Uzawa* method), (2) Change of variables (streamfunction-vorticity formulation) and (3) Splitting methods which decouples velocity and pressure. The velocity correction scheme (VCS) (**?**), a type of splitting method, decouples the velocity field from the pressure field used in *nektar++* will be discussed in this section. The velocity correction scheme is a stiffly-stable time-integration (IMEX) scheme which treats the nonlinear terms (advection) explicitly and linear terms (pressure gradient and diffusion) implicitly. The VCS will be demonstrated through a worked example. The incompressible Navier-Stokes equations

with unit density, constant density and viscosity is written as,

$$\frac{\partial \mathbf{u}}{\partial t} = \mathbf{N}(\mathbf{u}) - \nabla p + \nu \mathbf{L}(\mathbf{u}), \qquad \nabla \cdot \mathbf{u}, \tag{3.32}$$

where $\mathbf{u}$, p, ρ, ν refers to the fluid's velocity, pressure, density and kinematic viscosity respectively. The convection and diffusion terms are conveniently written as nonlinear and linear functions,

$$\mathbf{N}(\mathbf{u}) \equiv -(\mathbf{u} \cdot \nabla)\mathbf{u} = -\frac{1}{2}\left[(\mathbf{u} \cdot \nabla)\mathbf{u} + \nabla \cdot (\mathbf{u}\mathbf{u})\right], \qquad \mathbf{L}(\mathbf{u}) \equiv \nabla^2 \mathbf{u}. \tag{3.33}$$

The nonlinear terms are written in the skew-symmetric to minimise aliasing errors (**?**). The first step in the scheme is to time integrate the nonlinear terms explicitly,

$$\frac{\hat{\mathbf{u}} - \sum_{q=0}^{J_e-1} \alpha_q \mathbf{u}^{n-q}}{\Delta t} = \sum_{q=0}^{J_e-1} \beta_q \mathbf{N}(\mathbf{u}^{n-q}), \tag{3.34}$$

where $\hat{\mathbf{u}}$ is the first intermediate velocity field, J_e denotes the order of the explicit scheme, superscript n denotes the solution at the nth time-step and α_q, β_q refers to constant related to the IMEX schemes. Next, the second intermediate velocity field $\hat{\hat{\mathbf{u}}}$ is obtained from the gradient of the pressure field at $n+1$,

$$\frac{\hat{\hat{\mathbf{u}}} - \hat{\mathbf{u}}}{\Delta t} = -\nabla p^{n+1}. \tag{3.35}$$

However, the pressure field at time-step $n+1$ is not known. Taking the divergence of equation 3.35, and assuming that $\hat{\hat{\mathbf{u}}}$ is divergence-free, the Poisson equation for pressure is given as,

$$\nabla^2 p^{n+1} = \nabla \cdot \left(\frac{\hat{\mathbf{u}}}{\Delta t}\right). \tag{3.36}$$

with the following boundary condition,

$$\frac{\partial p^{n+1}}{\partial n} = \mathbf{n} \cdot \left(\frac{\hat{\hat{\mathbf{u}}} - \hat{\mathbf{u}}}{\Delta t}\right) \tag{3.37}$$

However, this boundary condition often suffer from splitting errors and may lead to wrong solutions (**?**). To rectify this, the boundary condition is directly obtain by taking normal dot product with 3.32 and evaluated explicity (**?**),

$$\frac{\partial p^{n+1}}{\partial t} = -\sum_{q=0}^{J_e-1} \beta_q \left[\frac{1}{\Delta t}\mathbf{u}^{n-q} + \nu(\nabla \times \omega^{n-q}) + (\mathbf{u}^{n-q} \cdot \nabla)\mathbf{u}^{n-q}\right] \cdot \mathbf{n}. \tag{3.38}$$

where $\omega = \nabla \times \mathbf{u}$, J_e is the order for the explicit scheme, β_q is the coefficient related to the time-integration scheme. We obtain the pressure field at time-step $n+1$ by solving the pressure Poisson equation (3.36) with the modified boundary conditions (3.38). Then, the second intermediate velocity field $\hat{\hat{\mathbf{u}}}$ is obtained from equation 3.35. Finally, the velocity field

at $n+1$ is obtain from the final step of the scheme by solving

$$\frac{\gamma_0 \mathbf{u}^{n+1} - \hat{\hat{\mathbf{u}}}}{\Delta t} = \nu \sum_{q=0}^{J_i-1} \beta_q \mathbf{L}(\mathbf{u}^{n+1-q}), \qquad \mathbf{u}^{n+1}|_{\delta\Omega} = g_D \tag{3.39}$$

where J_i denotes the order of the implicit scheme, γ_0, β_q are coefficients related to the stiffly stable time-integration scheme and $\mathbf{u}^{n+1}$ satisfies the Dirichlet boundary conditions. Table 3.2 shows the coefficients of stiffly-stable time-integration schemes (**?**).

test	1st order	2nd order
γ_0	1	3/2
β_0	1	2
β_1	0	-1
α_0	0	-1/2
α_1	0	0

Table 3.2: Stiffly-stable splitting scheme coefficients

3.5 Linear Stability Analysis

3.6 Edge Tracking

To study the dynamics of infinitetisimal perturbations about a base flow, the time evolution equation for the perturbations dynamics typically reduces to,

$$\frac{\partial}{\partial t}\mathbf{u} = \mathcal{L}\mathbf{u}, \tag{3.40}$$

where $\mathcal{L}, \mathbf{u}$ refers to the linearised operator and a vector of perturbations. Suppose the that linear operator is diagonlisable,

$$\mathcal{L} = \begin{bmatrix} | & & | \\ \mathbf{s}_1 & \cdots & \mathbf{s}_n \\ | & & | \end{bmatrix} \begin{bmatrix} \lambda_1 & & 0 \\ & \ddots & \\ 0 & & \lambda_n \end{bmatrix} \begin{bmatrix} | & & | \\ \mathbf{s}_1 & \cdots & \mathbf{s}_n \\ | & & | \end{bmatrix}^{-1} = \mathcal{S}\Lambda\mathcal{S}^{-1}. \tag{3.41}$$

Suppose we can decompose our initial conditions into a superposition of eigenmodes,

$$\mathbf{u}_0 = \alpha_{1,0}\mathbf{s}_1 + \alpha_{2,0}\mathbf{s}_2 + ... + \alpha_{N,0}\mathbf{s}_n = \sum_{i=1}^{n} \alpha_{i,0}\mathbf{s}_i, \tag{3.42}$$

and w

Edge state tracking

Computing Invariant solutions

Chapter 4

Transitional Rayleigh-Bénard Poiseuille flows

4.1 Introduction

Rayleigh-Bénard-Poiseuille (RBP) flows describe the motion of fluids confined between two extended parallel plates, heated from below and cooled from the top, with an imposed pressure gradient. This system combines classical Rayleigh-Bénard convection (RBC) and plane Poiseuille flow (PPF), driven by buoyancy and shear forces, respectively. In the limiting cases, the laminar solution can transition to convection rolls (RBC) or shear-driven turbulence (PPF), depending on whether buoyancy or shear forces dominate. Transition to turbulence in the regime where both forces interact remains largely unexplored. For instance, do buoyancy forces promote the transition to shear-driven turbulence?; how does shear influence the convection? Understanding the transition to turbulence in this regime can have implications for applications such as the fabrication of thin uniform films in chemical vapour deposition [**??**] and the cooling of electronic components [**??**].

4.1.1 Rayleigh-Bénard Poiseuille (RBP) flows

The non-dimensionalised parameters that govern the RBP flow are the Rayleigh number, $Ra = \eta g d^3 \Delta T / \nu \kappa$, Reynolds number, $Re = W_c h / \nu$, Prandtl number, $Pr = \kappa / \nu$, and the aspect ratio of the flow domain, $\Gamma = L/2d$, where $\eta, g, \Delta T, \nu, \kappa, W_c, h, d, L$ are the thermal expansion coefficient, acceleration due to gravity, temperature difference between the bottom and top wall, kinematic viscosity, thermal diffusivity, laminar centreline velocity, domain's half-depth, domain's full-depth, length (or span), respectively.

? first investigated the primary instabilities of RBP flows, which can be determined by Re, Ra, Pr, and the planar x-z perturbations wavenumbers α, β respectively. For a given Ra and Pr, the neutral stability curves are limited by the development of Tollmien-Schlicting waves for $Re \geq Re_{TS} = 5772.22$ [**?**], and convection rolls within $0 \leq Re < Re_{TS}$. Convection rolls can be categorised based on their orientation to the mean flow, namely, longitudinal

$(\alpha = 0, \beta \neq 0)$, transverse $(\alpha \neq 0, \beta = 0)$ and oblique rolls $(\alpha \neq 0, \beta \neq 0)$. The linearised system governing the onset of longitudinal rolls is analogous to the linearised RBC system, with a critical Rayleigh number, $Ra_\parallel = Ra_{RB} = 1708.8$ and critical wavenumber, $\alpha_\parallel = \alpha_{RB} = 3.13$ [**??**], independent of Re and Pr. The critical Rayleigh number for oblique and transverse rolls matches that of RBC at $Re = 0$ due to horizontal isotropy, but increases as Re increases, depending on Pr, i.e., $Ra_\perp = f(Re, Pr)$ [**???**]. When spatially developing instabilities are considered, longitudinal rolls are always convectively unstable, and transverse rolls can become absolutely unstable [**???**]. Nonmodal stability analyses of subcritical RBP indicate that the optimal transient growth, G_{max}, increases gradually with Ra. The wavenumber of the optimal initial conditions, β_{max}, resembles that observed in shear flows [**?**], and gradually approaches the critical wavenumber of convection rolls, $\alpha_\parallel$, as Ra increases [**?**]. For $Re > 0$, the longitudinal rolls appear as the dominant primary instability [**?**]. Secondary stability analyses of longitudinal rolls reveal a wavy instability near $Re \sim 100$ [**?**], leading to wavy longitudinal rolls, which are convectively unstable [**??**]. The influence of finite lateral extensions in RBP flows on the stability of longitudinal and transverse rolls [**??**], as well as wavy rolls [**??**], has been reported. In finite streamwise extensions of RBP flows, the onset of convection rolls and the heat flux variations due to entrance effects have been investigated [**???**]. More recently, shear-driven turbulence can enhance heat fluxes in turbulent RBP flows [**??**]. RBP flows with sinusoidal heating and wavy walls have also been studied [**?**]. For an in-depth discussion of RBP flows, see the reviews by **?** and **?**.

4.1.2 Rayleigh-Bénard convection (RBC)

In the limiting case of $Re = 0$, the RBP problem reduces to the buoyancy-driven Rayleigh-Bénard convection (RBC). We provide an overview of the key developments of RBC as a foundation for studying RBP flows at $Re = 0$. Beyond the onset, $Ra > Ra_{RB}$, the secondary stability characteristics of ideal straight rolls (ISRs), which are infinitely-parallel convection rolls, are described by the Busse balloon. This balloon defines the stability boundaries of ISRs based on their wavenumber, Ra and Pr. For $Pr = 1$ and $Ra_{RB} < Ra \lesssim 6000$, the secondary instabilities primarily modify the ISR wavenumber to remain within the boundaries of the Busse balloon. These include the cross-roll, Eckhaus, or skewed-varicose instabilities [**???**]. An oscillatory secondary instability emerges at $Ra \gtrsim 5500$, where a stationary ISR transitions into a time-dependent tertiary state, known as oscillatory ISRs [**??**], and tthese instabilities has been reported in experiments [**????**]. Notably, ISRs appear to be the exception rather than the norm as multiple convection patterns in the form of squares, targets, and oscillatory convection patterns have been reported, resulting in many multiple stable states in the same Ra parameter space where ISRs are expected [**???????**]. For large aspect ratios, $\Gamma \gtrsim 20$, convection rolls can exhibit spatiotemporal chaotic behaviour, known as spiral defect chaos (SDC) within the same Ra range [**?????????**]. It is now established that both SDC and ISR can coexist at the same Ra, forming a bistable system confirmed experimentally [**?**].

This study focuses on the influence of Re on the complex convection patterns of RBC within

$Ra \in [0, 10000]$. Specifically, we investigate the impact of shear on the bistable system between SDC and ISRs, the stability boundaries of the Busse balloon, and the possible emergence of multiple 'non-ISR' states as Re increases.

4.1.3 Plane Poiseuille flows (PPF)

The other limiting case at $Ra = 0$ corresponds to the classical plane Poiseuille flow (PPF), and its relevance to RBP flows is discussed here. Turbulence in PPF is known to be subcritical, occurring at $Re \sim 1000$, well below the threshold $Re < Re_{TS}$ [??]. This could be due to the non-normality of the Orr-Sommerfeld equations, allowing disturbances to develop significant transient growth at $Re = 1000$ [??]. The optimal initial conditions involve streamwise vortices which amplify streaks, related to the lift-up effect [?]. These modal and nonmodal mechanisms above highlight developments based on linear methods. Utilising tools from nonlinear dynamics systems, turbulence could be viewed as chaotic trajectories around unstable nonlinear solutions known as invariant solutions or exact coherent structures [????????]. We adopt this perspective as we analyse chaotic (turbulent) trajectories within a confined domain, $\Gamma = \pi/2$, motivated from the minimal flow unit from ?. In large domains, $\Gamma \gtrsim 20$, transitional PPF exhibits spatiotemporal intermittent turbulent-laminar bands, where turbulent and laminar regions can coexist [??????].

This study focuses on the impact of Ra on the transition to turbulence. For instance, could convection rolls, reminiscent of the optimal streamwise vortices [?], assist the transition towards subcritical turbulence?

4.1.4 Objectives and organisation

While the stability characteristics of laminar RBP flows have been well studied (see §4.1.1), its transition to shear-driven turbulence remains poorly understood and is the focus of this study. For instance, how do wavy rolls evolve as Re increases? Additionally, we also aim to bridge the gap between RBC (see §4.1.2), and PPF (see §4.1.3) by investigating the impact of Re on the bistability between SDC and ISRs in RBC, as well as the influence of Ra on turbulent-laminar bands in PPF. The main objective of this work is to perform direct numerical simulations (DNS) of transitional RBP flows within $Ra \in [0, 10000]$ and $Re \in [0, 2000]$ at $Pr = 1$ in both large and confined domains, $\Gamma = 4\pi$, $\Gamma = \pi/2$. This study is largely exploratory, focusing on identifying different flow regimes and providing key insights into their dynamical processes. Hence, we do not intend to perform bifurcation analysis due to the lack of prior knowledge of the phase space, which could lead to large computational costs.

The paper is organised as follows: in §5.2, we describe the problem formulation, governing equations, numerical methods and setup. In §4.3, we present the Ra-Re phase space, identifying five distinct regimes and their transition boundaries. We also introduce a new 'intermittent roll' regime and discuss the coexistence of longitudinal rolls with turbulent-laminar bands, highlighting the role of longitudinal rolls in transitional RBP flows. In §5.6, we investigate the

unstable manifolds of longitudinal rolls in a confined domain, $\Gamma = \pi/2$, revealing dynamical connections between shear-driven turbulence, longitudinal rolls and the laminar state, and discuss its relevance to the larger domain. Finally, we conclude in §4.5, and propose directions for future work.

4.2 Problem formulation

4.2.1 Governing equations

We consider a layer of fluid sandwiched between two extended parallel plates of equal length and span, $L = L_x = L_z$, separated by depth, d (or two half heights, $h = d/2$), with a uniform upper and lower plate temperature T_U and T_L. The fluid is unstably stratified such that $\Delta T = T_L - T_U > 0$. The fluid has a density of ρ, kinetic viscosity, ν, thermal diffusivity κ. The governing equations are the non-dimensionalised Navier-Stokes equations with Boussinesq approximation given by,

$$\frac{\partial \mathbf{u}}{\partial t} + (\mathbf{u} \cdot \nabla)\mathbf{u} = -\nabla p + \frac{1}{Re}\nabla^2 \mathbf{u} + \frac{Ra}{8PrRe^2}\theta \mathbf{j}, \tag{4.1a}$$

$$\frac{\partial \theta}{\partial t} + (\mathbf{u} \cdot \nabla)\theta = \frac{1}{RePr}\nabla^2 \theta, \tag{4.1b}$$

$$\nabla \cdot \mathbf{u} = 0, \tag{4.1c}$$

with the following boundary conditions at the wall,

$$\mathbf{u}|_{y=\pm h} = 0, \quad \theta|_{y=-h} = 1, \quad \theta|_{y=h} = 0, \tag{4.2}$$

and periodic boundary conditions in the planar x and z directions. $\mathbf{u}(\mathbf{x}, t)$ denotes the non-dimensionalised velocity scaled by the laminar centreline velocity, W_c, i.e. $W_{lam}(y) = W_c(1-y^2)$. $\mathbf{x} = (x, y, z)$ and t denote the non-dimensionalised spatial and temporal coordinates scaled by the half-height, h and the advective time scale, W_c/h, where x, y, z refers to the spanwise, wall-normal and streamwise directions, respectively. p refers to the non-dimensionalised pressure scaled by ρW_c^2, and $\theta(\equiv (T - T_U)/\Delta T)$ refers to the non-dimensionalised temperature with T being the absolute temperature. $\mathbf{j}$ denotes the unit vector in the y-direction. We note that the rescaled $Ra/8$ term in the momentum forcing terms is equivalent to the Rayleigh number scaled based on the half-depth, h, whereas Ra is scaled based on depth, d, as in classical RBC. The Rayleigh number, Ra, Reynolds number Re and Prandtl number, Pr are defined in §**??**. We set $Pr = 1$ in this study. For the Rayleigh-Bénard convection problem, we note that the equation (4.1) becomes singular at $Re = 0$. In such cases, we solve the non-dimensionalised incompressible Navier-Stokes equations based on thermal length, velocity and temporal scales derived in Appendix A.1.

4.2.2 Numerical Methods

The governing equations are solved numerically using an open-source spectral/hp-element package, Nektar++ [??]. The computational mesh consists of 2D quadrilateral elements in the $x-y$ plane generated using Gmsh [?] and then imported into Nektar++ using Nekmesh [?]. We discretise the spatial domain based on the quasi-3D approach, employing spectral/hp elements in the $x-y$ plane and Fourier expansions in the z [?]. We emphasise that the streamwise direction is in z. The discretised equations are solved using a velocity correction scheme, based on a second-order stiffly splitting scheme, where the nonlinear advection and forcing terms are treated explicitly, while the pressure and diffusion terms are treated implicitly [?]. The 3/2 and polynomial de-aliasing rule for the Fourier expansions and spectral/hp elements are applied during the evaluation of the nonlinear advection terms. We refer to the solution obtained at the end of the velocity correction scheme as the homogenous velocity, $\mathbf{u}_h$. Due to the enforced periodicity in the streamwise z direction via Fourier expansions, a pressure drop cannot be prescribed to drive the flow for $Re > 0$ scenarios. To sustain the flow, we use a Green's function approach [?] to impose a constant flow rate,

$$W_b = Q(\mathbf{u}) = \frac{1}{2L_x h} \int_{x,y} \mathbf{u} \, \mathrm{d}x \mathrm{d}z, \tag{4.3}$$

where W_b and $Q(\cdot)$ refer to the desired flow rate and flow rate operator. A correction velocity, $\mathbf{u}_{corr}$, is obtained by solving the linear Stokes equation with unit forcing once and is stored for reuse. At the end of every time-step, the final velocity field, $\mathbf{u}$, is then updated by adding this correction velocity to the homogeneous velocity obtained from the velocity correction scheme,

$$\mathbf{u} = \mathbf{u}_h + \gamma \mathbf{u}_{corr}, \tag{4.4}$$

where γ defined as,

$$\gamma = \frac{W_b - Q(\mathbf{u}_h)}{Q(\mathbf{u}_{corr})}, \tag{4.5}$$

is adjusted to satisfy the desired flow rate, W_b. The flow rate, W_b, is related to the laminar centreline velocity $W_c = 3/2W_b$, which defines the Reynolds number, $Re = W_c h/\nu$. For more details on the numerical method, the reader is referred to ?.

4.2.3 Ra-Re sweep

We consider fifty-two numerical experiments at $Re = 0, 0.1, 1, 10, 100, 500, 750, 1000, 1050, 2000$, and $Ra = 0, 2000, 3000, 5000, 8000, 10000$ at $Pr = 1$ with a large aspect ratio of $\Gamma = 4\pi$. Their spatial and temporal numerical resolutions and time-integration horizon, T, are described in the Appendix A.2. The initial conditions of all cases are sampled from a statistically stationary solution. Laminar solutions are obtained for $Ra = 0$, $Re \leq 1000$, and are omitted from the analysis. For all of the cases considered here, we maintain the same spatial resolution except $Re = 2000$, where the number of Fourier expansions was doubled. The temporal resolution

between the numerical experiments differs due to time scales arising from the different flow physics, as we shall see later. We have also considered a mesh independence study for the end case of $Ra = 10000$, $Re = 2000$, where doubling the number of Fourier modes or increasing the polynomial order by 1 led to a $< 1\%$ change in near-wall transport properties defined by the Nusselt number, $Nu = -\langle d\theta/dy_{y=-h}\rangle_{x,z} d/\Delta T$, and shear, $\langle dw/dy|_{y=-h}\rangle_{x,z}$, where $\langle \cdot \rangle_{x,z} = 1/(L_x L_z) \int_{z,x} \cdot \, dx dz$ refer to the plane averaged operator.

4.2.4 Linear Stability Analysis

In §5.6, we will perform numerical experiments where small disturbances are added along the unstable manifolds of longitudinal rolls. To determine the unstable manifolds, we consider a small disturbance about the longitudinal roll state,

$$\mathbf{u}(\mathbf{x}, t) = \mathbf{u}_{LR}(\mathbf{x}) + \hat{\mathbf{u}}(\mathbf{x}, t), \tag{4.6a}$$

$$\theta(\mathbf{x}, t) = \theta_{LR}(\mathbf{x}) + \hat{\theta}(\mathbf{x}, t), \tag{4.6b}$$

$$p(\mathbf{x}, t) = p_{LR}(\mathbf{x}) + \hat{p}(\mathbf{x}, t), \tag{4.6c}$$

where $\mathbf{q} = [\mathbf{u}, \theta, p]^T$, $\mathbf{q}_{LR} = [\mathbf{u}_{LR}, \theta_{LR}, p_{LR}]^T$ and $\hat{\mathbf{q}} = [\hat{\mathbf{u}}, \hat{\theta}, \hat{p}]^T$ refers to solution vector, the longitudinal state and the disturbances respectively. We substitute equation (5.3) into (4.1) and neglect the nonlinear terms, leading to the linearised equations,

$$\frac{\partial \hat{\mathbf{q}}}{\partial t} = \mathcal{A}(\mathbf{q}_{LR}; Re, Ra, Pr)\hat{\mathbf{q}}, \tag{4.7a}$$

where

$$\mathcal{A}(\mathbf{q}_{LR}; Re, Ra, Pr) = \begin{pmatrix} -(\mathbf{u}_{LR} \cdot \nabla) - (\nabla \mathbf{u}_{LR} \cdot) + 1/Re\nabla^2 & \frac{Ra}{8Re^2 Pr}\hat{\mathbf{j}} & -\nabla \\ -(\nabla \theta_{LR} \cdot) & -(\mathbf{u}_{LR} \cdot \nabla) + \nabla^2 & 0 \\ \nabla \cdot & 0 & 0 \end{pmatrix}. \tag{4.7b}$$

Out of convenience, we will only consider longitudinal rolls invariant along the z-direction, which are also assumed to be periodic in x-direction, and the following form of normal-mode solution can be considered,

$$\hat{\mathbf{q}}(\mathbf{x}, t) = \breve{\mathbf{q}}(x, y)e^{i(\alpha x + \beta z) + \lambda t} + \text{c.c}, \tag{4.8}$$

where λ, α and β are the complex frequency, the spanwise wavenumber (or the Floquet exponent), and the stream wavenumber, respectively. Using the periodic nature of $\breve{\mathbf{q}}(x, y)$ in the

x-direction, (5.5) can also be written as

$$\hat{\mathbf{q}}(\mathbf{x}, t) = \left[\sum_{n=-\infty}^{\infty} \breve{\mathbf{q}}_n(y) e^{i\frac{2\pi}{L_x}(n+\epsilon)x} \right] e^{i\beta z + \lambda t} + \text{c.c}, \qquad (4.9)$$

where $\epsilon(= \alpha L_x/(2\pi))$ is the Floquet detuning parameter with $0 \leq \epsilon \leq 1/2$. In this study, we will only consider the identification of the unstable manifolds of longitudinal rolls in a fixed computational domain, hence, the fundamental mode, $\epsilon = 0$, is of sole interest. Substituting equation (5.6) into (5.4) result to a discretised eigenvalue problem with the eigenvalue λ. The wavenumber, β, is restricted to discrete values of $\beta = 2\pi m/L_z$, and m is a positive integer, for the given computational domain. The resulting eigenvalue problems are solved using a time-stepper-based iterative Arnoldi algorithm implemented in Nektar++ [**?**].
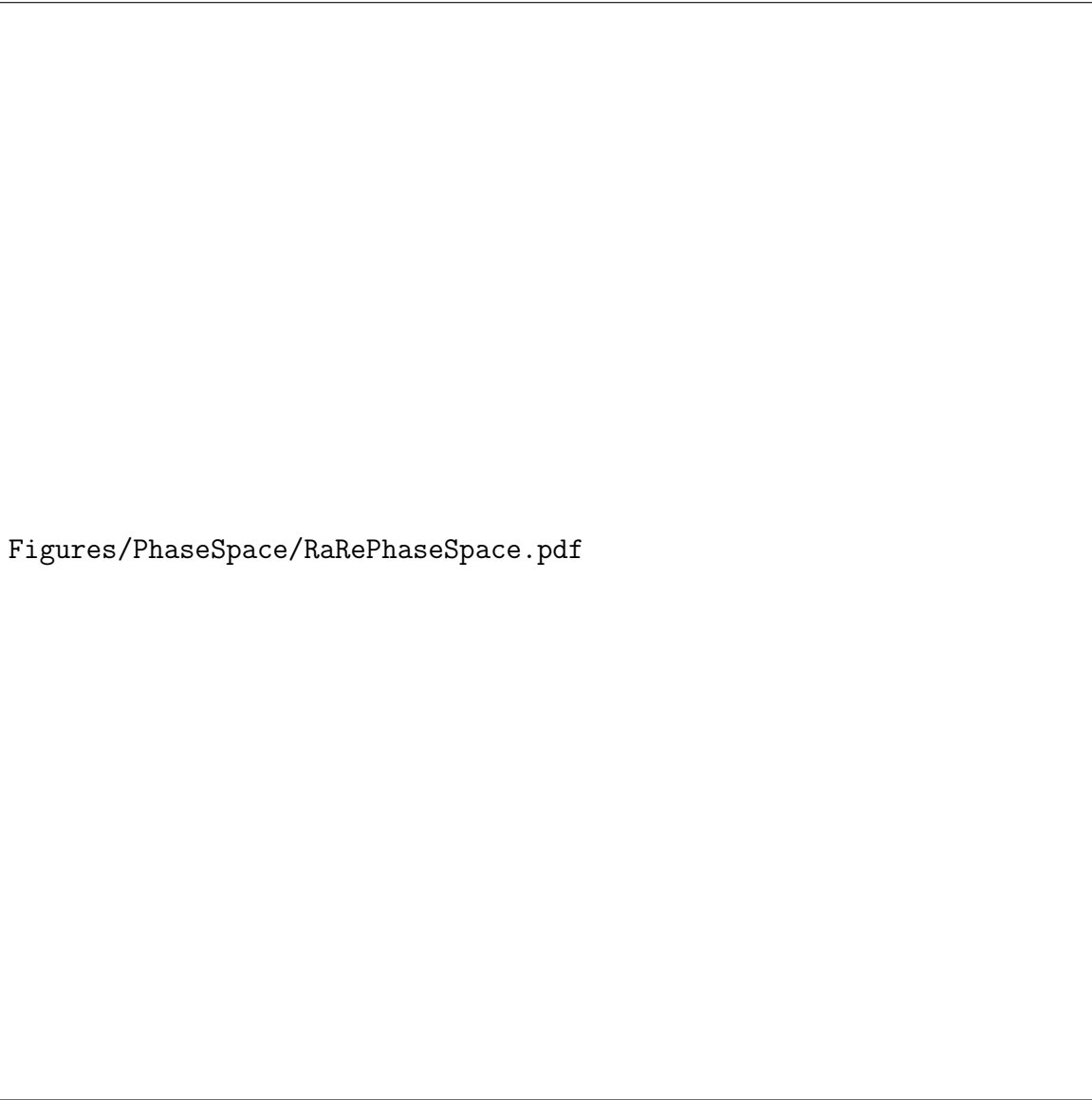
4.3 Ra-Re Phase Space

4.3.1 Classification

We present the results obtained from the DNS of transitional RBP flows, focusing on the parameter space defined by Rayleigh numbers in the range $Ra \in [0, 10000]$, and Reynolds numbers in the range of $Re \in [0, 2000]$ (see Appendix A.2 for the full details). At opposite ends of the Re-spectrum, the onset of SDC and subcritical shear-driven turbulence are shown. Figure 4.1 shows the terminal midplane temperature snapshots, $\theta(x, z)|_{y=0}$, of different flow regimes. The solid blue curves refer to the approximate neutral stability boundaries for the longitudinal and transverse rolls as $Ra_{\parallel} = 1708$, and $Ra_{\perp} = f(Re)$ respectively [**?**]. In the absence of shear at $Re = 0$, these curves merge onto the classical critical RBC instability at $Ra_{cr} = 1708$, as ISRs become rotationally invariant about the wall-normal axis. Additionally, a red arrow indicates the secondary neutral stability curve, marking the onset of oscillatory instabilities of ISRs within $5000 < Ra < 8000$ at $Re = 0$ [**?**]. The phase diagram in figure 4.1 is not plotted to scale but serves as a conceptual reference for distinguishing different flow states.

In this Ra-Re phase space, we categorise the flow behaviour into five distinct regimes: (1) bistability between SDC and ISRs (SDC & ISRs), (2) ideal straight rolls (ISRs), (3) wavy rolls, (4) intermittent rolls, and (5) shear-driven turbulence. The categories are defined based on common flow structures (patterns), and/or dynamical characteristics, ranging from equilibrium solutions to intermittent and chaotic dynamics. Furthermore, we classify these states based on their first and second-order statistical properties, where they appear independent of Re in the buoyancy-dominated regime (shaded in red), and Ra in the shear-dominated regime (shaded in blue), discussed in Appendix A.3. In the mixed regime shaded in green, both Ra and Re are important.

In the buoyancy-dominated regime, the flow structures are predominantly described by convection rolls, such as SDC, transverse, oblique, longitudinal rolls (and ISRs with no mean flow) or oscillatory rolls. The bistability between SDC and ISRs is preserved for $Ra \geq 3000$
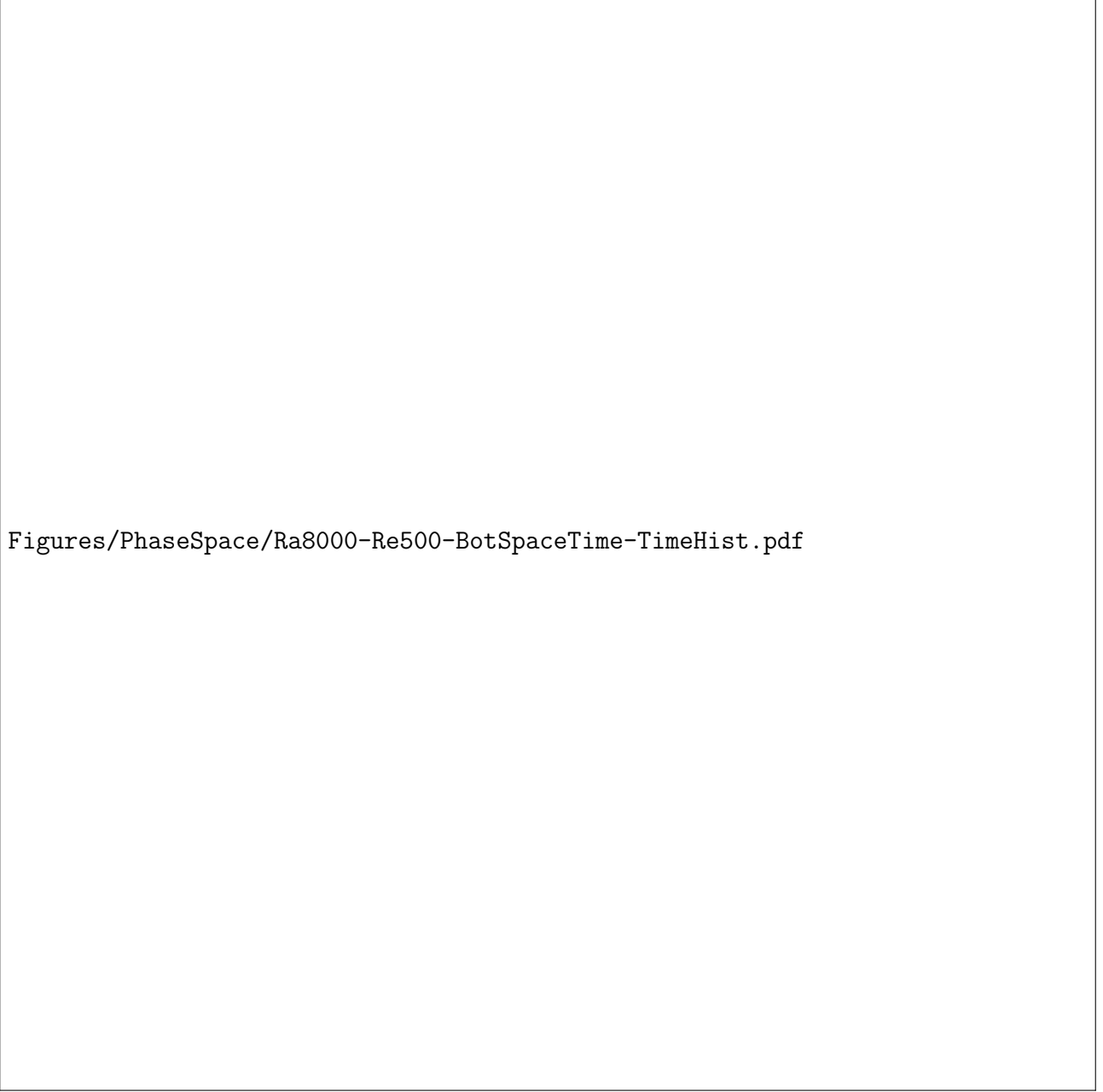
Figure 4.1: The $Ra - Re$ phase space illustrates the terminal midplane temperature snapshots, $\theta(x, z)|_{y=0}$ for $Re \in [0, 2000]$ and $Ra \in [0, 10000]$, classified into five distinct regimes: (1) SDC & ISRs, (2) ISRs, (3) wavy rolls, (4) intermittent rolls and (5) shear-driven turbulence. The blue solid curves refer to primary neutral curves of the longitudinal and transverse rolls $Ra_{\parallel}, Ra_{\perp}$. The red curve refers to secondary oscillatory instability of ISRs at $Re = 0$ [?]. Shades of red, green and blue indicate their dominant mechanism, whether driven by buoyancy or shear (or mixed). The plot is not to scale.

at $Re = 0.1$, and $Re = 1$ for $Ra \geq 5000$. This points towards a Re_s-threshold where SDC disappears, which depends on Ra, demarcated by the black dotted lines on the left-hand side of figure 4.1. However, computing this Re_s-threshold is beyond the scope of this work. Notably, a transverse roll with a 'hooked-like' defect is observed at $Re = 1$, $Ra = 3000$, reminiscent of the multiple 'non-ISR' states in RBC (see references in §4.1.2). At $Re = 10$, SDC disappears and longitudinal rolls appear. As Re is increased further to 1000, the longitudinal rolls emerge as the preferred solution at $Ra = 2000, 3000$. Notably, the non-dimensionalised spanwise wavenumber of these longitudinal rolls is approximately $\alpha d \approx 1.65$, which happens to lie outside of the stability boundaries of the Busse balloon in RBC [?]. This may suggest that the stability boundaries may expand as Re increases. Further evidence comes from the skewed-varicose longitudinal roll structure at $Re = 100$, $Ra = 3000$, which resembles a skewed-varicose instability, a secondary instability related to the Busse balloon boundaries [?].

As Re approaches 100, the longitudinal rolls undergo a secondary wavy instability [??], leading to the emergence of wavy longitudinal rolls depicted in figure 4.1. The wavelength of streamwise waviness and spanwise periodic longitudinal roll appears across approximately three intervals of streamwise length, $\Lambda_z \sim L_z/3$, and twelve intervals of spanwise length, $\Lambda_x \sim L_x/12$, respectively. The ratio between the wavelength of streamwise waviness and spanwise roll is about ~ 4, around the ballpark reported by ?.

4.3.2 Spatiotemporal intermittent rolls

As Re approaches $Re = 500$, wavy rolls disappear. Instead, a new regime, referred to as intermittent rolls, is observed. In this regime, the longitudinal rolls remain as the dominant convection structure, interspersed with a spatiotemporal intermittent breakdown towards the laminar state. For $Ra = 8000, Re = 500$, this behaviour is illustrated in the temporal intermittency of the near-wall transport properties such as the plane averaged shear, $\langle \mathrm{d}w/\mathrm{d}y|_{y=-h} \rangle_{x,z}$, and the Nusselt number, Nu, in figure 4.2(a). The breakdown from the longitudinal rolls towards the laminar state is evident in figure 4.2(b), where the bright and dark regions in the spacetime plot of near-wall spanwise and wall-normal perturbation kinetic energy, $\mathcal{E}_{u'+v'} = 1/2 \left[u'|^2_{(y^+,z)=(15,8\pi)} + v'|^2_{(y^+,z)=(15,8\pi)} \right]$ (where $\mathbf{u}' = \mathbf{u} - W_{lam}(y)$, $y^+ = u_\tau y_0/\nu$, $u_\tau = \sqrt{\langle \gamma/h \rangle_t}$, $y_0 = h - y = 0.44$, refer to perturbation velocities, dimensionless height, frictional velocity, wall-normal height respectively), highlight the presence of longitudinal rolls and spatially-localised laminar states. Figure 4.2(c) describes the spacetime plot of midplane temperature, $\theta|_{(y,z)=(0,8\pi)}$, where elongated red/blue lines correspond to regions of longitudinal rolls, while green spots indicate spatially-localised laminar states, highlighting the breakdown process. The near-wall transport properties, such as the Nusselt number and shear, exhibit strong correlations, peaking at $t = 3736$, corresponding to a spatially coherent longitudinal roll structure in figure 4.2(d,e). This is followed by a dip at $t = 6189$ and $t = 8680$, indicative of the breakdown towards the laminar state shown in figures 4.2(f,g) and 4.2(h,i) respectively. In other words, the longitudinal rolls enhance heat and momentum transfer across the wall, which is briefly disrupted by its breakdown towards the laminar state. However, exploring the

Figure 4.2: The intermittent rolls regime at $Ra = 8000, Re = 500$, $t \in [0, 10000]$. The time history of (a) Nusselt number, and shear, (b) near-wall wall-normal and spanwise perturbation kinetic energy, (c) midplane temperature spacetime plot, and their corresponding near-wall and midplane temporal planar snapshots at (d,e) $t = 3736$, (f,g) $t = 6189$, and (h,i) $t = 8680$.

spatiotemporal intermittency of this regime remains challenging in a large extended domain, To overcome this challenge, we consider a confined domain, $\Gamma = \pi/2$, where spatial intermittency could be artificially suppressed and discuss its temporal intermittent dynamics in §4.4.2.

4.3.3 Coexistence with turbulent bands

As Re approaches $Re = 1050$, shear-driven turbulence emerges as spatiotemporal intermittent turbulent-laminar bands, where turbulent and laminar regions can coexist (see references in §4.1.3). In the absence of buoyancy ($Ra = 0$), these bands emerge clearly, as shown in figure 4.3. The spacetime plot of the near-wall wall-normal and spanwise perturbation kinetic energy, $\mathcal{E}_{u'+v'}$, in figure 4.3(a) highlights this coexistence, where the turbulent and laminar regions are indicated by dark and bright areas, respectively. Notably, a period of prolonged laminar state is observed at $t = 1100, 4491, 6171$, represented by localised green regions in the midplane temperature spacetime plot, $\theta|_{(y,z)=(0,8\pi)}$, in figure 4.3(b). The prolonged laminar states are also evident in the near-wall and midplane temporal snapshots of figures 4.3(c-h), shown as large pockets of dark and green regions filling approximately half of the spatial domain. Next, we consider the influence of buoyancy on the turbulent-laminar bands and compare cases at $Ra = 0$ and $Ra = 10000$ at $Re = 1050$. At $Ra = 10000$, the features of the turbulent-laminar bands appearing as alternate dark and bright bands are visually consistent in the spacetime plot of near-wall wall-normal and spanwise perturbation kinetic energy, $\mathcal{E}_{u'+v'}$, in figure 4.4(a). However, key differences between the $Ra = 0$ case emerge. Notably, the midplane temperature snapshots, $\theta|_{(y,z)=(0,8\pi)}$, at $t = 1282, 5077, 6358$ in figures 4.4(d,f,g) reveal localised regions of streamwise-aligned red and blue stripes, indicating the presence of longitudinal rolls, which are absent in $Ra = 0$. These longitudinal roll regions are located next to neighbouring turbulent (bright) regions in the near-wall perturbation kinetic energy snapshots in figures 4.4(c,e,g), suggesting that longitudinal rolls coexist with turbulent patches at $Ra = 10000$. However, we caution that similar red and blue stripes are also observed in $Ra = 0$, where longitudinal rolls are not expected, likely suggesting the presence of quasi-streamwise rollers, shown in figure 4.3(f). Nonetheless, turbulence occurs more spatially intermittently at $Ra = 0$, containing prolonged pockets of laminar regions, while the turbulent-laminar bands at $Ra = 10000$ appear more visibly consistently (compare figures 4.3(a) and 4.4(a)). In other words, the presence of longitudinal rolls may promote turbulence locally, where prolonged regions of laminar patches do not appear. However, investigating this remains challenging due to the spatiotemporal nature of a large extended domain. To address this, we focus our analysis to a confined domain, $\Gamma = \pi/2$, where turbulent bands and longitudinal bands cannot coexist, thereby reducing spatial intermittency discussed further in §5.6.

Figure 4.3: Shear-driven turbulence regime at $Ra = 0$, $Re = 1050$, $t \in [0, 8000]$. Spacetime plots of (a) near-wall wall-normal and spanwise perturbation kinetic energy, (b) midplane temperature spacetime plot, and near-wall and midplane temporal planar snapshots at (c,d) $t = 1100$, (e,f) $t = 4491$, and (g,h) $t = 6171$, highlighting a prolonged laminar patch.

Figure 4.4: Shear-driven turbulence regime at $Ra = 100000, Re = 1050$, $t \in [0, 8000]$. Space-time plots of (a) near-wall wall-normal and spanwise perturbation kinetic energy, (b) midplane temperature spacetime plot, and their corresponding near-wall and midplane temporal $x-z$ planar snapshots at (c,d) $t = 1282$, (e,f) $t = 5077$, and (g,h) $t = 6358$, highlighting the coexistence of longitudinal rolls and turbulent bands.

4.4 The role of longitudinal rolls

4.4.1 The thermally-assisted sustaining process (TASP) in a confined domain

Motivated by the minimal flow unit (MFU) approach to study turbulence [?], we consider simulations confined to a confined domain defined by $\Gamma = \pi/2$, where the longitudinal rolls and localised turbulence could be spatially isolated. We first consider a numerical simulation at $Ra = 10000, Re = 1050$, in $\Gamma = \pi/2$, time integrated for $t \in [0, 3000]$. The initial condition has been sampled from a statistically stationary turbulent field at $Re = 2000$, which is then lowered slowly to $Re = 1050$. The time history from $t \in [0, 3000]$ of the near-wall transport properties such as the Nusselt number, Nu, shear, $\langle \mathrm{d}w/\mathrm{d}y|_{y=-h}\rangle_{x,z}$, volumetric temperature, $\theta(\mathbf{x})$, and near-wall streamwise and spanwise perturbation velocities snapshots, $w'|_{y^+=15}, v'|_{y^+=15}$, are presented in figure 4.5. In this confined domain, the dynamics of the system exhibit temporal intermittency, where the solution trajectory appears to wander between the longitudinal rolls and turbulent dynamics, marked by high and low near-wall transport properties, respectively. The turbulent dynamics mentioned here refer to chaotic trajectories (see §4.1.3) marked by a disordered volumetric temperature field and high near-wall transport quantities.

Starting from a longitudinal roll state of spanwise wavenumber of $\alpha d = 4$ at $t = 1291.5$ in figure 4.5(b), the solution erupts into turbulence at $t = 1480.5$, marked by a disordered temperature field in figure 4.5(c). During this breakdown, the near-wall snapshots of streamwise perturbation velocity, $w'|_{y^+=15}$, and wall-normal perturbation velocity, $v'|_{y^+=15}$, illustrated in the bottom panels of figures 4.5(c), reveal three pairs of high- and low-speed streaks, each with an average spanwise wavelength of $\Lambda_x^+ \approx 339/3 = 113$ (where $\Lambda_x^+ = u_\tau \Lambda_x / \nu$ refers to non-dimensionalised wavelength), close to the mean streak spacing ($\Lambda^+ \sim 100$) commonly reported in shear flow turbulence [????]. These streaks appear to be meandering, negatively correlated with wall-normal perturbation velocities, reminiscent of a streak breakdown process [?], or a bursting event [?], where high- and low-speed streaks are brought close to and away from the wall, respectively, enhancing near-wall transport quantities. Indeed, this is reflected by large increments of the Nusselt number and shear of roughly 40% at $t = 1480.5$ in figure 4.5(a). Subsequently, the solution trajectory returns to a longitudinal roll state at $t = 1564.5$, before erupting into turbulence at $t = 1711.5$ (see figures 4.5(d,e) respectively). This suggests that the turbulence has a finite lifetime, occurring transiently before decaying towards the laminar state at $Re = 1050$ [??], which is linearly unstable, leading to the onset of longitudinal rolls where transient turbulence could be re-excited again.

To test this hypothesis, we consider a numerical simulation at $Ra = 0$, $Re = 1050$, in $\Gamma = \pi/2$, where longitudinal rolls cannot appear. The initial condition is taken from a stationary turbulent solution at $Ra = 0$, $Re = 2000$, which is then lowered slowly to $Re = 1050$, and then time integrated for $t \in [0, 700]$. The time history of Nusselt number, Nu, shear, $\langle \mathrm{d}w/\mathrm{d}y|_{y=-h}\rangle_{x,z}$, and the volumetric temperature snapshots, $\theta(\mathbf{x})$, are reported in figure 4.6. Turbulence occurs transiently, which decays towards the laminar solution in $t \in [0, 700]$ within

Figure 4.5: Intermittent dynamics in a confined domain at $Ra = 10000$, $Re = 1050$, $t \in [0, 3000]$, $\Gamma = \pi/2$. The time history of the (a) Nusselt number and shear. Temporal snapshots of volumetric temperature, planar near-wall streamwise and spanwise perturbations at (b) $t = 1291.5$, (c) $t = 1480.5$, (d) $t = 1564.5$, (e) $t = 1711.5$. Longitudinal rolls and transient turbulence are observed at (b,d) and (c,e), respectively.

Figure 4.6: Relaminarisation in a confined domain at $Ra = 0$, $Re = 1050$, $t \in [0, 3000]$, $\Gamma = \pi/2$. The time history of the (a) Nusselt number and shear. Temporal snapshots of volumetric temperature at (b) $t = 31.5$, (c) $t = 63$, (d) $t = 157.5$, (e) $t = 672$.

the confined domain. As we compare the results between $Ra = 0$ and $Ra = 10000$, we propose that the longitudinal rolls at $Ra = 10000$ could provide a transition mechanism towards transient turbulence, which could be sustained indefinitely.

Next, we investigate the impact of longitudinal rolls on this proposed mechanism at different Ra. We perform four numerical simulations with an initial condition taken from $Ra = 10000, Re = 1050$, at $t = 850.5$ (before the onset of longitudinal rolls, see figure 4.5), which is lowered instantaneously to $Ra = 8000, 5000, 3000, 2000$ respectively. The initial conditions are time-integrated further to $t \in [850.5, 5000]$, and the time history of the shear, $\langle \mathrm{d}w/\mathrm{d}y|_{y=-h} \rangle_{x,z}$, and the temperature volumetric temporal snapshots, $\theta(\mathbf{x})$, of these 'Ra-quenching' experiment are presented in figure 4.7. The time history of shear is visibly intermittent for $Ra = 8000, 5000$, depicted as the orange and green trajectories in figure 4.7(a), similar to $Ra = 10000$. At $Ra = 8000, 5000$, the longitudinal rolls emerge at $t = 1312.5$ (see figures 4.7(d,f)), before erupting into turbulence at $t = 1743$ and $t = 3570$ in figures 4.7(e,g) respectively. This is then accompanied by a large spike in the near-wall transport properties before dipping briefly in figure 4.7(a). As Ra is lowered to $Ra = 3000, 2000$, the transients begin to decay into a longitudinal state from $t = 850.5$ to $t = 1312.5$, which remains asymptotically stable until $t = 4200$, represented as the red and purple trajectories of figures 4.7(i,k) respectively. This suggests that the longitudinal rolls become linearly unstable for $Ra = 8000, 5000$, leading to turbulence, while remaining stable for $Ra = 3000, 2000$. Notably, the longitudinal rolls state at $Ra = 5000$ remained saturated over a longer period $t \in [1500, 3400]$ (green curve of figure 4.7), suggesting an underlying linear instability with a smaller growth rate compared to $Ra = 8000$. We note that the longitudinal rolls in figure 4.7 have a spanwise wavenumber of $\alpha d = 4$, which corresponds to the wavenumber of the dominant primary instability (see Appendix A.4), indicating that it is the preferred wavenumber within the confined domain.

To determine the stability characteristics of the longitudinal rolls, we perform linear stability analysis about the longitudinal roll state ($\alpha d = 4$), at $Ra = 10000, 8000, 5000, 3000, 2000$. The details of linear stability analysis are described in §4.2.4, where λ and $\hat{\mathbf{s}}_\beta e^{i\beta z}$ refer to the eigenvalue and eigenmode. The longitudinal roll (base) states, $\mathbf{q}_{LR}$, are obtained by time integrating an initial condition consisting of the laminar (conduction) state, superimposed by the primary eigenmode, $\alpha d = 4$, at $Ra = 10000, 8000, 5000, 3000, 2000$, in a two-dimensional $x - y$ plane, suppressing any three-dimensional perturbations numerically. The growth rates as a function of discrete streamwise wavenumbers, $2 \leq \beta d \leq 5$, are presented in figure 4.8. We note that the admissible streamwise wavenumbers within $\Gamma = \pi/2$ are $\beta d = m$, where m is a positive even integer, $m = 2, 4, ..$, and $\beta d = 3, 5$ are included for completeness. The longitudinal rolls are linearly unstable for $Ra \geq 5000$, while they remain stable for $Ra \leq 3000$, confirming our hypothesis earlier. Notably, the growth rates between $Ra = 5000$ and $Ra = 10000$ differ by an order of magnitude, which could explain the prolonged period of saturation in the green curve of figure 4.7(a,b). The dominant secondary instability of longitudinal rolls in $\Gamma = \pi/2$ has a streamwise wavenumber of $\beta d = 2$. Using a standard quadratic regression, the critical Rayleigh number for disturbances with $\beta d = 2$ is approximately $Ra_s \approx 4720$, presented in

Figure 4.7: *Ra*-quenching experiments for $Ra = 8000, 5000, 3000, 2000$, $Re = 1050$, $\Gamma = \pi/2$, $t \in [850.5, 5000]$. The time history of (a) shear and (b) volumetric temperature snapshots of the initial condition at $t = 850.5$. Volumetric temperature snapshots for $Ra = 8000$ at (c,d) $t = 1312.5, 1743$, and $Ra = 5000$ at (e,f) $t = 1312.5, 3570$, revealing a longitudinal roll and a turbulent state, respectively. Stable longitudinal rolls emerge for $Ra = 3000$ at (g,h) $t = 1312.5, 4200$, and $Ra = 2000$ at (j,k) $t = 1312.5, 4200$.

Figure 4.8: The growth rates of infinitesimal perturbations linearised about longitudinal rolls, $\mathbf{q}_{LR}$, of spanwise wavenumber of $\alpha d = 4$, against (a) streamwise wavenumber λ, and (b) Ra for $\beta d = 1$. The hatches in (a) refer to wavenumbers smaller than those admissible in $\Gamma = \pi/2$. The dash-dotted line in (b) is a standard quadratic regression yielding $Ra_s \approx 4720$.

figure 4.8(b).

Following this, we examine the dominant unstable manifold ($\beta d = 2$) of the longitudinal rolls, by considering an initial condition,

$$\mathbf{q}_0(\mathbf{x}, t = 0) = \mathbf{q}_{LR}(x, y) + \hat{\mathbf{q}}_\beta(x, y)e^{i\beta z}, \tag{4.10}$$

which is prescribed to equation (4.1). Here, $\hat{\mathbf{q}}_\beta e^{i\beta dz}$ is an eigenmode at βd, and the amplitude of which was scaled such that its total energy is defined by,

$$\delta = \frac{1}{V}\int_\Omega \hat{\mathbf{u}}(\mathbf{x})^T\hat{\mathbf{u}}(\mathbf{x}) + \frac{Ra}{8Re^2 Pr}\hat{\theta}(\mathbf{x})^2 \, d\Omega \approx O(10^{-3}) \tag{4.11}$$

is considered. We have also considered that $\delta = 10^{-2}, 10^{-4}$, where $\delta = 10^{-3}$ was found to be sufficiently small enough to ensure linear growth, while large enough to be computationally practical.

The initial condition is time integrated from $t \in [0, 8000]$, and its time history of near wall transport properties such as the Nusselt number, Nu and shear, $\langle dw/dy|_{y=-h}\rangle_{x,z}$, midplane temperature spacetime plot, $\theta|_{(y,z)=(0,\pi)}$, volumetric temperature, $\theta(\mathbf{x})$, and near-wall streamwise and spanwise perturbation velocities snapshots, $w'|_{y^+=15}, v'|_{y^+=15}$, are presented in figure 4.9. The intermittent trajectory is visually present, oscillating between the longitudinal rolls and transient turbulence over four cycles $t = [0, 8000]$, marked by regions of low and high near-wall transport quantities in figure 4.9(a) and alternating between organised and disorganised longitudinal rolls in figure 4.9(b). The snapshots of figure 4.9 illustrate the volumetric temperature field, planar near-wall streamwise and wall-normal perturbations, resembling the longitudinal rolls ($LR1-4$), and transient turbulent states ($T1-4$). As the solution emerges from the unstable manifold of the longitudinal roll state, ($LR1$) in figure 4.9(c), the trajectory erupts into turbulence at $t = 1512$, marked by a disordered volumetric temperature field with high- and low-speed streaks in snapshot ($T1$) in figure 4.9(c). These high- and low-speed streaks are negatively spatially-correlated with wall-normal perturbation velocities in figure 4.9(d), reminiscent of sweeps and ejection events commonly found in turbulent shear flows [??]. Notably, the flow structures in snapshot $T1$ in figure 4.9(d), appear visibly symmetric along the centerline of the channel, $x^+ \approx 162$ (where $x^+ = u_\tau x/\nu$ refers to the non-dimensionalised spanwise coordinate), comparable to the invariant states identified in transition shear flows [?????]. Turbulence occurs transiently, and the solution decays towards a longitudinal roll-liked state at $t = 2446.5$, shown by snapshot ($LR2$) in figure 4.9(e), thereby completing one single cycle. We note that the snapshot ($LR2$) does not strictly resemble the longitudinal roll state at snapshot ($LR1$), however, we show that they are similar and reside close by in state space, as we shall see later. The intermittent cycle repeats over three subsequent intervals, where the turbulent dynamics and longitudinal rolls emerge at $t = 2992.5, 5103, 6993$, and $t = 3727.5, 6300$, represented as snapshots ($T2, 3, 4$) and ($LR3, 4$) in figures 4.9(f,h,j) and 4.9(g,i) respectively.

Here, we showed that the dominant unstable manifold of the longitudinal rolls is linked to turbulent dynamics, a transition mechanism based on linear instability. Interestingly, a 'single'

Figure 4.9: Integrating along the dominant unstable manifold, $\beta d = 2$, of the longitudinal rolls at $Ra = 5000, Re = 1050, \Gamma = \pi/2$, $t \in [0, 8000]$. Time history of the (a) Nusselt number and shear, and (b) midplane temperature spacetime plot. This system oscillates between the longitudinal rolls $(LR1-4)$ and turbulence $(T1-4)$ over four intervals. Snapshots of volumetric temperature and near-wall streamwise and spanwise velocity perturbations at (b) $t = 105$, (c) $t = 1512$, (d) $t = 2446.5$, (e) $t = 2992.5$, (f) $t = 3727.5$, (g) $t = 5103$, (h) $t = 6300$, (i) $t = 6993$.

longitudinal roll with $\alpha d = 2$ emerges after turbulence decays, shown as snapshot ($LR3$). This suggests that other unstable manifolds may be linked to the transition to transient turbulence.

To visualise the temporal dynamics in figure 4.9 with better clarity, we project the solution trajectory onto state observables using the planar averaged centerline velocity, $\langle w|_{y=0}\rangle_{x,z}$, shear, $\langle \mathrm{d}w/\mathrm{d}y|_{y=-h}\rangle_{x,z}$ coloured by the volume normalised perturbation kinetic energy, $1/(2V)||\mathbf{u}'||^2$, in figure 4.10. These observables seek to distinguish the region of turbulent dynamics, longitudinal roll state, and laminar state residing in near $(0.82, 3.2)$, $(0.90, 2.32)$ and $(1, 2)$, respectively. This separation is further supported by the location of the temporal snapshots between $(T1-4)$ and $(LR1-4)$, organised near the turbulent dynamics and in longitudinal roll state, $\mathbf{q}_{LR,\alpha d=4}$, setting them apart. We emphasise that the unstable longitudinal roll state, $\mathbf{q}_{LR,\alpha d=4}$, and laminar states denoted by open circles are unstable equilibria, while the snapshots longitudinal roll, $(LR1-4)$, and turbulent snapshots, $(T1-4)$, denoted by black crosses, are not.

The solution trajectory emerges from the unstable manifold of the longitudinal rolls, $\mathbf{q}_{LR_{\alpha d=4}}$, evolving towards turbulent dynamics around $(0.85, 3.2)$, denoted by high shear. Turbulence is transient, occurring with a finite lifetime [**??**], eventually decaying towards the laminar state. As the solution trajectory approaches the laminar solution $(1, 2)$, it abruptly reverses towards the longitudinal roll state near $(0.95, 2.15)$, $(LR3)$. Subsequently, the solution trajectory could depart along the unstable manifold of the longitudinal rolls again, leading to the onset of turbulence, where the cycle repeats.

To determine if this cycle could be sustained indefinitely, we consider a longer time horizon, $t \in [0, 68750]$, illustrated in figure 4.10(b). The solution trajectory wanders between the 'cloud' of chaotic transient turbulence at the top left corner (in red), and longitudinal roll and laminar state (in blue) in the bottom right, forming a basin of attraction between the unstable longitudinal rolls, transient turbulence and the laminar state. We suggest that this basin of attraction, is likely established above a critical Ra as the longitudinal rolls become linearly unstable (i.e $Ra \gtrsim Ra_s \approx 4720$, see figure 4.8(b)), providing an intermediate pathway towards transient turbulence, which could be regenerated again - a 'self-sustaining' dynamical process. We refer to this sustaining process as the *thermally-assisted sustaining process (TASP)*, inspired by the self-sustaining process (SSP) from turbulent shear flows [**?**].

4.4.2 Variation of Ra and Re on the thermally sustained turbulent process within $\Gamma = \pi/2$

In this section, we explore the behaviour of the *TASP* as Re and Ra are varied. We consider eight different cases at $Ra = 8000, 4000$ and $Re = 600, 700, 1000, 1400$. The results of these eight cases, where longitudinals rolls are either unstable at $Ra = 8000$ or stable at $Ra = 4000$, are shown in figure 4.11, depicting the spacetime plots of midplane temperature, $\theta|_{y=0}(x,t)$, time history of the Nusselt number, Nu, and shear, $\langle \mathrm{d}w/\mathrm{d}y|_{y=-h}\rangle_{x,z}$ and state space projection using the planar averaged centerline velocity, $\langle w|_{y=0}\rangle_{x,z}$, shear, coloured by the volume normalised perturbation kinetic energy, $\frac{1}{2V}||\mathbf{u}'||^2$. For all cases except $Ra = 4000$, $Re = 1000$ and $Re = 1400$, their initial conditions are prepared from the laminar state, superimposed by a random

Figure 4.10: State space projection based on the planar averaged centerline velocity and shear, coloured by the volume normalised perturbation kinetic energy at $Ra = 5000$, $Re = 1050$, $\Gamma = \pi/2$, (a) $t \in [0, 800]$, (b) $t \in [0, 68750]$. The open black circles represent the unstable equilibria of longitudinal rolls and the laminar state. Note that the black-crosses, labelled by (T1-4) and (LR1-4), refer to temporal snapshots in figure 4.9, not equilibria solutions.

Figure 4.11: The behaviour of the unstable and stable longitudinal rolls at $Ra = 8000, 4000$ for (a,e) $Re = 600$, (b,f) $Re = 700$, (c,g) $Re = 1000$ and (d,h) $Re = 1400$ within $\Gamma = \pi/2$. Each parameter regime consist of three panels from the top to bottom, depicting the midplane temperature spacetime plot, $\theta|_{(y,z)=(0,\pi)}$, time history of the Nusselt number and shear, and state space projection based on the planar averaged centerline velocity and shear, coloured by the volume normalised perturbation kinetic energy.

noise based on a Gaussian distribution with zero mean and unit variance, scaled to a total energy of $\delta = 10^{-3}$ (see definition in equation (4.11)). For the exceptional cases at $Ra = 4000$, $Re = 1000$ and $Re = 1400$, where subcritical turbulence and stable longitudinal rolls are expected, their initial conditions are obtained by gradually lowering Re from a statistically stationary turbulent solution at $Re = 2000$. We note that we have not explicitly performed a linear stability analysis of the longitudinal rolls for the parameter regime in figure 4.11, however, they appear to be unstable at $Ra = 8000$, while being stable at $Ra = 4000$ from DNS.

At $Ra = 8000$, $Re = 1000$, $t \in [0, 10000]$ in figure 4.11(c), the trajectory visits the transient turbulent regime near $t = 7200$, which decays towards the longitudinal roll state, $\mathbf{q}_{LR}$, at $t = 7400$, which could be regenerated again, consistent with the $TASP$ in §4.4.1. As Ra is lowered to 4000, the solution trajectory decays towards the longitudinal roll state, $\mathbf{q}_{LR}$, where the $TASP$ disappears. In this case, the longitudinal rolls are linearly stable, confirming our hypothesis earlier that the $TASP$ is only established when longitudinal rolls become linearly unstable above a certain Ra-threshold (i.e $Ra \gtrsim Ra_s \approx 4720$).

At $Re = 1400$, $Ra = 4000$, the solution trajectory remains within the turbulent 'cloud' near $(0.8, 3.8)$ illustrated in figure 4.11(h), suggesting that turbulence might be sustained indefinitely, in which the turbulent chaotic saddle at $Re = 1000$ could be transformed into a chaotic attractor at $Re = 1400$. As Ra is increased to 8000, the solution trajectory originating from the laminar state, evolves towards the unstable longitudinal roll state, $\mathbf{q}_{LR}$ at $t = 1550$, transitioning into sustained turbulence at $t = 1800$. Therefore, the linearly unstable longitudinal rolls serve as an intermediate transitional pathway between the laminar state and subcritical turbulence, whereas at $Ra = 4000$, a bistability between stable longitudinal rolls (not shown) and turbulence is established.

Next, we examine the behaviour of $TASP$ as Re decreases towards the intermittent regime at $Re = 600, 700$, where a periodic orbit emerges between the longitudinal roll and the laminar state. At $Re = 600$, $Ra = 8000$ in figure 4.11(a), the solution trajectory initially evolves towards the longitudinal roll state, $\mathbf{q}_{LR}$, which is linearly unstable and breaks down towards the laminar state at $t = 2200$. This breakdown is evidenced by the trajectory's proximity to the laminar state in state space and the presence of a narrow green patch in the midplane temperature spacetime plot. The longitudinal roll state is regenerated again, forming a periodic orbit with a period of $T_{period} = 8098 - 6108 = 1990$, oscillating between the longitudinal roll and laminar state over five intervals within $t \in [0, 10000]$. As Re increases slightly to 700, the periodic orbit persists over a shorter period of $T_{period} = 3889 - 3386 = 503$. A notable difference is observed in the regenerated longitudinal rolls, which is continuously translated by $L_x/2$ in the x-direction. Additionally, as Re increases from 600 to 700, the trajectory moves further away from the laminar state during breakdown, suggesting an increasing attraction towards the longitudinal roll state, $\mathbf{q}_{LR}$ (compare $t = 2200$ in figure 4.11(a) and $t = 2750$ in figure 4.11(b)). When Ra is lowered to $Ra = 4000$, the periodic orbit disappears and the trajectory stabilises into the longitudinal roll state, $\mathbf{q}_{LR}$, at $Re = 600, 700$.

To summarise the dynamical processes identified in figure 4.11, we present a state space

Figure 4.12: A state space sketch of figure 4.11 at $Ra = 8000$, (a) $Re = 600$, (b) $Re = 700$, (c) $Re = 1000$, (d) $Re = 1400$ and $Ra = 4000$ at (e) $Re = 600, 700$, (f) $Re = 1000$, (g) $Re = 1400$. The longitudinal roll is linearly unstable (saddle) at $Ra = 8000$, and is stable at $Ra = 4000$, whereas the laminar state is always linearly unstable (saddle). The blue and orange solid arrows refer to the unstable manifold of longitudinal rolls and the laminar state. The red solid lines denote the chaotic trajectories of turbulence, likely forming a chaotic saddle at $Re = 1000$ and a chaotic attractor at $Re = 1400$. The black-dashed trajectories refer to possible solution trajectories, forming a periodic orbit (P.O) at $Ra = 8000$, $Re = 600, 700$, and a basin of attraction (B.o.A) at $Ra = 8000, Re = 1000$. We note that invariant states could exist at $Ra = 4000, Re = 600, 700$, labelled as a saddle here [?].

sketch of it in figure 5.21. At $Ra = 8000$, $Re = 600$ and $Re = 700$, the longitudinal rolls become linearly unstable, breaking down into the laminar state before being regenerated, forming a periodic orbit illustrated enclosed by black dotted paths in figures 5.21(a,b). For $Re = 700$, the regenerated longitudinal roll is continuously translated by $L_x/2$, suggestive a possible merger of two periodic orbits into one sketched in figure 4.11(b). Future bifurcation studies are required to establish this, providing an avenue for future work. As Ra is lowered to $Ra = 4000$, the laminar state stabilises into the longitudinal rolls in figure 5.21(e). This regime may contain invariant solutions [?], denoted as saddle points here. Integrating along the unstable manifold of longitudinal rolls at $Ra = 8000, Re = 1000$ leads to transient turbulence, which eventually decays to the laminar state before regenerating into longitudinal rolls again, forming the *TASP* in figure 5.21(c). In contrast, at $Ra = 4000, Re = 1000$, the longitudinal rolls become linearly stable, eliminating the intermediate (orange) pathway toward turbulence where transient turbulence stabilises into longitudinal rolls shown as the black-dashed trajectory in figure 5.21(f). For $Ra = 8000, Re = 1400$, the linearly unstable longitudinal rolls provide an intermediate pathway towards turbulence from the laminar state sketched in figure 5.21(d), breaking the bistability between the laminar state and subcritical turbulence seen at $Ra = 4000$ in figure 5.21(g). This behaviour resembles the nature of subcritical turbulence in shear-driven flow, highlighting the contribution of unstable longitudinal rolls towards the transition to turbulence within $\Gamma = \pi/2$.

We examined the dynamics of unstable longitudinal rolls as the Reynolds number, Re, and Rayleigh number, Ra, are varied, identifying three key dynamical processes: (1) periodic orbits between longitudinal rolls and the laminar state (figure 5.21(a,b)), (2) the *TASP*, where transient turbulence can be sustained (figure 5.21(c)) and (3) an intermediate transitional pathway towards sustained turbulence (figure 5.21(d)). To establish a connection between these processes and understand their transitional boundaries, we conduct a parameter sweep over $Ra \in [4000, 10000]$ and $Re \in [600, 1400]$ within $\Gamma = \pi/2$. Figure 4.13 presents the midplane temperature spacetime plot alongside the time history of shear, $\langle \mathrm{d}w/\mathrm{d}y|_{y=-h} \rangle_{x,z}$ and the Nusselt number, Nu. For all simulations, the initial conditions are prepared from the laminar state, superimposed with a random noise based on a Gaussian distribution with zero mean and unit variance, scaled to a total energy of $\delta = 10^{-3}$ (see definition in equation (4.11)). Due to the subcritical nature of turbulence and expected stable longitudinal rolls, exceptions are made for $Ra = 4000$, $Re \in [900, 1400]$, where initial conditions are taken from gradually lowering Re from a statistically stationary turbulent state at $Re = 2000$. The *thermally-assisted sustaining process* is highlighted in green for $Ra \in [5000, 10000]$ and $Re \in [900, 1200]$, where temporally intermittent shear and Nusselt number fluctuations are observed, accompanied by a mixture of organised and disorganised flow structures in the temperature spacetime plots. In this regime, the longitudinal rolls provide an intermediate pathway towards transient turbulence, which appears linearly unstable for $Ra \geq 5000$. Below this threshold, transient turbulence decays into stable longitudinal rolls, as observed at $Ra = 4000$, $Re \in [900, 1200]$ labelled as 'transient turbulence'. Periodic orbits between longitudinal rolls and the laminar state occur

for $Ra \in [6000, 10000]$ and $Re \in [600, 800]$, establishing above a critical $Ra - Re$ threshold, below which solutions stabilise into longitudinal rolls shaded in red. Notably at $Re = 800$, the periodic orbit becomes increasingly quasi-periodic, likely related to the *TASP* near $Re \sim 900$. Despite longitudinal rolls being linearly stable at $Ra = 4000, Re = 1400$ (not shown), turbulence is sustained, shaded in blue across $Re = 1400$. In this case, a bistable system forms between longitudinal rolls and turbulence at $Ra = 4000$, while the longitudinal rolls provide an intermediate pathway towards turbulence for $Ra \geq 5000$. Figure 4.13 underscores the role of unstable longitudinal rolls in transitional RBP flows within confined domains.

4.4.3 Extending to large domains, $\Gamma = 4\pi$.

In this section, we bridge the gap between the confined and large domains by discussing the relevance of dynamical processes within the confined domains to the large domains, $\Gamma = 4\pi$. We will focus on the intermittent roll and shear-driven turbulence regime at $Ra = 500, 750, 1000, 1050$ for $Ra = 10000$ presented by figure 4.14, illustrating their spacetime plots of midplane temperature, $\theta|_{(y,z)=(0,8\pi)}$, and near-wall wall-normal and spanwise perturbation kinetic energy, $\mathcal{E}_{u'+v'}$. Additionally, we also examine the probability distribution functions based on the centreline-velocity normalised midplane velocity and temperature, $f(w|_{y=0}, \theta|_{y=0})$. At $Ra = 10000$, $Re = 500$, the breakdown of longitudinal rolls towards the laminar state is observed, highlighted by spatially-localised green spots in the midplane temperature plots, and dark regions in the near-wall perturbation kinetic energy spacetime plot near $t = 500, 3800$ in figure 4.14(a,b) respectively. As Re increases from 500 to 750, the breakdown towards the laminar state remains visually apparent. The spatiotemporal dynamics between longitudinal rolls and the laminar state within the intermittent regime in the large domain are reminiscent of the periodic orbit identified between them in a confined domain. There is a noticeable decrease in the number of green and dark regions between figures 4.14(a,b) and (d,e), suggesting fewer laminar events at $Re = 750$. Indeed, this difference is further reflected in their PDFs, where the probability of laminar events, at $(w|_{y=0}, \theta|_{y=0}) = (1, 0)$, depicted as the 'head' of the 'arc-shaped' PDF decreasing from $Re = 500$ (figure 4.14(c)) to $Re = 750$ (figure 4.14(f)). This likely suggests fewer laminar state events and more occurrences of the longitudinal roll state, as the solution trajectory becomes increasingly attracted towards the longitudinal roll state from $Re = 600$ and $Re = 700$ at $Ra = 8000$ in the confined domain presented in figures 4.11(a,b).

At $Re = 1000$, we observe the coexistence of the laminar state, the longitudinal rolls and transient turbulence appearing as dark, bright and very bright regions in the near-wall wall-normal and spanwise perturbation velocities, normalised by thermal velocity scale, $\mathcal{E}_{u'+v'}/u_\kappa^2$ (where $u_\kappa = \kappa/d$) in figure 4.14(h). Starting at $t = 2000$, the longitudinal rolls appearing as red/blue elongated strips in figure 4.14(g) erupt into turbulence at $t = 2500$, appearing as very bright spots in figure 4.14(h). Turbulence is transient, decaying towards the laminar state at $t = 3000$, as indicated by the dark patches in figure 4.14(h). By $t = 4000$, longitudinal rolls are regenerated, appearing as red/blue elongated strips in figure 4.14(g). This process resembles *TASP* in a confined domain (figure 5.21(c)), suggesting that a similar process may be present

Figures/RaEffectOnTurbulence/ConsolidatedPlot-full-annotated.pdf

Figure 4.13: The temperature spacetime plots and time history of shear and the Nusselt number for $Ra \in [5000, 10000]$, $Re \in [600, 1400]$ within $\Gamma = \pi/2$. Unstable longitudinal rolls lead to the onset of (1) periodic orbits (yellow), (2) the *thermally-assisted sustaining process* (green), and (3) sustained turbulence (blue), occurring beyond an $Ra - Re$ boundary, below which

Figures/RaEffectOnTurbulence/Ra10000-MidSpaceTimeAndPDFs.pdf

Figure 4.14: The midplane temperature spacetime plot, and near-wall wall-normal and spanwise perturbation kinetic energy by normalised by thermal velocity scale, u_κ, and the probability density functions based on planar-averaged centerline velocity and the midplane temperature at $Ra = 10000$, (a,b,c) $Re = 500$, (d,e,f) $Re = 750$, (g,h,i) $Re = 1000$, (j,k,l) $Re = 1050$.

in the large domain.

As Re approaches $Re = 1050$, turbulence becomes sustained, forming distinct turbulent-laminar bands as seen in figure 4.14(k,h). The increase in turbulent events is reflected by the PDFs, where a 'D'-shaped PDF absent in $Re = 750$, gradually increases in intensity from $Re = 1000$ to $Re = 1050$. The lack of prolonged laminar spots, previously identified for $Ra = 0$ (figure 4.3 suggests that the longitudinal rolls provide an intermediate pathway towards turbulence in a small domain (figure 4.11(d)).

4.5 Conclusions

We conclude by summarising the key findings of transitional RBP from figure 4.1, where we identify five different regimes and their transition boundaries. First, we examined the bistability between SDC and ISRs in RBP flows, which persists up to $Re = 1$, beyond which only ISR solutions are observed. The critical Re_s at which SDC disappears likely depends on Re and remains an avenue for future study. At $Re = 10$, the wavenumber of the stable ISRs adheres to the stability boundaries of the Busse balloon, and we observe longitudinal rolls as well as oscillatory longitudinal rolls, expected from the secondary instabilities of RBC [?]. Wavy rolls appear at $Re = 100$, $Ra \geq 5000$ [??], but disappear for $Re \geq 500$, where a new regime referred to as the intermittent rolls emerges. This regime is characterised by the spatiotemporal intermittent breakdown of longitudinal rolls towards the laminar state, before being regenerated again. Similar to the wavy rolls regime, intermittent rolls only appear above a Ra-threshold, $Ra \geq 5000$ (see figure 4.1), below which longitudinal rolls persists. Notably, the wavenumber of these longitudinal rolls lies outside of the stability boundaries of the Busse balloon for RBC ($Re = 0$), suggesting the stability boundaries are modified as Re increases, a potential avenue for future work. As Re approaches the shear-driven turbulent regime, we observe the coexistence of longitudinal rolls with neighbouring turbulent bands at $Ra = 10000$, highlighting the role of the spatiotemporal nature of longitudinal rolls in transitional RBP.

To investigate the role of longitudinal rolls in transitional RBP, we consider a confined domain, $\Gamma = \pi/2$, where spatial intermittency can be artificially suppressed. Integrating along the unstable manifold of longitudinal rolls in the confined domain leads to transient turbulence, which eventually decays towards the laminar state before longitudinal rolls re-emerge again. Transient turbulence can be sustained here, referred to as the *thermally-assisted sustaining process (TASP)*. To understand *TASP* further, we explore its behaviour as Re and Ra are varied. As Re decreases towards the intermittent rolls regime, a periodic orbit emerges, oscillating between the longitudinal roll and a laminar state. In contrast, as Re increases, shear-driven turbulence becomes sustained, with the longitudinal rolls providing an intermediate route towards the transition to turbulence from the laminar state. Our investigation of the role of unstable longitudinal rolls within confined domains revealed three dynamical processes: the onset of (1)periodic orbits, (2) the *TASP*, and (3) providing an intermediate route towards turbulence. It was also shown that the stability of longitudinal rolls largely depends on Re and Ra, below

which only stable longitudinal rolls are observed. Furthermore, the connection between the dynamical process identified here to the onset of wavy rolls warrants further investigation. We also acknowledge that more spatially subharmonic instabilities may arise as the domain size increases.

Finally, we assess the relevance of our findings in the confined domain and their connection to the large domain. We suggest that the breakdown towards the laminar state in the intermittent roll regime bears qualitative similarities to the periodic orbit between them in the confined domain. Furthermore, transient turbulence that is sustained by longitudinal rolls is also evident in the large domain, where the flow transitions between transient turbulence, longitudinal rolls and the laminar state in figures 4.14(g,h). At $Re = 1050$, the turbulent-laminar bands dominate, weakly dependent on Ra, as suggested by figure A.2. It may be possible that these turbulent-laminar bands decay spontaneously towards the laminar state [??], and their lifetime statistics may depend on Ra, which warrants further investigation. However, if the $TASP$ persists above a critical Ra providing a pathway to turbulence, then the turbulent-laminar bands could be sustained indefinitely. As Re approaches 2000, featureless turbulence emerges, with the first- and second-order statistics becoming independent of Re, indicating fully developed turbulence. It is likely that the range of $Ra \in [0, 10000]$ considered here is too low to significantly influence shear-driven turbulence at $Re = 2000$, suggested by the studies of turbulent RBP [?].

Chapter 5

The state space structure of Spiral Defect Chaos

5.1 Introduction

Rayleigh-Bénard convection (RBC) concerns the fluid motion confined between two parallel walls, separated by a distance d, heated from below. The motion of the fluid is effectively driven by unstable stratification due to temperature gradients ($\Delta T/d$) across the walls. Given a large enough temperature gradient, a non-trivial fluid motion occurs, often developing into a spatially varying structure known as a convection pattern. This motion is described in terms of the Rayleigh number $Ra = \alpha g d^3 \Delta T/\nu\kappa$, Prandtl number $Pr = \nu/\kappa$ and aspect ratio of the experimental/computational domain $\Gamma = L/d$, where $\alpha, g, \Delta T, \nu, \kappa, L$ refers to the thermal expansion coefficient, acceleration due to gravity, temperature difference between the bottom and top wall, kinematic viscosity thermal diffusivity, domain's length and span respectively. An important question that underpins RBC is often as follows: Given the Rayleigh number (Ra), Prandtl number (Pr) and aspect ratio (Γ) of a fluid system, what convection pattern arises and what is its associated heat flux?

5.1.1 Multiple convection states

While the Busse balloon describes the stability of ISRs over a continuum of wavenumbers (at given Ra and Pr), predicting the wavenumber of an ISR state remains an ongoing challenge **?**. Experimental investigations of RBC in moderate domains ($\Gamma \geq 7$) showed that ISRs in rectangular (straight rolls) and cylindrical (concentric rolls) domains are stable. Consider $\varepsilon (\equiv (Ra - Ra_c)/Ra_c$, where Ra_c is the critical Ra for the onset of linear instability for ISRs) as a control parameter referred to as the reduced Rayleigh number. As ε is increased continuously from below the onset, the initial ISRs become unstable and transform into another set of ISRs with a different wavelength. With the marginal increase of ε, this process is repeated and the ISRs undergo hysteretic transverse wavelength adjustments, adhering to the stability boundaries of the Busse balloon **??**. When ISRs become unstable, roll dislocations and defects

can be nucleated near the boundary or bulk, modifying the effective roll wavenumber as they travel through the domain **?**. This observation implies that the wavenumber of an ISR state depends on the state's history or the system's initial condition **?**.

It is worth noting that the solutions in the form of ISRs appear to be an exception rather than the rule **?**. The coexistence of multiple 'non-ISR' states, in the form of squares, travelling/stationary targets, giant rotating spirals, and oscillatory convection patterns have been found over several years **??????**. Investigation of cylindrical RBC with small aspect-ratio ($\Gamma = 2$) revealed eight stationary states (at the same $Ra = 142000$), and two oscillatory states ($Ra > 14200$) **?**. These findings were later supported by numerical experiments and bifurcation analyses **???**. In particular, bifurcation analyses performed by **?**, revealed twelve stable branches in the form of symmetric and asymmetric convection rolls near onset ($Ra \leq 2500$), with the potential emergence of hundreds of branches at higher Rayleigh numbers, $Ra \leq 30000$ **?**. In larger domains ($\Gamma \geq 28$), giant rotating spirals were identified and thoroughly investigated **??**. Experimental and numerical studies of RBC with varying sidewall boundary conditions (i.e. thermally insulating, conducting and no-slip) **????**, non-Boussinesq convection **??**, and rotational effects **?** were investigated, where multiple states were also reported. More recently, **??** computed up to sixteen stable and unstable invariant states and identified heteroclinic orbits between the multiple states in an inclined RBC.

5.1.2 Spiral defect chaos

Convection rolls exhibiting spatio-temporal chaotic behaviour known as spiral defect chaos (SDC) are found in the same parameter space of ε, where ISRs were expected **???????????**. It is well established that SDC exists as an intrinsic state of RBC, independent of sidewall conditions **?**. SDC has also been found in numerical simulations of the two-dimensional Swift-Hohenberg equations **?????**. Some investigations into quantifying the onset of SDC in terms of Rayleigh number remain inconclusive. The critical reduced Rayleigh number for the onset of SDC, ε_s, has been observed to decrease with increasing Γ, and increase with increasing Pr **?????**. It is worth noting that SDC has been reported in larger domains ($\Gamma \geq 20$) only, implying that there exists a minimal Γ for SDC to occur **?**, further supporting the dependence of ε_s on Γ mentioned above. This is also consistent with the leading Lyapunov exponents, which become smaller with decreasing aspect ratios, Γ, albeit at larger $\varepsilon = 2.5$ **??**. Investigations into the spatial-temporal characteristics of SDC, such as the quantification of the averaged roll-curvature **??**, probability of spirals **??** and correlation length-/time-scales **???** have been studied. Specifically, the correlation length-scales **???** of SDC appear to scale exponentially as ε is increased. Furthermore, spatio-temporal chaotic behaviour reminiscent to SDC has been found in other pattern-formation systems such as rotational RBC **?**, dielectric barrier discharge **?** and chemical systems **?**.

Given the co-existence of ISRs and SDC in the parameter space of ε, it is known that they form bistability at $Pr \approx 1$ in a spatially extended domain, supported by experiments over a range of $\varepsilon(> 0)$ **?**. Only carefully prepared experiment setups led to ISRs while most

initial conditions yield SDC. In other words, the asymptotic state of RBC depends on its initial conditions, reminiscent of the hysteretic behaviour of RBC discussed in §5.1.1. The chaotic state of SDC is unstable at $Pr = 4$, where multiple spiral patterns coarsen into a single spiral, before evolving into straight-curved rolls over a long period **?**. This implies that the behaviour of SDC depends on Pr.

5.1.3 Scope of this study

The bistability between SDC and ISR is well established, but this also opens a question of how it is connected with the previous findings of multiple stable states. It is worth noting that a possible parameter in exploring this connection appears to be the domain size. Bistability has been reported in domains much larger ($\Gamma = 50$) than the multiple states found in small-to-moderate domains ($\Gamma \leq 10$) **?**. Furthermore, giant rotating spirals have been found in domains comparable to the horizontal length scale of SDC **??**. Under this premise, the scope of this study is to explore how SDC, ISRs and multiple states are linked within the state space, where stable/unstable equilibria and their manifolds (or linear stability) could provide useful physical insights into the state transition dynamics.

Motivated by the observation that SDC consists of several localised structures that resemble multiple states (i.e. travelling waves, spirals, asymmetric states), we first seek to isolate these states by minimising the domain systematically. Confined within the minimal domain, SDC is found to appear only transiently and does not sustain for a long time. The transient SDC state eventually stabilises into a large number of stable multiple states, which will be referred to as the 'elementary' states of SDC, and they are subsequently found within the minimal domain. As we shall see later, these elementary states remarkably resemble local structures of SDC observed in wide computational domains, indicating that they possibly underpin the formation of SDC. Next, the state-space boundaries between SDC and ISRs are explored by employing the edge-tracking technique **??**, unveiling the existence of multiple edge states sitting on the boundaries. Finally, to understand the role of the unstable ISRs outside the Busse balloon, we perform a series of numerical experiments, in which a small perturbation is added along the unstable manifolds of several (unstable) ISRs outside of the Busse balloon. We shall see that some of their unstable manifolds are connected to stable ISRs within the Busse balloon, while the others are linked to transient SDC, which is subsequently stabilised into an elementary state. This suggests that some of the unstable ISRs act as signposts for the state-space boundary between stable ISRs and SDC (and/or elementary states).

The main contributions of the present study can be briefly summarised as follows:

1. Discovery of a number of stable invariant solutions which underpin the localised structures of SDC by minimising the computational domain for SDC (sectisn 5.3);

2. Computation of some of multiple 'edge states' sitting on the separatrix between SDC and ISRs (section 5.4);

3. Several heteroclinic orbits connecting unstable ISRs and stable ISRs near the boundaries of the Busse balloon (section 5.5.1);

4. The role of unstable ISRs far from the Busse balloon acting as a signpost between ISRs and SDC (section 5.5.2).

5.2 Problem formulation

5.2.1 Rayleigh-Benard convection (RBC)

We consider a buoyancy-driven flow of an incompressible fluid separated by a vertical height of d, confined between an upper wall of uniform temperature T_U, and a lower wall of uniform temperature T_L. The temperature of the lower wall is higher than the temperature of the upper wall ($\Delta T = T_L - T_U > 0$) such that the fluid is unstably stratified. The fluid has a density of ρ, a thermal diffusivity of κ, and a kinematic viscosity of ν. The non-dimensionalised governing equations with the Boussinesq approximation for buoyancy-driven flows are given by

$$\frac{\partial \mathbf{u}}{\partial t} + (\mathbf{u} \cdot \nabla)\mathbf{u} = -\nabla p + Pr\nabla^2\mathbf{u} + RaPr\theta\mathbf{j}, \tag{5.1a}$$

$$\frac{\partial \theta}{\partial t} + (\mathbf{u} \cdot \nabla)\theta = \nabla^2\theta, \tag{5.1b}$$

$$\nabla \cdot \mathbf{u} = 0, \tag{5.1c}$$

with the following boundary conditions at the wall,

$$\mathbf{u}|_{y=0,1} = 0, \quad \theta|_{y=0} = 1, \quad \theta|_{y=1} = 0, \tag{5.2a}$$

and the periodic boundary condition in the horizontal direction. Here, t denotes the time scaled by the vertical thermal diffusion time, d^2/κ, and $\mathbf{x}(= (x, y, z))$ is the spatial coordinates non-dimensionalised by d, where x and z are two orthogonal horizontal directions and y is the vertical direction. $\mathbf{u}(= (u, v, w))$ is the velocity vector scaled with κ/d, p the pressure scaled with $\rho\kappa^2/d^2$, $\theta(\equiv (T - T_U)/\Delta T)$ the non-dimensional temperature with T being the absolute temperature, and $\mathbf{j}$ denotes the unit vector in y-direction. The Rayleigh number and the Prandtl numbers are defined as in §5.1: $Ra = \alpha g d^3 \Delta T/\nu\kappa$, Prandtl number $Pr = \nu/\kappa$. Throughout this study, $Pr = 1$ is set.

5.2.2 Numerical method

The governing equations are solved numerically using Nektar++, an open-source spectral/hp-element method framework ?. An initial computational mesh, composed of quadrilateral elements, in the x-y plane is generated using Gmsh ? and then refined by Nekmesh, the mesh

generator available in Nektar++. Several computational domains of different sizes are prepared: $(L_x, L_y, L_z) = (32\pi, 1, 32\pi), (16\pi, 1, 16\pi), (8\pi, 1, 8\pi), (4\pi, 1, 4\pi)$. The spatial domain is discretised using a quasi-3D approach with spectral/hp elements in x-y domain and Fourier expansions in z-direction. The discretised equations are subsequently solved using a velocity-correction method based on a second-order implicit-explicit temporal scheme ???. Since different computational domain sizes were considered, the spatial distribution of spectral/hp elements in the x-y plane and Fourier expansions along z was kept constant. A spatial resolution of $(\Delta x, \Delta y|_{y=0,d}, \Delta y|_{y=d/2}, \Delta z) = (0.1\pi, 0.0549, 0.367, 0.25\pi)$ with polynomial order $P = 4$, and temporal resolution of $\Delta t = 0.0125$ was sufficient to establish numerical independence – for example, the Nusselt number, $Nu(= -\int_{x,z} \frac{\partial \theta}{\partial y}|_{y=0} \,\mathrm{d}x\mathrm{d}z)$, varies less than 10^{-5} when P was increased to $P = 5$.

5.2.3 Linear stability analysis of ISRs

As discussed in §5.1.3, we will perform a set of numerical experiments, in which a small perturbation about several unstable ISRs is added along their unstable manifolds. To obtain the direction of the unstable manifolds (i.e. linear instability eigenfunctions), we consider a small perturbation about the ISR (base) state:

$$\mathbf{u}(\mathbf{x}, t) = \mathbf{u}_{ISR,q}(\mathbf{x}) + \mathbf{u}'(\mathbf{x}, t), \tag{5.3a}$$

$$\theta(\mathbf{x}, t) = \theta_{ISR,q}(\mathbf{x}) + \theta'(\mathbf{x}, t), \tag{5.3b}$$

$$p(\mathbf{x}, t) = p_{ISR,q}(\mathbf{x}) + p'(\mathbf{x}, t), \tag{5.3c}$$

where $\mathbf{s} = [\mathbf{u}, \theta, p]^T$, $\mathbf{s}_{ISR,q} = [\mathbf{u}_{ISR,q}, \theta_{ISR,q}, p_{ISR,q}]^T$ and $\mathbf{s}' = [\mathbf{u}', \theta', p']^T$ refers to solution vector, the ISR (base) state of a given wavenumber, q, and the perturbation respectively. Substitution of (5.3) into (A.1) leads to the following linearised equations:

$$\frac{\partial \mathbf{s}'}{\partial t} = \mathcal{A}(\mathbf{s}_{ISR,q}; Ra, Pr)\mathbf{s}', \tag{5.4a}$$

where

$$\mathcal{A}(\mathbf{s}_{ISR,q}; Ra, Pr) = \begin{pmatrix} -(\mathbf{U} \cdot \nabla) - (\nabla \mathbf{U} \cdot) + Pr\nabla^2 & RaPr\hat{\mathbf{j}} & -\nabla \\ -(\nabla\Theta\cdot) & -(\mathbf{U} \cdot \nabla) + \nabla^2 & 0 \\ \nabla\cdot & 0 & 0 \end{pmatrix}. \tag{5.4b}$$

For the sake of simplicity here, we will only consider the ISRs invariant along z-direction. Since the ISRs are also assumed periodic in x-direction, the following form of normal-mode solution

can be considered:

$$\mathbf{s}'(\mathbf{x}, t) = \breve{\mathbf{s}}(x, y)e^{i(\alpha x + \beta z) + \lambda t} + \text{c.c.}, \tag{5.5}$$

where λ, α and β are the complex frequency, the streamwise wavenumber (or the Floquet exponent), and the spanwise wavenumber, respectively. Using the periodic nature of $\breve{\mathbf{s}}(x, y)$ in x-direction, (5.5) can also be written as

$$\mathbf{s}'(\mathbf{x}, t) = \left[\sum_{n=-\infty}^{\infty} \breve{\mathbf{s}}_n(y)e^{i\frac{2\pi}{L_x}(n+\epsilon)x} \right] e^{i\beta z + \lambda t} + \text{c.c.}, \tag{5.6}$$

where $\epsilon(= \alpha L_x/(2\pi))$ is the Floquet detuning parameter with $0 \leq \epsilon \leq 1/2$. Since the stability analysis here will be limited to the identification of unstable manifolds of ISRs in a fixed computational domain, $\epsilon = 0$ (fundamental mode) is considered only - note that the modes associated with $\epsilon \neq 0$ are only observed in the x domains greater than L_x.

Substituting (5.6) into (5.4) leads to a discretised eigenvalue problem in terms of the eigenvalue λ, where the wavenumber in the z-direction must be restricted to be $\beta = 2\pi m/L_z$, and m is a positive integer, for the given computational domain. The resulting eigenvalue problems are solved using a time-stepper-based iterative Arnoldi algorithm **?**, implemented in Nektar++, which has been verified in various applications **?**. The eigenvalues of primary instabilities of RBC computed in Nektar++ are also verified against those obtained with a Chebyshev-collocation method in Appendix A.5.

5.3 Transient SDC and elementary states in minimal domain

In this section, we seek to capture localised structures of SDC using a minimal domain by systematically reducing the domain by half in the homogeneous (x-z) directions. A random noise, characterised by Gaussian white noise (0 mean and 1 variance), generated with a total energy of

$$\delta = \frac{1}{\overline{V}} \int_\Omega \tilde{\mathbf{u}}(\mathbf{x})^T \tilde{\mathbf{u}}(\mathbf{x}) + RaPr\tilde{\theta}(\mathbf{x})^2 \, \mathrm{d}\Omega \approx O(10^{-3}), \tag{5.7}$$

where $\tilde{\mathbf{u}}(\mathbf{x})$ and $\tilde{\theta}(\mathbf{x})$ refer to the perturbation velocity and temperature about the base state $\mathbf{U}(\mathbf{x}) = \mathbf{0}$ and $\Theta(y) = 1 - y$, is introduced as an initial condition to the system. Here, we note that the first term of the integrand in (5.7) is the kinetic energy of the perturbation velocity and the second one measures the potential energy from the perturbation temperature.

The system is time integrated for 300 units of vertical thermal diffusion time $t \, (= d^2/\kappa)$. The resulting mid-plane temperature snapshots $\theta(x, z)|_{y=d/2}$ at $t = 300$ exhibit features of spiral defect chaos, as shown in figure 5.1. When the domain size is large, for instance, $\Gamma = 8\pi$ shown in figure 5.1(a), features of SDC consist of many repeating localised spirals, defects and dislocations. Reducing the domain in half to $\Gamma = 4\pi$, shown in figure 5.1(b), led to a spatially less extensive chaotic state, revealing a single spiral, with some defects and dislocations.

Figure 5.1: Midplane temperature snapshots, $\theta(x,z)|_{y=d/2}$, of spiral defect chaos (SDC) for a domain aspect ratio of (a) $\Gamma = 8\pi$ and (b) 4π. Elementary states of SDC captured when $\Gamma = 2\pi$: (c) steady *pacman* (PM), (d) relative periodic orbit *spiral-defect* (SD), (e) relative periodic orbit *hooked* (HK), and (f) periodic *peanut* (PN) elementary state. Note that the localised structures indicated by bounding boxes in (a,b) resemble structures in (c-f).
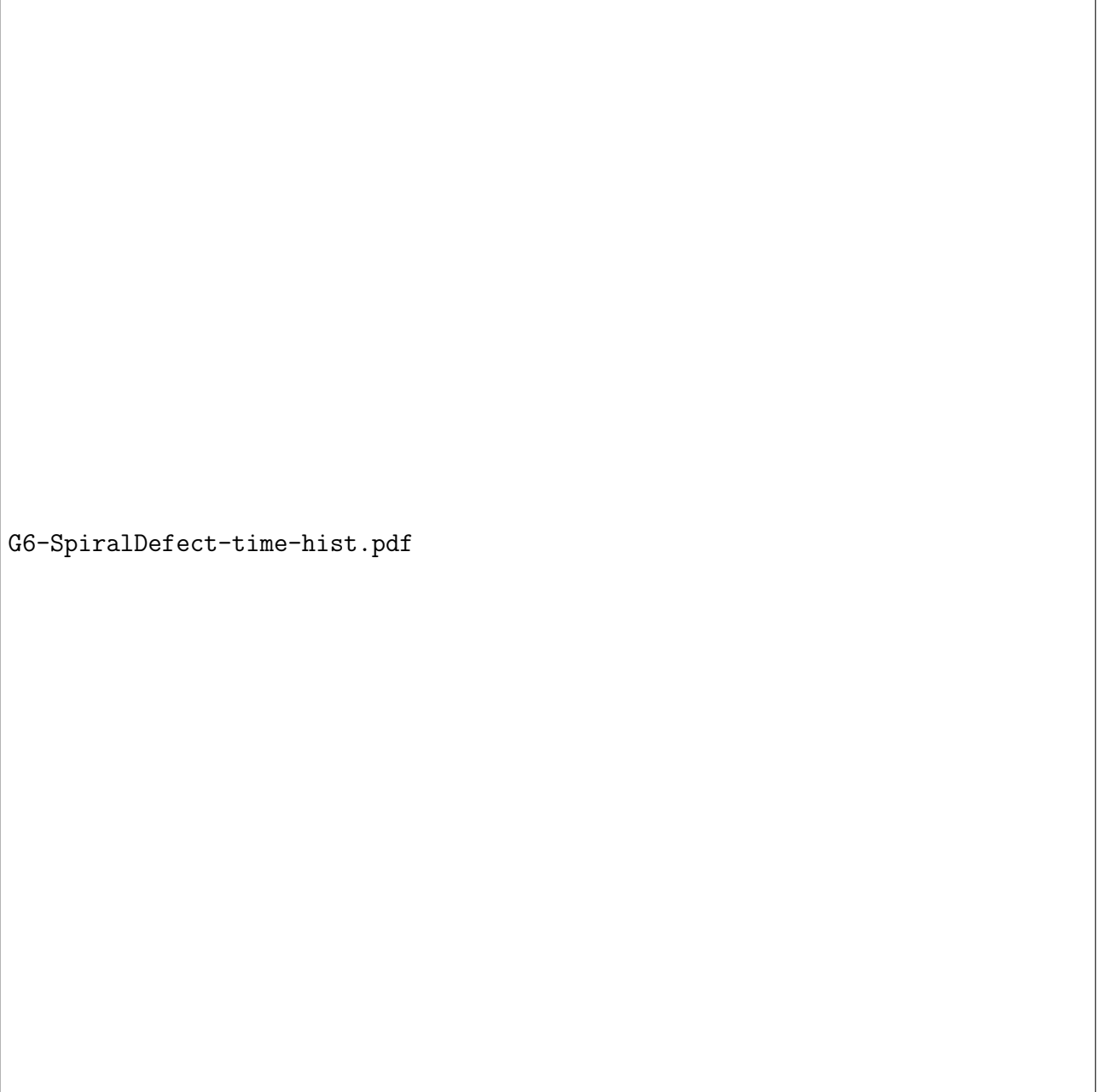
Surprisingly, a further reduction of the domain in half, $\Gamma = 2\pi$, does not lead to sustained SDC, but rather, a transient SDC state before settling into stable 'elementary' states. These elementary states are identified as *pacman* (PM), *spiral-defect* (SD), *hooked* (HK), and *peanut* (PN) states in figure 5.1 (c-f), which resemble the localised features of SDC (see the coloured bounding boxes in figures 5.1(a,b)). These states represent stable invariant solutions of (A.1). Specifically, PM state represents a steady equilibrium, SD and HK states are characterised by relative periodic orbits, and the PN state is a periodic orbit **?**.

An example of a transient SDC state is shown in figure 5.2(a), where spirals, a typical feature of SDC **?**, form spontaneously with a chaotic transient (figures 5.2(c-e)), before stabilising into SD state with a period of $T \approx 73$ (figures 5.2(f,g)). In addition to the elementary states presented in figures 5.1(c-f), we have identified ten additional elementary states, each independently preceded by a transient SDC state, and fourteen stable ISRs of varying wavenumbers (see Appendix A.6). In total, we have identified 28 states with $\Gamma = 2\pi$. Minimising the domain further to $\Gamma = \pi$ only led to stable ISRs at least for the random initial conditions we have examined in this study. We therefore consider $\Gamma = 2\pi$ as the minimal domain, in which both transient SDC and elementary states exist. It is worth mentioning that solutions to multiple states were obtained in smaller domains with $\Gamma = 2$, but in a cylindrical domain **??**.

To show whether SDC and elementary states are related, we compare their state space trajectories, and the averaged wall-normal temperature profiles. Figure 5.3 presents the two chaotic trajectories of SDC from $\Gamma = 8\pi, 4\pi$, four of fourteen transient SDC trajectories obtained and fourteen stable fixed-points of ISRs from $\Gamma = 2\pi$ on a two-dimensional state portrait based on the volume $(\overline{V} = L_x L_y L_z)$ normalised L2-norms of velocity $(||\frac{1}{\overline{V}}\tilde{\mathbf{u}}||_2)$ and temperature $(||\frac{1}{\overline{V}}RaPr\tilde{\theta}||_2)$ perturbations. The trajectories begin from $t = 3$, as those for $t < 3$ contain artificial transients and are omitted for clarity. The state space trajectories of SDC ($\Gamma = 8\pi, 4\pi$) and the transient SDC states for $\Gamma = 2\pi$ are visibly attracted toward a region, where $||\frac{1}{\overline{V}}\tilde{\mathbf{u}}||_2 \approx 6.3$ and $||\frac{1}{\overline{V}}RaPr\tilde{\theta}||_2 \approx 8.6$, as shown in figure 5.3(b). This suggests that they are presumably the same type of SDC emerging in different domains. The closely packed chaotic trajectories are in contrast to the ISRs populating sparsely.

The transient SDC trajectories eventually stabilise into fourteen elementary states in figure 5.4, where the transient SDC trajectories from figure 5.3 are now omitted. Obscured by the transient SDC trajectories initially, the elementary states in figure 5.4(b) emerge as seven steady states (■), two travelling waves (×), one periodic orbit (dash-dotted line) and four relative periodic orbits (solid line). All the SDC trajectories for $\Gamma = 8\pi, 4\pi, 2\pi$ are organised around the fourteen elementary states (figure 5.4(b)). Notably, the state space trajectories of SDC and the elementary states are in close vicinity to the ISR of wavenumbers $q = 2.5/d$ (see figures 5.3 and 5.4), which corroborates with the averaged wavenumber of SDC, $q_{avg} \approx 2.5/d$ **??**.

The comparison between the time-averaged mean temperature profile, mean-squared temperature fluctuations, and mean-squared velocity fluctuations of SDC (figures 5.1(a,b)) and elementary states (figures 5.1(c-f) and figure A.6) are presented in figure 5.5. In figure 5.5(c),

Figure 5.2: (a,b) Time history of the volume ($\overline{V} = L_x L_y L_z$) normalised L2-norm of velocity perturbations from a random initial condition with $\delta = 0.001$ and (c-g) Mid-plane temperature snapshots at $t = 6, 15, 30, 79, 250$. Here, transient chaotic SDC lasts up to $t \approx 70$, before stabilising into an SD state, emerging as a relative periodic orbit with the time period $T \approx 73$ propagating diagonally in the negative x- and z-directions.

Figure 5.3: (a) State-space portrait in the plane of $||\frac{1}{\overline{V}}\tilde{\mathbf{u}}||_2$ and $||\frac{1}{\overline{V}}RaPr\tilde{\theta}||_2$ for SDC from $\Gamma = 8\pi, 4\pi$ (figures 5.1(a,b)), four transient SDC state proceeding to stable elementary states (figures 5.1(c-f)), A.6), and fourteen stable stationary ISRs of wavenumbers $2.0 \leq qd \leq 3.35$. Here, the magnitude of q is denoted by the opacity of the filled symbol ($\bullet$), increasing from the bottom left and turning toward the top left shown as arrows; (b) Zoomed-in view of (a). The legend refers to the figures for respective trajectories preceding snapshots in figure 5.1.

Figure 5.4: (a) State-space portrait (from figure 3) highlighting the transient SDC states for $\Gamma = 2\pi$ proceeding toward stable elementary states (see figures 5.1(c-f), A.6): steady states (■), travelling waves (×), periodic orbit (dash-dotted line) and relative periodic orbits (solid lines). Here, ISRs are denoted by the varying opacity of the filled symbol (•) increasing from the bottom left and turning toward the top left shown as arrows; (b) Zoomed-in view of (a).

Figure 5.5: Profiles of (a) averaged temperature, (b) root-mean-squared temperature fluctuation, (c) sum of root-mean-squared x-z velocity fluctuations and (d) root-mean-squared wall-normal velocity fluctuations for the SDC and elementary states shown in figures 5.1(a-f) and in Appendix A.6. Note that $\langle \cdot \rangle = \frac{1}{TL_x L_z} \int_{t,x,z} \cdot \, \mathrm{d}t\mathrm{d}x\mathrm{d}z$ refers to the time and plane averaged operator, where T was chosen to be sufficiently long to ensure temporal convergence.

we present the sum of mean-squared x- and z- velocity fluctuations due to horizontal isotropy. The mean temperature profiles of the elementary states closely match those of SDC (figure 5.5(a)). Notably, the mean-squared temperature and velocity fluctuations between SDC states (grey and black dashed curves) of figures 5.5(b-d) are similar. The mean-squared temperature and velocity fluctuations profiles of elementary states are comparable to those of SDC but are in general, slightly larger in magnitudes.

The spatial-temporal complexity of SDC reduces when the domain size is reduced from $\Gamma = 8\pi$ to $\Gamma = 4\pi$, i.e. less disordered spatial features. Reducing the domain from $\Gamma = 4\pi$ to $\Gamma = 2\pi$ led to transient SDC before stabilising into many elementary states. From the conventional view, especially made in the context of shear flow turbulence, this is unexpected as the chaotic state (i.e. turbulence) is commonly described as solution trajectories wandering around unstable invariant solutions **????**. However, in this particular case observed in RBC, the chaotic state (i.e. SDC) is instead stabilised into stable invariant solutions (elementary states). Despite this distinguished feature of the state space, each of the elementary states is still seen to emerge in a spatially localised manner of SDC in an extended domain (figure 5.1), and their spatially-averaged statistics are remarkably similar to those of SDC in extended domains (figure 5.5). Therefore, we consider the elementary states in the minimal domain to be the 'building blocks' structure of SDC.

5.4   Multiplicity of edge states

The stable nature of many ISRs and elementary states underpinning SDC implies the existence of state-space boundaries between them (i.e. edge). In this section, we perform the edge tracking between the stable manifolds of ISRs and elementary states to compute the attractors on the edge (i.e edge states). For the edge tracking, we use the bisection method **???**, with an initial condition given by

$$\mathbf{s_0}(\mathbf{x}, t = 0) = \chi \mathbf{s}_{ISR,q} + (1 - \chi)\mathbf{s}_{elementary}, \tag{5.8}$$

where $\mathbf{s_0}(= [\mathbf{u}_0, \theta_0, p_0]^T)$ refers to an initial condition consisting of a weighted sum, $\chi \in [0, 1]$, between a stable ISR state, $\mathbf{s}_{ISR,q}$ of a wavenumber q, and an elementary state, $\mathbf{s}_{elementary}$ where the subscript refers to its names in figures 5.1(c-f).

Given the large number of stable ISRs and elementary states, we shall focus on the computation of the edge states considering three of the stable ISRs and two of the elementary states. However, in principle, the edge tracking is technically possible with other stable ISRs and elementary states. As such, in general, multiple edge states are expected. The three ISRs are related to three different wavenumbers, denoted by $\mathbf{s}_{ISR,q=2.06/d}, \mathbf{s}_{ISR,q=2.24/d}, \mathbf{s}_{ISR,q=3.16/d}$ (figures A.7(b,d,j)) respectively, and the two elementary states are SD state, $\mathbf{s}_{spiral-defect}$ (figure 5.1(c)), and PM state, $\mathbf{s}_{pacman}$ (figure 5.1(d)). Using this set of stable ISRs and elementary states, we aim to track the edge near $\mathbf{s}_{ISR,q}$ in the direction of $\mathbf{s}_{elementary}$ by bisecting the initial condition with χ in (5.8), whereby one of the two trajectories across the edge decays toward

$\mathbf{s}_{ISR,q}$	$\mathbf{s}_{elementary}$	Edge state	State transitioned
$\mathbf{s}_{ISR,q=2.06/d}$	$\mathbf{s}_{spiral-defect}$	*Jagged* (Stationary)	Transient Chaos
$\mathbf{s}_{ISR,q=2.06/d}$	$\mathbf{s}_{pacman}$	*Jagged* (Stationary)	Transient Chaos
$\mathbf{s}_{ISR,q=2.24/d}$	$\mathbf{s}_{spiral-defect}$	*Point-defect* (Travelling wave)	$\mathbf{s}_{bubble-defect}$
$\mathbf{s}_{ISR,q=2.24/d}$	$\mathbf{s}_{pacman}$	*Forked* (Relative Periodic Orbit)	Transient Chaos
$\mathbf{s}_{ISR,q=3.16/d}$	$\mathbf{s}_{spiral-defect}$	*Skewed-varicose* (Stationary)	Transient Chaos
$\mathbf{s}_{ISR,q=3.16/d}$	$\mathbf{s}_{pacman}$	*Skewed-varicose* (Stationary)	Transient Chaos

Table 5.1: A summary of the edge states computed. The first two columns denote the pair of initial conditions considered for edge tracking in Eq. (5.8). The names and classification of the edge states are described in the third column. The last column describes the state transitioned from $\mathbf{s}_{ISR,q}$ for sufficiently large χ in Eq. (5.8).

$\mathbf{s}_{ISR,q}$ and the other is attracted toward transient chaotic state (i.e. SDC), referred to as the 'lower' and 'upper' trajectories respectively. The bisection of the initial condition is carried out by monitoring the difference in two trajectories with Nu (i.e. ΔNu). When the two trajectories reach a certain time at which $\Delta Nu > 0.0007$, the bisection of the initial condition is repeated using the flow fields from the two different trajectories by replacing $\mathbf{s}_{ISR,q}$ and $\mathbf{s}_{elementary}$ in (5.8) with them. This process is repeated until the edge trajectory reaches an attractor (i.e. an edge state).

Table 5.1 summarises the edge states and their dynamical properties computed from six combinations of $\mathbf{s}_{ISR,q}$ and $\mathbf{s}_{elementary}$ states, and they are visualised with the mid-plane temperature field in figure 5.6. The convection patterns of edge states are often featured with mild spatial complexity compared to SDC and the elementary states. In particular, their patterns contain the underlying convection pattern of $\mathbf{s}_{ISR,q}$ with spatially localised defects. We obtained four edge states: specifically, the *jagged* and *skewed-varicose* edge states are stationary, and the *point-defect* and *forked* edge states are travelling wave and a relative periodic orbit respectively. The *jagged*, *skewed-varicose* and *forked* edge states lie on the boundary, separating the basins of attraction of stable $\mathbf{s}_{ISR,q}$ from transient SDC. In the case of the *point-defect* edge state, the solution trajectory is found to bypass the transient SDC state, directly settling into a stable elementary state characterised by bubble-like convection roll defects, $\mathbf{s}_{bubble-defect}$. Since the *jagged*, *skewed-varicose*, *forked* edge states are similar in nature, acting as separatrices between $\mathbf{s}_{ISR,q}$ states and transient SDC, we will focus our analysis on the *jagged* edge state only, alongside the *point-defect* edge state.

Using Nu as an observable, successive bisections between $\mathbf{s}_{ISR,q=2.06/d}$ and $\mathbf{s}_{spiral-defect}$ reveal the trajectory along the edge, as illustrated in figure 5.7. The trajectory along the edge spans from $t \approx 0-15$, and is initially characterised by a 'speckled' defect (figure 5.7(b)). The 'speckled' defect grows into a spatially localised jagged-liked defect as the trajectory is attracted to the *jagged* stationary edge state from $t \approx 6.5$ onwards (figures 5.7(c-e)). We further examine the two trajectories in the opposite directions along the unstable manifold of the *jagged* edge state

Figure 5.6: Mid-plane termperature fields of ISRs and elementary states used in Eq. (5.8), and the resulting edge states. Here, ISRs (green borders): (a) $\mathbf{s}_{ISR,q=2.06/d}$, (b) $\mathbf{s}_{ISR,q=2.24/d}$, (c) $\mathbf{s}_{ISR,q=3.16/d}$; elementary states: (d) $\mathbf{s}_{pacman}$, (e) $\mathbf{s}_{spiral-defect}$; edge states (black borders): (f) *jagged*, (g) *point-defect*, (h) *forked* and (i) *skewed-varicose* edge state.

Figure 5.7: (a) Time history of Nu and (b-e) the corresponding mid-plane temperature field snapshots at $t = 2.0, 6.5, 31.0, 65.5$ along the edge trajectory obtained by bisecting $\mathbf{s}_{ISR,q=2.06/d}$ and $\mathbf{s}_{spiral-defect}$.

in figure 5.8, where the 'upper' trajectory evolves into a transient SDC and the 'lower' trajectory decays into the original stable $\mathbf{s}_{ISR,q=2.06/d}$ state. Starting from the 'upper' trajectory (figure 5.8(a)), the spatially localised jagged defect grew in the direction normal to the roll orientation at $t = 80.5$ (figure 5.8(b)), contaminating the adjacent roll structure and propagating through the domain where transient SDC emerges from $t > 80.5$, lasting up to $t \approx 120$ (a snapshot of transient chaotic SDC regime at $t = 90.5$ is shown in figure 5.8(c)). The trajectory subsequently stabilises into a travelling-wave PM elementary state described by 'pac-man' like patterns, propagating along the $-x$ direction from $t = 125.5$ to $t = 170.5$ (figures 5.8(d,e)). This is reminiscent of a secondary cross-roll instabilities experienced by low-wavenumber ISRs (such as $\mathbf{s}_{ISR,q=2.06/d}$ considered here), where a defect propagates in the direction perpendicular to the rolls ?. Along the 'lower' trajectory (figure 5.8(f)), the jagged defects diffuses from $t = 70.5$ to $t = 75.5$, decaying into the stable $\mathbf{s}_{ISR,q=2.06/d}$ state at $t = 80.5$ (figures 5.8(g-j)).

Next, we analyse the edge trajectory obtained bisecting between $\mathbf{s}_{spiral-defect}$ and $\mathbf{s}_{ISR,q=2.24}$ in figure 5.9. The trajectory along the edge from $t = 4$ (figure 5.9(b)) is described by time-dependent convection structures. The edge trajectory began to be stabilised into the *point-defect* edge state from $t = 13$ onwards (figure 5.9(c)), propagating along x direction from $t = 22.5$ (figures 5.9(d,e)). It is characterised by the convection structure of the $\mathbf{s}_{ISR,q=2.24}$ state with a pointed defect structure, hence referred to as the *point-defect* edge state. The upper and lower trajectories through two opposite directions of the unstable manifold of the travelling wave *point-defect* edge state are subsequently examined in figure 5.10. Integrating along the upper trajectory (figure 5.10(a)), the spatially localised point-defect structure grew from $t = 43$ to $t = 83$ (figures 5.10(b-d)), saturating into a stationary elementary state at $t = 163$ (figure 5.10(e)) characterised by $\mathbf{s}_{ISR,q=2.24}$ with a large bubble defect. Along the lower trajectory (figure 5.10(f)), the spatially localised point defect merged onto the adjacent convection roll from $t = 38$ to $t = 44.5$ (figures 5.10(g,h,i)), stabilising into the $\mathbf{s}_{ISR,q=2.24/d}$ state at $t = 53$ (figure 5.10(j)). It is worth noting that, in this particular case, no chaotic transient in the form of SDC has been observed.

Finally, figure 5.11 depicts a state space portrait of stable ISRs, SDC and the edge/elementary states found here. As seen previously, SDC and elementary states are seen to be clustered around the region of $||\frac{1}{V}\tilde{\mathbf{u}}||_2 \approx 6.3$ and $||\frac{1}{V}RaPr\tilde{\theta}||_2 \approx 8.6$, whereas stable ISRs are distributed along a horseshoe-shaped band (green line). The edge states found in this study are located not far from the (green) horseshoe-shaped band of ISRs, as they presumably lie in a smaller (grey) horseshoe-shape band situated between ISRs and SDC or elementary states. While we have identified four edge states, we expect that there are more edge states, presumably distrubuted along the (grey) horseshoe-shaped band. It is also worth mentioning that the edge states we found here contain the underlying ISR structure ($\mathbf{s}_{q=2.06/d,2.24/d,3.16/d}$) modified by spatially localised defects and 'pinches' between rolls, supporting its proximity with ISRs in the state space. This feature is also reminiscent of spatially localised edge states identified in boundary layer flows ?. Lastly, we would like to emphasise that we have only considered initial conditions from the states between $\mathbf{s}_{ISR,q}$ and $\mathbf{s}_{elementary}$ and not strictly between $\mathbf{s}_{ISR,q}$ and a
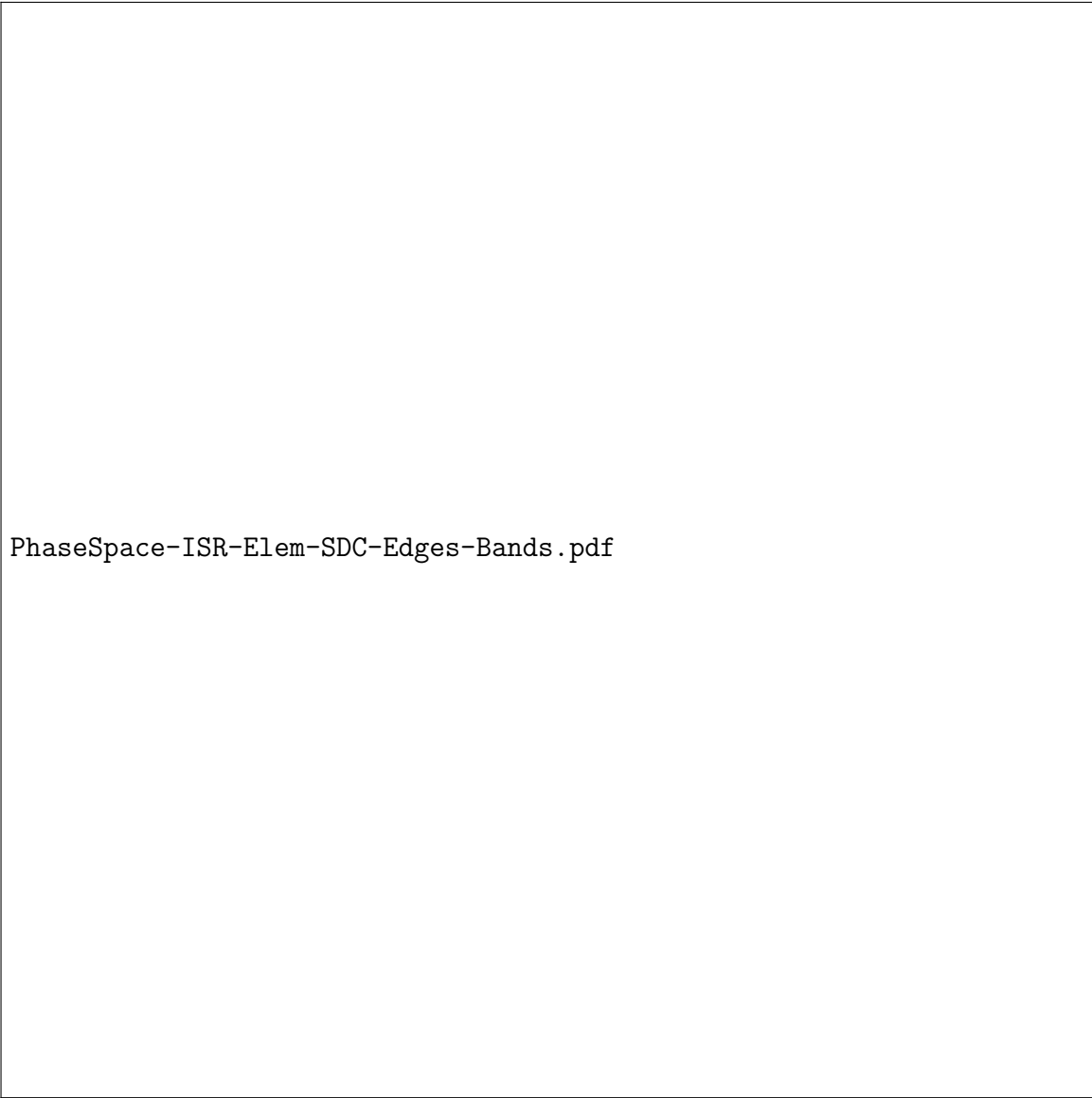
Figure 5.8: Time history of Nu along two opposite directions along the unstable manifold of the *jagged* edge state: (a) 'upper' trajectory leading to a transient SDC for $t \approx 85 - 120$ and subsequently to PM state for $t > 120$ and (f) 'lower' trajectory stabilising into $\mathbf{s}_{ISR,q=2.06/d}$. Mid-plane temperature fields are visualised in (b-e) along the upper trajectory at $t = 80.5,\ 90.5,\ 125.5,\ 170.5$, and in (g-j) along the lower trajectory at $t = 70.5, 75.5, 80.5, 85.5$.

Figure 5.9: a) Time history of Nu and (b-e) the corresponding mid-plane temperature field snapshots at $t = 4, 13, 22.5, 40.5$ along the edge trajectory obtained by bisecting $\mathbf{s}_{ISR,q=2.24}$ and $\mathbf{s}_{spiral-defect}$.

Figure 5.10: Time history of Nu along two opposite directions of the unstable manifold of the *point-defect* edge state: (a) 'upper' trajectory leading a stationary elementary state with bubble defect from $t \approx 43 - 163$ and (f) 'lower' trajectory decaying to the stable $\mathbf{s}_{ISR,q=2.24}$ state. Mid-plane temperature fields are visualised in (b-e) along the upper trajectory at $t = 43.0, 58.0, 83.0, 163.0$, and in (g-j) along the lower trajectory at $t = 38.0, 43.5, 44.5, 53.0$.

PhaseSpace-ISR-Elem-SDC-Edges-Bands.pdf

Figure 5.11: Phase portrait of the *jagged*, *point-defect*, *defect* and *skewed-varicose* edge states, along with stable ISRs, elementary states and transient SDC. Green and grey horseshoe lines are the regions, where stable ISRs and edge attractors are expected to be distributed when different sizes of the computational domain are considered.

Cases	$\beta = 0.25$	$\beta = 0.50$	$\beta = 0.75$	$\beta = 1.00$	$\beta = 1.25$	$\beta = 1.50$	$\beta = 1.75$
$q = 3.5/d$	$ISR_{3.04}$	(a) $ISR_{2.50}$	Stable	Stable	Stable	Stable	Stable
$q = 4.0/d$	$ISR_{2.50}$	(b) $ISR_{3.16}$	$ISR_{3.00}$	$ISR_{2.83}$	Stable	Stable	Stable
$q = 4.5/d$	$ISR_{2.50}$	$ISR_{2.50}$	(c) $ISR_{3.00}$	$ISR_{3.20}$	(d) Elementary	$ISR_{2.50}$	(e) Elementary

Table 5.2: Asymptotic state of secondary linear instabilities of $q = 3.5/d, 4.0/d, 4.5/d$. Subscripts in ISR refer to asymptotic wavenumber q, e.g., $ISR_{2.5}$ refers to ideal straight rolls with wavenumber of $q = 2.5/d$. The asymptotic behaviours of (a-c) and (d,e) are discussed further in §5.5.1 and §5.5.2 respectively.

transient SDC state. Nevertheless, three of the edge states are found to lie on the boundary separating the stable ISRs from transient SDC, supporting previous findings that the transient chaotic SDC are related to elementary states.

5.5 Unstable ideal straight rolls

Thus far, we have studied the edge and the edge states between some of the stable ISRs and elementary states. The dynamics associated with the unstable ISRs outside of the Busse balloon, however, remain unclear **?**. Given that the stable ISRs and SDC form a bistable system, it is expected that some of the unstable ISRs near the Busse balloon would asymptotically reach one of the stable ISRs as the difference between the stable and unstable ISRs would be sufficiently small **??**. On the other hand, the unstable ISRs, which exist far from the boundary of the Busse balloon, may well have a sufficiently large deviation from the stable ISRs, implying that they are possibly associated with a state-space route to the SDC. The purpose of this section is to test this hypothesis by examining the long-term behaviour of the linear instabilities of the unstable ISRs.

We consider the linear instabilities of 3 unstable ISRs on the right side of the Busse balloon, with increasing wavenumber of $q = 3.5/d, 4.0/d, 4.5/d$, as shown in figure 5.12(a). The identification of the linear instability mode (or unstable manifold) with the different spanwise wavenumbers β is considered (see (5.6)). Figure 5.12(b) presents the unstable eigenvalues as a function of β. There are 2, 4 and 7 unstable manifolds ($\Re(\lambda) > 0$) for unstable ISRs of $q = 3.5/d, 4.0/d, 4.5/d$ respectively, forming total 13 unstable manifolds. In general, the growth rate and the number of linear instability modes (i.e. the repelling strength and the number of unstable manifolds) increase as q increases. It is worth mentioning that the solutions of unstable ISRs of $\mathbf{s}_{ISR,q}(x, y)$ (required for linear stability analysis) are obtained by restricting the computational domain to the 2D x-y plane which artificially suppresses 3D linear instabilities. We also note that the stability analysis of the unstable ISR, $q = 5.0/d$ was not considered as it quickly evolved into an unstable ISR of $q = 3.5/d$, which will be discussed in section §5.5.1.

To consider the long-term behavior in the direction of the unstable manifolds, an initial condition,

$$\mathbf{s}_0(\mathbf{x}, t = 0) = \mathbf{s}_{ISR,q}(\mathbf{x}) + \hat{\mathbf{s}}_\beta(x, y)e^{i\beta z}, \tag{5.9}$$
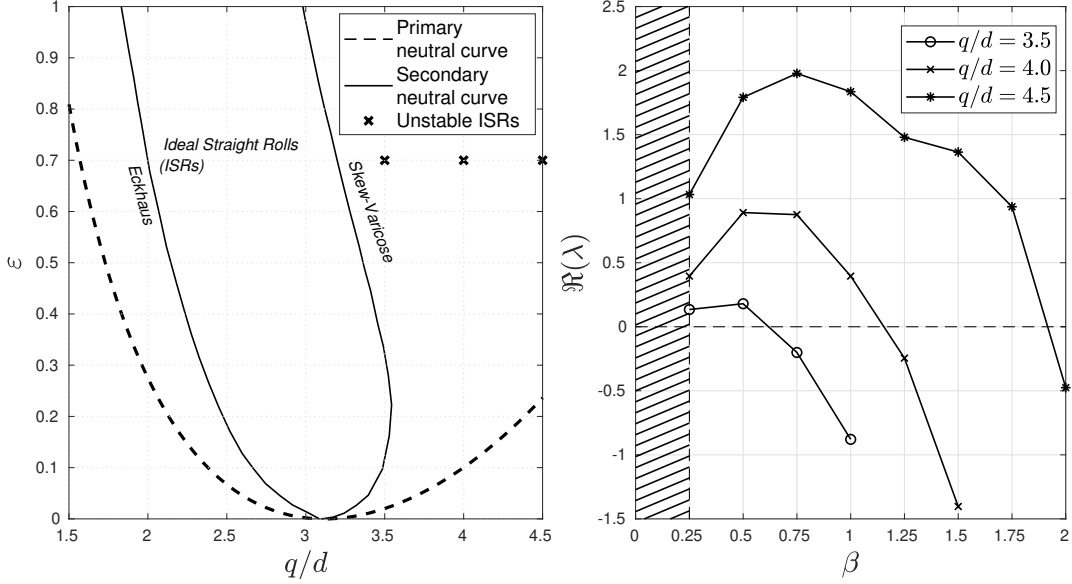
Figure 5.12: (a) Primary and secondary (Busse balloon from figure 1 **?**) stability curves and unstable ISRs with $q = 3.5/d, 4.0/d, 4.5/d$; (b) Variation of the growth rate of instabilities of unstable ISRs as a function of spanwise wavenumber β. (Note that there are a total 13 unstable eigenmodes.)

is prescribed to equation (A.1). Here, $\hat{\mathbf{s}}_\beta e^{i\beta z}$ is the unstable eigenmode, the amplitude of which was scaled such that its total energy (defined in (5.6)) of $\delta = 10^{-5}, 10^{-4}, 10^{-3}$ were considered. The total energy of the eigenmode, $\delta = 10^{-4}$ was found to be sufficiently small enough to ensure linear growth, while large enough to prevent other eigenmodes from being excited. Next, the initial condition is time integrated over an extended period until an asymptotic state is reached. Table 5.2 shows the asymptotic states of 13 linear instabilities, depicted in figure 5.12(b), of which 11 linear instabilities led to ISRs states, forming a network of heteroclinic orbits which will be discussed in §5.5.1. Only the remaining 2 instabilities led to a transient SDC state before settling into an elementary state discussed further in §5.5.2.

5.5.1 Pathways leading to ISRs - heteroclinic orbits

In this section, the asymptotic behaviour of the most unstable linear instabilities of ISRs (tab 5.2(a-c)) will be discussed. Figure 5.13 depicts the state space plot of volume normalised L2-norms of velocity and temperature. It reveals a number of heteroclinic orbits, connecting the base state (●), stable (●) and unstable (●) ISRs. Figure 5.13(a) exhibits several solution trajectories linking the base state, stable and unstable ISRs: three orbits connecting the base state to all the stable and unstable ISRs shown, one from the ISR of $q = 3.5/d$ to that of $q = 2.5/d$, and one from the ISR of $q = 5.0/d$ to that of $q = 3.5/d$. Here, caution will need to be taken in interpreting each of the connections as a heteroclinic orbit, because there appears to be an invariant state at which the speed of the solution trajectory nearly vanishes (a sign of the existence of unstable invariant states or ghost states **?**): for example, see the solution

Figure 5.13: The phase-space solution trajectories connecting: (a) unstable base (conductive) state between 10 unstable rolls ($q = 5/d$), 7 unstable rolls ($q = 3.5/d$) and 5 stable rolls ($q = 2.5/d$); (b) unstable base (conductive) state between 8 unstable rolls ($q = 5/d$) and 6 stable rolls ($q = 3.16/d$); (c) unstable base (conductive) state between 9 unstable rolls ($q = 4.5/d$) and 6 stable rolls ($q = 3/d$). Here, the size of the arrows indicates the speed of the solution trajectory (or flow).

trajectory between the ISR of $q = 3.5/d$ to that of $q = 2.5/d$ (in the inset of figure 5.13(a)), which will be discussed below with figure 5.14. Starting from the primary base state, the system saturates into an ISR of wavenumber $q = 5.0/d$. Since this ISR is linearly unstable, it evolves into another unstable ISR of $q = 3.5/d$, before ultimately stabilising into an ISR of $q = 2.5/d$. Next, figure 5.13(b) shows three solution trajectories connecting the base state, an unstable and stable ISR. Starting from the base state, the system transitions into an unstable ISR of $q = 4/d$ before stabilising into an ISR of $q = 3.16/d$. Lastly, figure 5.13(c) presents three solution trajectories connecting the base state, a stable and unstable ISR. Starting from the base state, it can evolve to an unstable ISR of $q = 4.5/d$ before settling into a stable ISR of $q = 3.0/d$. Figure 5.13 suggests that each of the stable ISRs within the Busse balloon has the basin of attraction, characterised by a web of heteroclinic orbits connecting some of the unstable ISRs outside of the Busse balloon. It is worth emphasising that the connections between the solutions presented here were obtained by time-integrating the dominant unstable manifolds of ISRs. In practice, there are many more unstable manifolds (see table 5.2) which have not been presented, potentially leading to more complex networks of heteroclinic orbits that form the basin of attraction for each stable ISR.
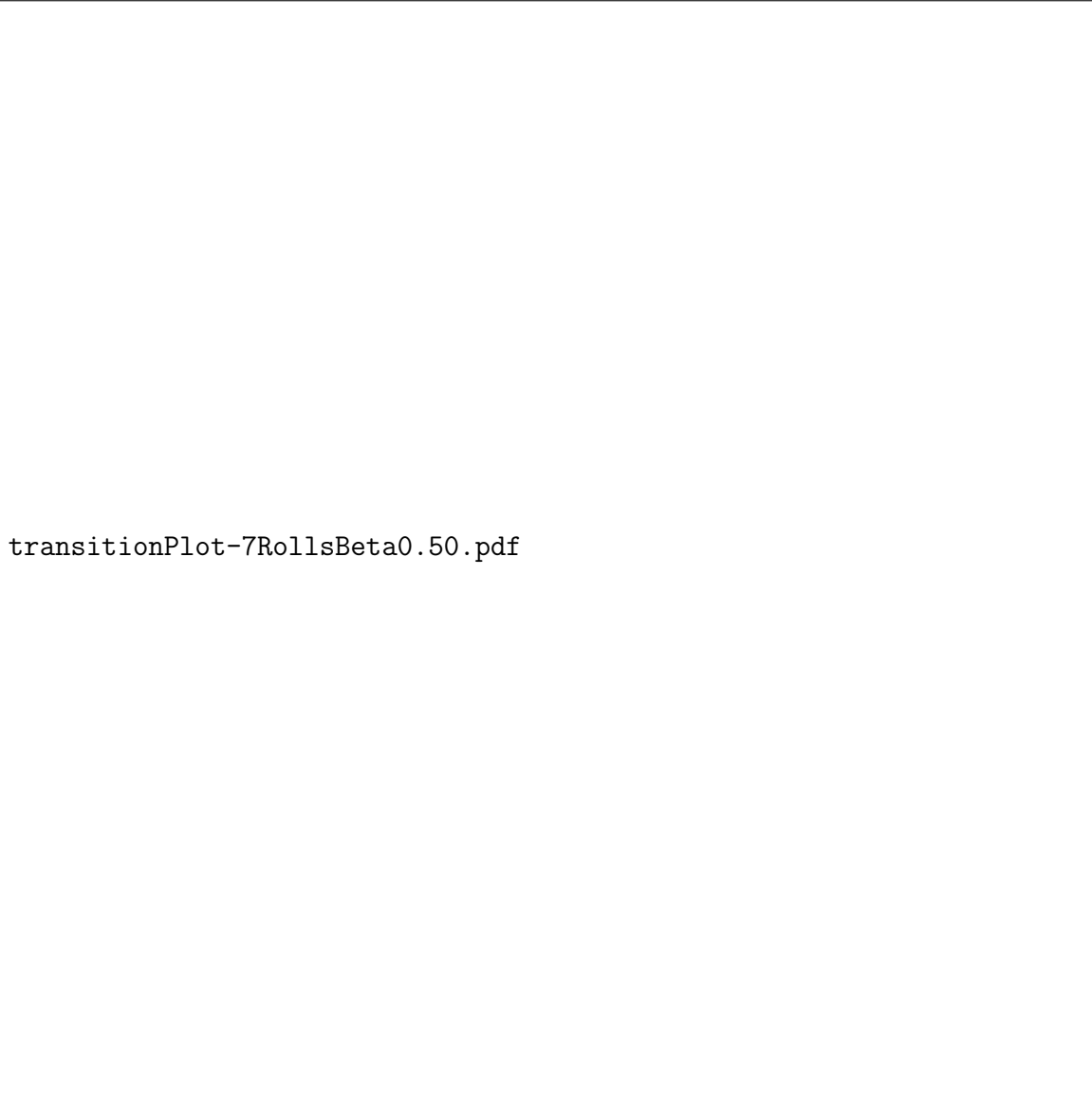
Figure 5.14 describes the asymptotic behaviour with the most unstable eigenmode for $q = 3.5/d$ (table 5.2(a)) in detail, corresponding to the connection between the unstable ISR of $q = 3.5/d$ and the stable ISR of $q = 2.5/d$ in figure 5.13(a). To observe the linear instability defined in Eq. (5.9), we report contribution of modal energy (figure 5.14(a)) as

$$E_k(t) = \frac{1}{2} \int_\Omega |\hat{\mathbf{u}}_k(t)|^2 \, \mathrm{d}\Omega, \tag{5.10}$$

where $\hat{\mathbf{u}}_k$ refers to the k-th Fourier coefficient in z-direction. Initially, the simulation starts from the ISR state of 7 rolls ($t = 33$), corresponding to a roll-wavenumber of $q = 3.5/d$. The unstable eigenmode $\hat{\mathbf{s}}_{\beta=0.50}$ grows exponentially before peaking at $t = 48.50$, forming an 'S'-liked symmetric state (figure 5.14(c)). Note that, at this point, the time derivative of $E_k(t)$ nearly vanishes, indicating that the snapshot taken at $t = 48.50$ is potentially close to an unstable invariant state. Finally, the modal energy of $N_z = 2$ decays and the system settles into an ISR state of $q = 2.5/d$ (5 rolls aligned in the x-direction), which is within the Busse balloon.
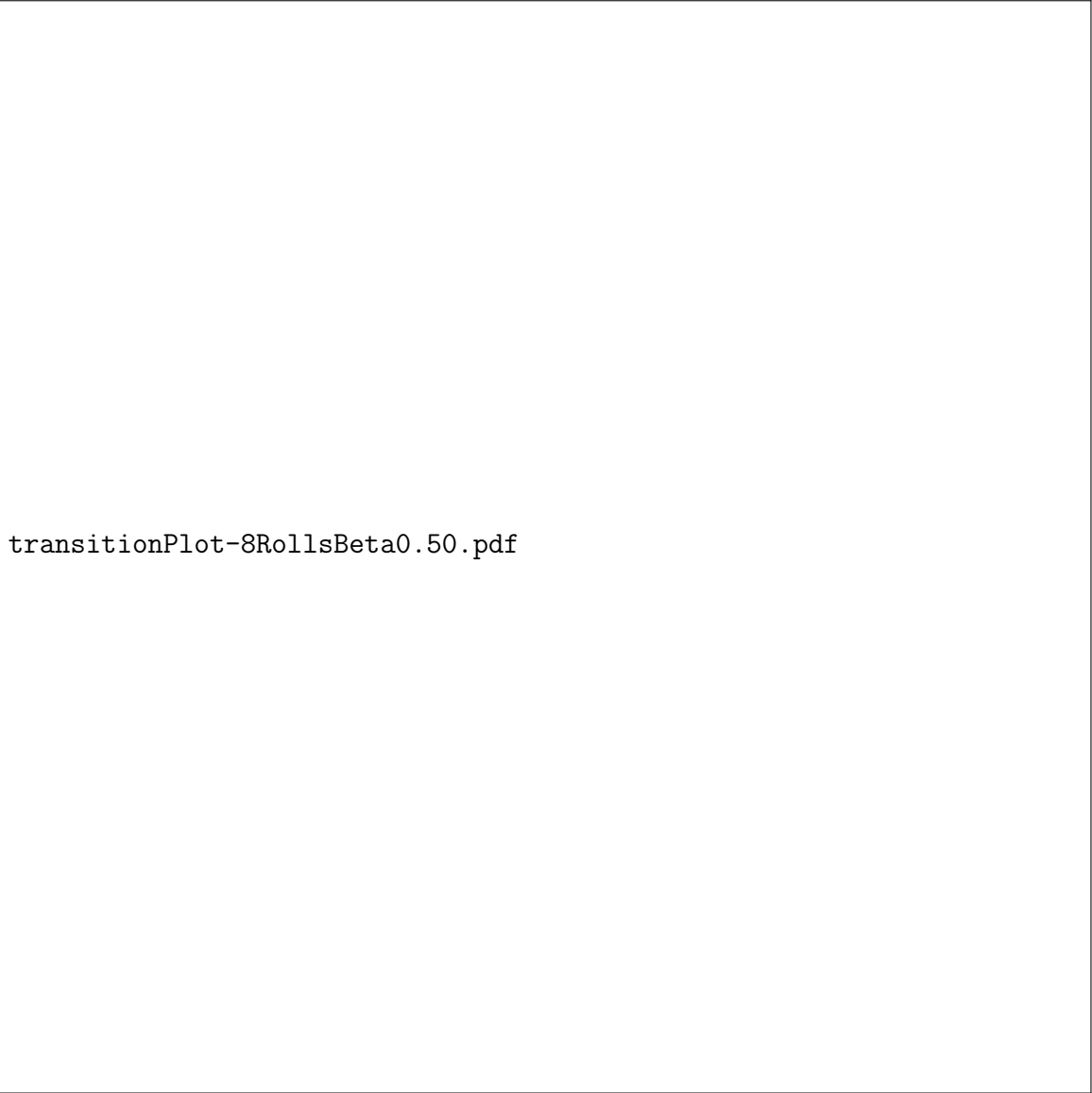
Figure 5.15 illustrates the asymptotic behaviour with the most unstable eigenmode for $q = 4.0/d$ (table 5.2b), also depicted in the solution trajectory connecting the unstable ISR of $q = 4.0/d$ to the stable ISR of $q = 3.16/d$ in figure 5.13(b). Figure 5.15(a) shows the contribution of modal energy from each Fourier z component. From $t = 5 - 10$, the system experiences an exponential growth, guided by its dominant secondary eigenmode $\hat{\mathbf{s}}_{\beta=0.50}$, where the 8 rolls ISRs 'disintegrates' into a convection pattern characterised by a symmetric 'D' convection pattern. Finally, the system stabilises into an ISR state with wavenumber $q = 3.16/d$.

Figure 5.16 presents the asymptotic behaviour with the most unstable eigenmode for $q = 4.5$ (table 5.2(c)), corresponding to the connection between the unstable ISR ($q = 4.5/d$) and the stable ISR ($q = 3/d$) in figure 5.13(c). Figure 5.16(a) shows the contribution of modal energy

Figure 5.14: Asymptotic behaviour of the linear instability ($\hat{\mathbf{q}}_{\beta=0.50}$) about unstable ISR $q = 3.5/d$. (a) Modal energy $E_k(t)$, and temperature snapshots, $\theta(x,z)|_{y=d/2}$ at (b) $t = 33$, (c) $t = 48.5$, (d) $t = 60$.

Figure 5.15: Asymptotic behaviour along the linear instability $\hat{\mathbf{s}}_{\beta=0.50}$ about unstable ISR $q = 4.0/d$. (a) Modal energy $E_k(t)$, and temperature snapshots, $\theta(x,z)|_{y=d/2}$ at (b) $t = 5$, (c) $t = 10.5$, (d) $t = 12.5$.

from each Fourier z component. Initially, the system begins as an ISR state of 9 rolls ($t = 1.25$). Next, the secondary eigenmode $\hat{\mathbf{s}}_{\beta=0.75}$ grows exponentially and peaks at $t = 4.50$, leading to an intermediate state characterised by a symmetric 'O' convection rolls with small $dE_k(t)/dt$ (fig 5.16(c)). Finally, the system evolved into an ISR state of $q = 3/d$ as an asymptotic state.
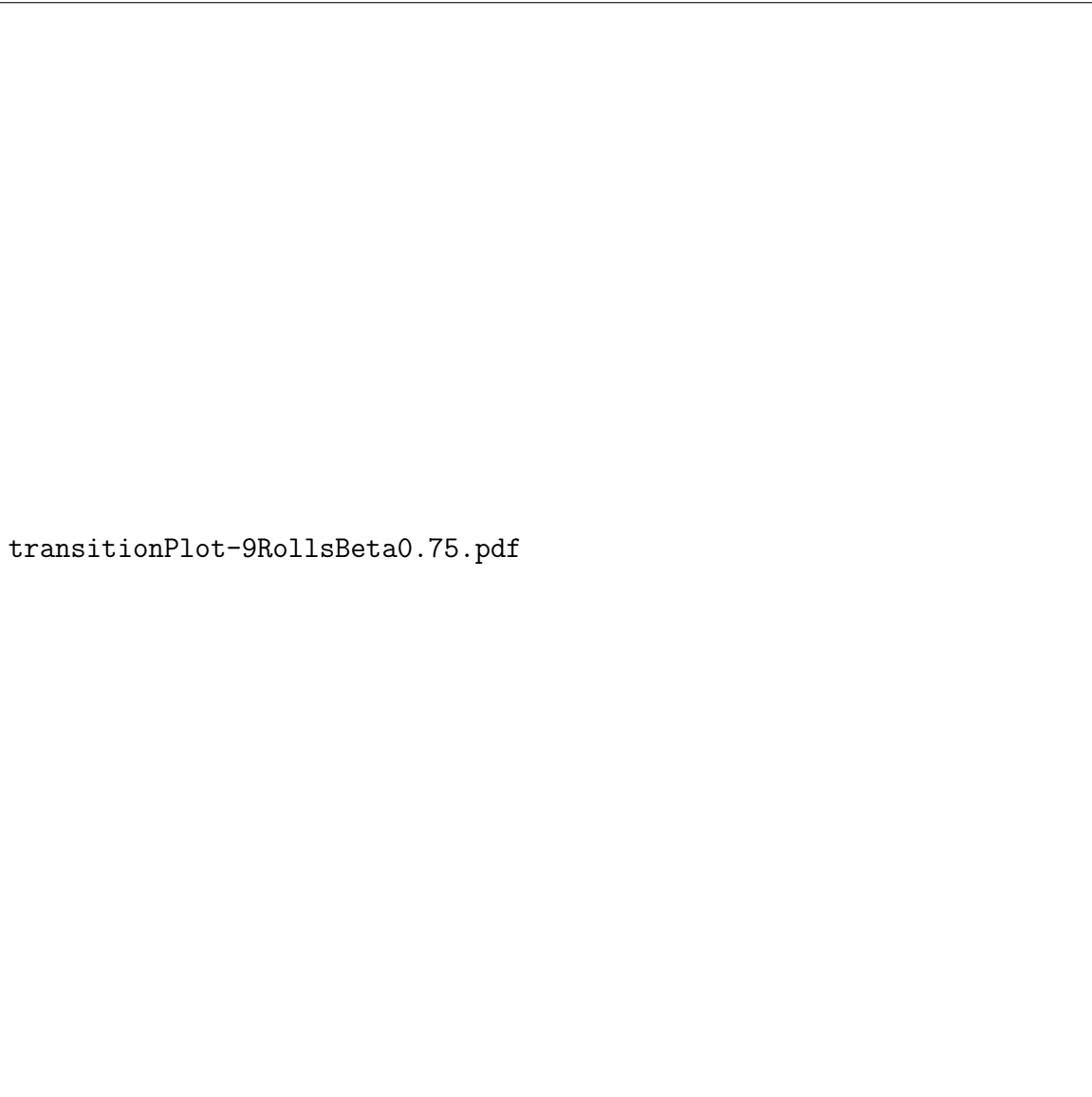
All three cases examined here show that the transition from an unstable ISR to a stable ISR involves an intermediate state, at which $dE_k(t)/dt$ is seen to be relatively small. In the transition pathway from the unstable to stable ISR, it is presumable that there exists an unstable equilibrium (i.e. fixed point/travelling-waves etc.) in the form of the original unstable ISR with its nonlinearly saturated instability, or ghost states **?**. The existence of such a stationary solution can probably be computed with a typical Newton iteration or variational methods [**??**], but this is beyond the scope of the present study. In any case, the numerical experiments here suggest that each of the stable ISR has a basin of attraction composed of a network of heteroclinic orbits involving connections between the base state and unstable ISRs.

5.5.2 Pathways leading to elementary states

Now, we discuss the asymptotic behaviour with linear instabilities of $\hat{\mathbf{s}}_{\beta=1.25}$ and $\hat{\mathbf{s}}_{\beta=1.75}$ about the unstable ISR of $q = 4.5/d$ (tab 5.2(d,e)). Contrary to the transitions presented in the previous section, the asymptotic states did not result in ISRs, but transient SDC before settling into an elementary state for case (e) (table 5.2(e)), and an elementary directly for case (d) (table 5.2(d)). The asymptotic behavior with $\hat{\mathbf{s}}_{\beta=1.25}$ for unstable ISR $q = 4.5/d$ (table 5.2(d)) is presented in figure 5.17. At $t = 1.25$, the unstable ISR state ($q = 4.5/d$) is characterised by 9 rolls aligned along x direction. Subsequently, the state experiences the linear instability triggered ($t = 5$, figure 5.17(c)), shown as an exponential growth of the brown curve figure 5.17(a)), corresponding to the fifth Fourier modal energy (or $\beta = 1.25$). At $t = 6.75$, the system transitions into a saturated state temporarily (albeit unstable), characterised by square-like alternating convection patterns (figure 5.17(d)), and saturates briefly at $t = 8.75$, forming 'S'-like convection patterns in figure 5.17(e). Finally, it settles into an oscillatory elementary state (i.e. stable periodic orbit) with an oscillation period of $T \approx 3.25$ (figures 5.17(f,g)).

The asymptotic behavior with $\hat{\mathbf{s}}_{\beta=1.75}$ of unstable ISR $q = 4.5/d$ (table 5.2(e)) is presented in figure 5.18. Starting from $t = 1.25$, the unstable ISR state is characterised by 9 convection rolls aligned along the x-axis. The state experiences the linear instability imposed from $t = 1.25$ to $t = 7$, corresponding to an exponential growth in the grey curve ($E_7(t)$ in figure 5.18(a)), marked by cross-convection rolls in figure 5.18(c). Subsequently, the state exhibits a transient SDC behaviour from $t \approx 7$ to $t \approx 80$, characterised by an 'O'-ring and 'pac-man' liked convection pattern illustrated in figure 5.18(d). Following this, the system stabilises into a short-period ($T \approx 1.8$) oscillatory behaviour between $t = 90$ and $t = 110$ (figure 5.18(e)), before transitioning into a long-period time-periodic state from $t = 110$ to $t = 201.75$ (figure 5.18(a) *cont.*), with a period of $T = 51.75$. The convection pattern appears to be travelling diagonally in the negative x-z directions (compare figures 5.18(f,g)), indicating that this state is a relative periodic orbit.

Figure 5.19 presents the state space trajectories of two pathways discussed above, rep-

Figure 5.16: Asymptotic behaviour along the linear instability of $\hat{\mathbf{s}}_{\beta=0.75}$ about unstable ISR of $q = 4.5/d$. (a) Modal energy $E_k(t)$, and temperature snapshots, $\theta(x,z)|_{y=d/2}$ at (b) $t = 1.25$, (c) $t = 4.50$, (d) $t = 8.75$.

Figure 5.17: Asymptotic behaviour along the unstable manifold of $q = 4.5/d, \beta = 1.25$. (a) Modal energy $E_k(t)$ plot, and temperature snapshots $\theta(x, z)|_{y=d/2}$ at (b) $t = 1.25$, (c) $t = 5$, (d) $t = 6.75$, (e) $t = 8.75$, (f) $t = 21.75$ and (g) $t = 25$

resented by the volume-normalised L2-norms of velocity perturbations, temperature perturbations and Nusselt number. These trajectories are superimposed upon the state space trajectories of SDC (figures 5.1(a,b)), elementary states (figures 5.1(c-f)) and the fixed-point attractors of ISRs (figure 5.4). The purple trajectory represents the one along the linear instability direction (i.e. the unstable manifold) of $q = 4.5/d$ with $\beta = 1.25$. Originating from the unstable ISR ($q = 4.5/d$), briefly saturates at $||\frac{1}{V}\tilde{\mathbf{u}}|| \approx 6.25$ and $||\frac{1}{V}RaPr\tilde{\theta}||_2 \approx 8$, before stabilising into a periodic orbit near the *spiral-defect* elementary state (see figure 5.1, represented by the orange trajectory in figure 5.4. The case of $q = 4.5/d$ along the linear instability direction for $\beta = 1.75$ is represented by the brown trajectory. Emanating from the unstable ISR ($q = 4.5/d$), the trajectory experiences a period of transient SDC behaviour in the vicinity of elementary states before converging onto a relative periodic orbit, as expected from figure 5.18. It is evident that the two trajectories arising from linear instabilities about the unstable ISR ($q = 4.5/d$) lie within the vicinity of SDC.

5.5.3   A pathway to SDC in an extended domain $\Gamma = 4\pi$

In §5.5.2, we have identified two distinct pathways to elementary states along some unstable manifolds from an unstable ISR. In particular, one of the trajectories evolved into transient SDC before stabilising into an elementary state. This is reminiscent of a chaotic saddle, but with a considerably short lifetime. The transient SDC behaviour observed within the minimal domain implies that if the same initial condition is added in an extended computational domain, it would trigger a chaotic state at least with a longer lifetime. This chaotic state is expected to be SDC in an extended domain, given the analysis in §5.5.2. To examine this hypothesis, we conduct a numerical simulation with an initial condition from the case of table 5.2(e) (i.e. the unstable ISR $q = 4.5/d$ with the instability mode of $\hat{\mathbf{s}}_{\beta=1.75}$) in a domain twice larger than each horizontal direction ($\Gamma = 12.58$).

The solution trajectory along the unstable manifold, $\mathbf{s}_{\beta=1.75}$, of ISR $q = 4.5/d$ in an extended domain ($\Gamma = 4\pi$) is presented in figure 5.20. The state, characterised by 18 convection rolls (figure 5.20(b)), experiences the linear instability from $t = 1.25$ to $t = 7$, marked by cross-convection rolls shown in figure 5.20(c). Subsequently, the state exhibits a prolonged period of chaotic behaviour, starting from $t = 7$ and lasting beyond $t = 200$. This is in stark contrast to the transient SDC behaviour observed in the minimal domain (figure 5.18), confirming the hypothesis above. Finally, it is interesting to note that the convection patterns of figures 5.20(f,g) contain localised structures that bear resemblance with the stationary *pac-man* (figure 5.1)(c)) and oscillatory *peanut* (figure 5.1(f)) elementary states.
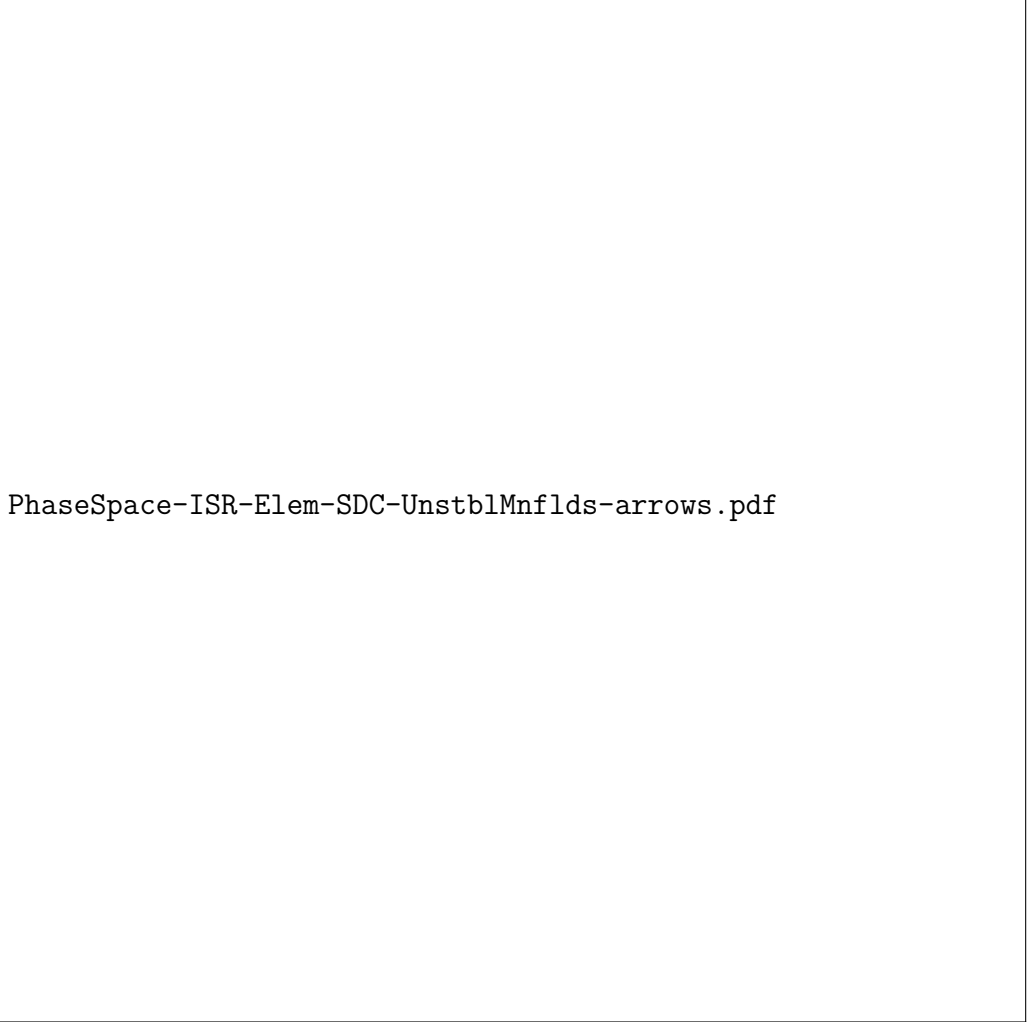
5.6   Concluding remarks

SDC has been considered one of the bistable states within a large spatial domain in Rayleigh-Bénard convection. However, existing studies have also shown the presence of multiple stable states in small and large domains, puzzling one's understanding of the bistable system in an

Figure 5.18: Asymptotic behaviour along the linear instability of $\hat{\mathbf{s}}_{\beta=1.75}$ about unstable ISR $q = 4.5/d$. (a) Modal energy $E_k(t)$, and temperature snapshots $\theta(x,z)|_{y=d/2}$ at the onset of secondary instability at (b) $t = 1.25$, (c) $t = 7$, following a transient SDC behaviour at (d) $t = 40$, and settling into a elementary state at (e) $t = 100$, (f) $t = 150$ and (g) $t = 201.75$.

Figure 5.19: State space visualisations using (a) $||\frac{1}{V}\tilde{\mathbf{u}}||_2$ and $||\frac{1}{V}RaPr\tilde{\theta}||_2$, for SDC shown in figure 5.1(a,b), 4 elementary states shown in figures 5.1(c-f), linear instabilities (purple) $\hat{\mathbf{s}}_{\beta=1.25}$, (brown) $\hat{\mathbf{s}}_{\beta=1.75}$ about an unstable ISR $q = 4.5/d$ (figures 5.17, 5.18), and stable fixed-points of ISRs for wavenumber $q \in (2.0/d, 3.35/d)$ with the magnitude of q is depicted by the opacity of the filled symbol ($\bullet$), with arrows denoting direction of increasing q. Figure (b) is a magnified plot of (a).

Figure 5.20: Asymptotic behaviour along the linear instability $\hat{\mathbf{s}}_{\beta=1.75}$ about unstable ISR $q = 4.50/d$, in an extended domain $\Gamma = 4\pi$. (a) Modal energy $E_k(t)$, and temperature snapshots $\theta(x, z)|_{y=d/2}$, at (b) $t = 1.25$, (c) $t = 7$, (d) $t = 40$, (e) $t = 100$, (f) $t = 125$, (g) $t = 150$.

Figure 5.21: State space sketch containing the base, stable and unstable ISRs, edge, elementary states and SDC in a confined domain. Open circles, (○) and filled circles/squares (●, ■) refer to unstable and stable states. Solid (−) and dashed lines (−−) are the solution trajectories along the primary and secondary instabilities respectively, $\lambda_{max}^{Pri,Sec}$ refers to the most unstable primary and secondary linear instability manifolds. Blue, orange and green trajectories denote heteroclinic connections leading toward stable ISRs (trajectories labelled (A-G) and colors adapted from figure 5.13). Dashed-dotted trajectories (− · −) refer to solution trajectories emerging from the edge states (color-coded from figure 5.11). The dotted line (· · ·) represents the boundary between ISRs and SDC, consisting of many stable elementary states.

extended spatial domain. Starting with numerical simulation in an extended domain ($\Gamma = 8\pi$), we have systematically reduced the computational domain, such that the fundamental patterns of SDC can be isolated. Through numerical experiments confined within a minimal domain of $\Gamma = 2\pi$, we have identified transient SDC before stabilising into a stable elementary states of SDC, and 14 different elementary states have been found in this way. From the conventional view of turbulence in shear flow, chaotic trajectories (representing turbulence) are expected to visit a set of unstable invariant solutions before eventually decaying to the base (laminar) state. However, in contrast to this expectation, the solution trajectory, once tangled into SDC stabilises into an non-trivial elementary state instead of returning to the base (ISR) state **??**. This finding is new and challenges the understanding of transition from a dynamical system viewpoint. Despite this, the elementary states are still situated around the chaotic trajectories of SDC in the state space (figure 5.4), and their statistical properties (figure 5.5) are remarkably similar to those of SDC. This suggests that the computed elementary states may serve as 'building block' structures of SDC that interact with each other to form SDC in an extended domain.

To further understand the state space structure of SDC, ISRs and possible gateways toward SDC, we furnish a state space sketch of the solution trajectories connecting the base, stable and unstable ISRs, edge, elementary states and SDC, shown in figure 5.21. Starting from the base state, time-integrating along the unstable manifold guided by primary instabilities leads to either stable or unstable ISRs, denoted by solid trajectories. Notably, the most unstable primary instability leads to a 7 roll ISR ($q = 3.5/d$), before saturating into a stable 5 roll ISR ($q = 2.5/d$), following the most unstable secondary instability, depicted by dashed trajectories. These solution trajectories form a network of heteroclinic orbits, connecting the base state with stable ($q = 2.5/d$) and unstable ($q = 3.5/d, 5/d$) ISRs, represented in blue. Further from the boundaries of the Busse balloon, we have identified two more heteroclinic orbits that form a basin of attractor between the base state, and stable, unstable ISRs, labelled as a group of orange and green trajectories. These heteroclinic orbits are expected in experimental settings where initial conditions and background noise can be controlled precisely. In practice, where precise controls are inaccessible, it is more likely to observe SDC ($\Gamma = 4\pi, 8\pi$) or stable elementary states ($\Gamma = 2\pi$), which are embedded in the chaotic trajectories of SDC (see coloured ■), supporting the notion that SDC is underpinned by elementary states presumably interacting with each other. By examining the edge states between stable ISRs and elementary states, we have identified 4 edge states that lie on the boundary between stable ISRs and transient SDC, where the upper and lower trajectories emerging from their unstable manifold are represented by dash-dotted trajectories. Further from the Busse balloon, we have identified an unstable manifold of a 9 roll ($q = 4.5/d$) ISR, leading to the onset of SDC. Consequently, the unstable base state is also expected to lie on the boundary, as a controlled initial condition could guide the system toward the unstable 9-roll ISR, and subsequently the onset of SDC. Finally, the dotted line represents the boundary between ISRs and SDC, consisting of the base state, edge states and unstable 9 roll ISR ($q = 4.5/d$), illustrating four possible routes toward SDC. Although

we have considered the unstable manifolds of ISRs for $\Gamma = 2\pi$, we acknowledge that the dimension of such manifolds depends on the domain size and that the presence of spatially subharmonic instabilities may arise as the domain size increases. Additionally, there may well be other unstable ISRs and edge states along the boundary. However, the investigation into the existence of such states is challenging due to the daunting computational efforts required. Recent advances, such as the framework proposed in **?**, may help to accelerate linear stability analysis and facilitate further investigations.

Chapter 6

Conclusions

Appendix A

Appendices

A.1 Governing equations for Rayleigh-Bénard convection

The governing equations for Rayleigh-Bénard convection are the non-dimensionalised equations with the Boussinesq approximation for buoyancy-driven flow, given by

$$\frac{\partial \mathbf{u}}{\partial t} + (\mathbf{u} \cdot \nabla)\mathbf{u} = -\nabla p + Pr\nabla^2\mathbf{u} + \frac{RaPr}{8}\theta\mathbf{j}, \qquad (A.1a)$$

$$\frac{\partial \theta}{\partial t} + (\mathbf{u} \cdot \nabla)\theta = \nabla^2\theta, \qquad (A.1b)$$

$$\nabla \cdot \mathbf{u} = 0, \qquad (A.1c)$$

subjected to the following boundary conditions at the walls,

$$\mathbf{u}|_{y=\pm h} = 0, \quad \theta|_{y=-h} = 1, \quad \theta|_{y=h} = 0, \qquad (A.2a)$$

and the periodic boundary conditions imposed in the planar x and z directions. Here, t denotes the time scaled by the vertical thermal diffusion time, d^2/κ, and $\mathbf{x}(= (x, y, z))$ represents the spatial coordinates non-dimensionalised by depth, d. The horizontal directions are x and z, while y is the vertical direction. The velocity vector is given by $\mathbf{u}(= (u, v, w))$ and is scaled by thermal velocity, κ/d, p. The pressure is scaled by $\rho\kappa^2/d^2$, while $\theta(\equiv (T - T_U)/\Delta T)$ refers to the non-dimensional temperature with T being the absolute temperature, and $\mathbf{j}$ denotes the unit vector in y-direction. The Rayleigh number Ra, and the Prandtl number, Pr, are defined as in §**??**. In this study, we set $Pr = 1$.

Ra	Re	N_z	dt	T	$\frac{d}{\kappa}$
0	1050	64	0.1	8000	-
0	2000	128	0.02	3000	-
2000	0	64	0.05	50	25
2000	0.1	64	0.005	5	25
2000	1	64	0.01	50	25
2000	10	64	0.05	50	2.5
2000	100	64	0.1	50	0.25
2000	500	64	0.1	50	0.05
2000	750	64	0.1	50	0.033
2000	1000	64	0.1	50	0.025
2000	1050	64	0.1	8000	3.81
2000	2000	128	0.02	2800	0.75
3000	0	64	0.05	3000	1500
3000	0.1	64	0.005	300	1500
3000	1	64	0.05	100	50
3000	10	64	0.05	50	2.5
3000	100	64	0.1	10000	50
3000	500	64	0.1	50	0.05
3000	750	64	0.1	50	0.033
3000	1000	64	0.1	50	0.025
3000	1050	64	0.1	8000	3.81
3000	2000	128	0.02	2800	0.75
5000	0	64	0.005	1200	600
5000	0.1	64	0.001	800	4000
5000	1	64	0.01	2500	1250
5000	10	64	0.05	500	25
5000	100	64	0.1	1000	5
5000	500	64	0.05	8000	8
5000	750	64	0.05	8000	5.33
5000	1000	64	0.02	8000	4
5000	1050	64	0.02	8000	3.81
5000	2000	128	0.02	2800	0.75
8000	0	64	0.0025	600	300
8000	0.1	64	0.0005	600	3000
8000	1	64	0.005	600	300
8000	10	64	0.05	500	25
8000	100	64	0.1	5000	25
8000	500	64	0.05	10000	10
8000	750	64	0.05	8000	5.33
8000	1000	64	0.02	8000	4
8000	1050	64	0.02	8000	3.81
8000	2000	128	0.02	2800	0.75
10000	0	64	0.0025	1000	500
10000	0.1	64	0.00025	800	4000
10000	1	64	0.0025	600	300
10000	10	64	0.05	12000	600
10000	100	64	0.1	8000	40
10000	500	64	0.05	8000	8
10000	750	64	0.05	8000	5.33
10000	1000	64	0.02	8000	4
10000	1050	64	0.02	8000	3.81
10000	2000	128	0.02	2800	0.75

Table A.1: The summary of the spatial and temporal resolution for a given Re, Ra. N_z denotes

A.2 Simulation parameters for Ra-Re sweep

The spectral/hp quadrilateral element width, heights and polynomial order are kept constant for all simulations, $(\Delta x, \Delta y|_{y=\pm h}, \Delta y|_{y=0}, P) = (0.1\pi, 0.0549, 0.367, 4)$. To resolve the high gradients, the quadrilateral element heights are bunched near the wall, $\Delta y|_{y=\pm h}$, and expanded in the channel center, $\Delta y|_{y=0}$. The basis type employed here consists of the modified Jacobi polynomials, known as the *modified* basis [**?**]. Table A.1 describes the number of Fourier expansions, N_z, and temporal resolution of 52 numerical experiments at $Re = 0, 0.1, 1, 10, 100, 500, 750, 1000, 1050, 2000$, and $Ra = 0, 2000, 3000, 5000, 8000, 10000$ with $Pr = 1$ and a large aspect ratio, $\Gamma = 4\pi$. The initial conditions of all numerical experiments were sampled from a statistically stationary solution based on the time history of the Nusselt number and shear. The laminar solution obtained for $Ra = 0$, $Re \leq 1000$ has been omitted in table A.1.

A.3 First- and second-order statistics of the buoyancy- and shear-driven regime

A.3.1 Buoyancy-driven regime

We present the first- and second-order statistics of the buoyancy-dominated regime (shaded in red), consisting of the (1) SDC & ISRs, and (2) ISRs states in figure A.1, illustrating its temporal and plane-averaged streamwise velocity, $\langle w \rangle_{x,z,t}$, temperature, $\langle \theta \rangle_{x,z,t}$, fluctuating wall-normal velocity squared normalised by thermal velocity scale, $\langle \tilde{v}\tilde{v} \rangle_{x,z,t}/u_\kappa^2$, fluctuating temperature squared, $\langle \tilde{\theta}\tilde{\theta} \rangle_{x,z,t}$ and fluctuating span- and streamwise velocities squared normalised by thermal velocity scale, $\langle \tilde{u}\tilde{u} + \tilde{w}\tilde{w} \rangle_{x,z,t}/u_\kappa^2$. We note that the fluctuating components are defined about a temporal-planar averaged quantity, i.e $\tilde{\mathbf{u}} = \mathbf{u} - \langle \mathbf{u} \rangle_{x,z,t}$. The mean temperature profiles (figure A.1(b)), and the fluctuating span- and streamwise velocities (figure A.1(f)) are visually similar for the same Ra, and are nearly independent of Re. However, we observe the dependence on Re at $Ra = 3000$ in the fluctuating temperature squared (figure A.1(d)), and fluctuating wall-normal velocities (figure A.1(c)), likely due to variations in convection structures, particularly in the convection roll wavenumbers. A detailed analysis of how the statistical properties vary with roll wavenumber is beyond the scope of this work. We propose that the underlying flow structure, consisting of convection rolls, describes the buoyancy-driven regime, shaded in red in figure 4.1. In this regime, the strength of the convection is primarily controlled by Ra, akin to RBC, and remains independent of Re.

A.3.2 Shear-driven regime

As Re falls within the range of $1050 \leq Re \leq 2000$, shear-driven turbulence dominates, where the impact of Ra on the first- and second-order statistics is weakly dependent on Ra in figure A.2. Figure A.2 describes the temporal and plane-averaged streamwise velocity, $\langle w \rangle_{x,z,t}$, tempera-

Figure A.1: The wall-normal distribution of temporal and plane- averaged (a) streamwise velocity, (b) temperature, (c) fluctuating wall-normal velocity squared normalised by thermal velocity scale, (d) fluctuating temperature squared and (e) fluctuating span- and streamwise velocities squared normalised by thermal velocity scale of buoyancy-driven regime shaded in red in figure 4.1.

Figure A.2: The wall-normal distribution of temporal and plane- averaged (a) streamwise velocity, (b) temperature, (c) fluctuating streamwise velocity squared, (d) fluctuating wall-normal velocity squared, (e) fluctuating spanwise velocities squared, (f) fluctuating Reynolds stresses and (g) fluctuating temperature squared in the shear-driven regime shaded in blue in figure 4.1.

ture, $\langle\theta\rangle_{x,z,t}$, fluctuating streamwise velocity squared, $\langle\tilde{w}\tilde{w}\rangle_{x,z,t}$, fluctuating wall-normal velocity squared, $\langle\tilde{v}\tilde{v}\rangle_{x,z,t}$, fluctuating spanwise velocities squared, $\langle\tilde{u}\tilde{u}\rangle_{x,z,t}$, fluctuating Reynolds stresses $\langle\tilde{v}\tilde{w}\rangle_{x,z,t}$, and fluctuating temperature squared, $\langle\tilde{\theta}\tilde{\theta}\rangle_{x,z,t}$ at $Re = 2000, 1050$ for $Ra \in [0, 10000]$. The flow structures appear as uniform, featureless turbulence [?] at $Re = 2000$, independent of Ra. The spacetime figure of near-wall ($y^+ = 15$), wall-normal and spanwise perturbation kinetic energy, $\mathcal{E}_{u'+v'}$, at $Re = 2000$, $t \in [0, 2800]$, illustrating spatially uniform featureless turbulence, visually distinguishable withn $Ra \in [0, 10000]$, corroborating with their Ra-independent first- and second-order statistics in figure A.2. In other words, the dominant physical mechanism is shear-driven turbulence at $Re = 2000$, independent of Ra.

As Re approaches $Re = 1050$, the midplane temperature in figure 4.1 shows regions of spatially localised structures, indicating the presence of turbulent-laminar bands, described in figure 4.3 and 4.4 later. The mean streamwise velocity and temperature gradients at both ends of the wall, and second-order statistics, are enhanced slightly from $Ra = 0$ to $Ra = 10000$. This enhancement could be due to the coexistence of longitudinal rolls with turbulent bands at $Ra = 10000$, discussed in §4.3.3. Notably, we have also included the statistics for a subcritical case ($Ra < Ra_{\parallel}$) at $Ra = 1000$, indicating the presence of subcritical effects as the statistics are slightly enhanced from $Ra = 0$ to $Ra = 1000$, reported by ?. Nonetheless, there is a distinct change of state between $Re = 1000$ to 1050 (see figure 4.1), marked by the transition from the longitudinal/intermittent roll regime to shear-driven turbulence at $Re \geq 1050$, thus, shaded in blue in figure 4.1.

A.4 Growth rates of primary instabilities

Figure A.4 shows the eigenvalues of the primary instabilities as a function of its spanwise wavenumber αd, leading to the onset of longitudinal rolls at $Re = 1050$. The results are obtained using a Chebyshev-collocation method discretised by 51 Chebyshev polynomials [?]. The crosses denote the spanwise wavenumbers admissible within the domain $\Gamma = \pi/2$, where $\alpha d = 4$ corresponds to the dominant eigenmode.

A.5 Verification of linear stability analysis

Figure A.5 shows the eigenvalues as a function of spanwise wavenumber β of RBC at $\varepsilon = 0.7$. The results are obtained using Nektar++ and compared against a Chebyshev-collocation method discretised by 101 Chebyshev polynomials ?.

A.6 Other elementary states and ISRs

Figure A.6 presents snapshots of temperature slices $(\theta(x, z)|_{d/2})$, depicting ten distinct elementary states. These states are obtained within a minimal domain $\Gamma = 2\pi$, consisting of eight stationary states (figures A.6(a-h)) and two travelling-wave states (figures A.6(i,j)). Figure A.7

Figure A.3: Spacetime plots of near-wall, wall-normal and spanwise perturbation kinetic energy for $Re = 2000$, $t \in [0, 2800]$, $\Gamma = 4\pi$ at (a) $Ra = 10000$, (b) $Ra = 8000$, (c) $Ra = 5000$, (d) $Ra = 3000$, (e) $Ra = 2000$, (f) $Ra = 0$.

Figure A.4: Growth rates of primary instabilities at $Ra = 10000, 8000, 5000, 3000, 2000$ leading to the onset of longitudinal rolls against spanwise wavenumber of αd at $Re = 1050$.
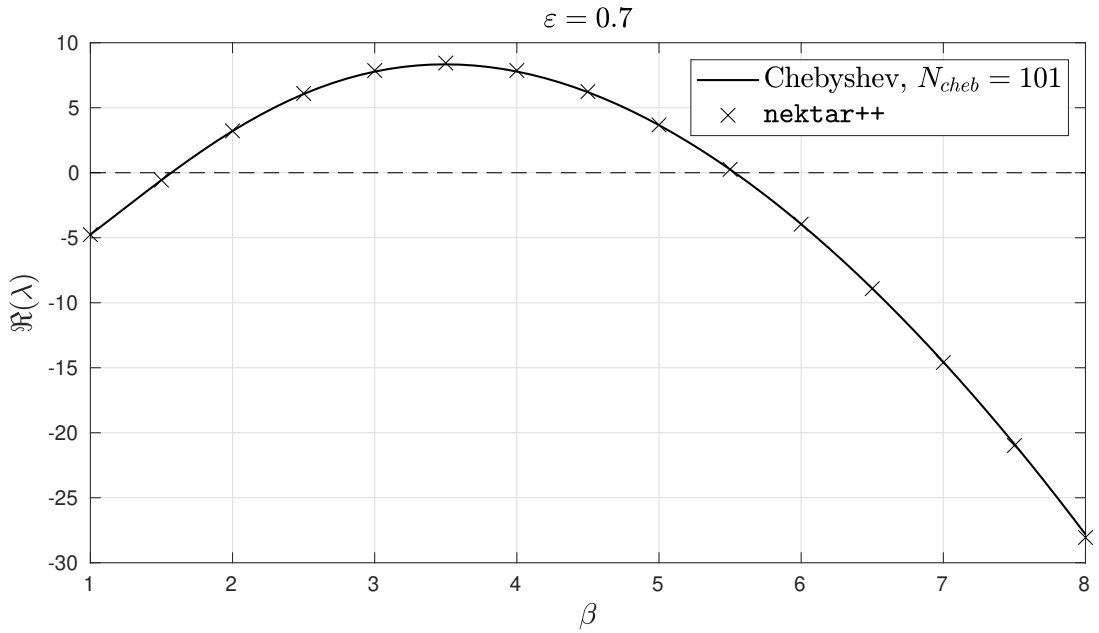
Figure A.5: Eigenvalues of primary instabilities of RBC at $\varepsilon = 0.7$ computed in Nektar++ compared against a Chebyshev-collocation method with 101 Chebyshev expansions.

features a snapshot of fourteen ideal straight rolls (ISRs), and they satisfy rotational symmetry about the y-axis and mirror symmetries about the x- and z-axes due to the horizontal isotropy of the present system. These ISRs represent stable fixed-points in the state space of figures 5.3, 5.4, 5.11, 5.19.

Figure A.6: Temperature snapshots, $\theta(x,z)|_{y=d/2}$, of 10 elementary states confined within a minimal domain $\Gamma = 2\pi$: (a) steady 'forked-A' state, (b) steady 'forked-B' state, (c) steady 'forked-c' state, (d) steady 'twin-armed' state, (e) steady 'tri-rolls' state, (f) travelling-wave 'O-a' state, (g) travelling-wave 'O-b' state, (h) steady 'keyhole' state, (i) relative periodic orbit 'eye' state, (j) relative periodic orbit 'S' state

Figure A.7: Temperature snapshots, $\theta(x,z)|_{y=d/2}$, of 14 stable ideal straight rolls (ISRs) confined within a minimal domain, $\Gamma = 6.28$. Plots (a-n) are ordered in increasing wavenumbers, $q \in (2/d, 3.35/d)$.

Bibliography

Henri Bénard. Les tourbillons cellulaires dans une nappe liquide. - Méthodes optiques d'observation et d'enregistrement. *Journal de Physique Théorique et Appliquée*, 10(1): 254–266, 1901. ISSN 0368-3893. doi: 10.1051/jphystap:0190100100025400. URL http://www.edpsciences.org/10.1051/jphystap:0190100100025400.

Greg Evans and Ralph Greif. Unsteady three-dimensional mixed convection in a heated horizontal channel with applications to chemical vapor deposition. *International Journal of Heat and Mass Transfer*, 34(8):2039–2051, August 1991. ISSN 00179310. doi: 10.1016/0017-9310(91)90215-Z. URL https://linkinghub.elsevier.com/retrieve/pii/001793109190215Z.

Fatin Bazilah Fauzi, Edhuan Ismail, Mohd Hanafi Ani, Syed Noh Syed Abu Bakar, Mohd Ambri Mohamed, Burhanuddin Yeop Majlis, Muhamad Faiz Md Din, and Mohd Asyadi Azam Mohd Abid. A critical review of the effects of fluid dynamics on graphene growth in atmospheric pressure chemical vapor deposition. *Journal of Materials Research*, 33(9): 1088–1108, May 2018. ISSN 0884-2914, 2044-5326. doi: 10.1557/jmr.2018.39. URL http://link.springer.com/10.1557/jmr.2018.39.

Klavs F. Jensen, Erik O. Einset, and Dimitrios I. Fotiadis. Flow Phenomena in Chemical Vapor Deposition of Thin Films. *Annual Review of Fluid Mechanics*, 23(1):197–232, January 1991. ISSN 0066-4189, 1545-4479. doi: 10.1146/annurev.fl.23.010191.001213. URL https://www.annualreviews.org/doi/10.1146/annurev.fl.23.010191.001213.

K.J. Kennedy and A. Zebib. Combined free and forced convection between horizontal parallel planes: some case studies. *International Journal of Heat and Mass Transfer*, 26(3):471–474, March 1983. ISSN 00179310. doi: 10.1016/0017-9310(83)90052-2. URL https://linkinghub.elsevier.com/retrieve/pii/0017931083900522.

Subhashis Ray and J. Srinivasan. Analysis of conjugate laminar mixed convection cooling in a shrouded array of electronic components. *International Journal of Heat and Mass Transfer*, 35(4):815–822, April 1992. ISSN 00179310. doi: 10.1016/0017-9310(92)90249-R. URL https://linkinghub.elsevier.com/retrieve/pii/001793109290249R.

Lord Rayleigh. LIX. *On convection currents in a horizontal layer of fluid, when the higher temperature is on the under side. The London, Edinburgh, and Dublin Philosophical Magazine and Journal of Science*, 32(192):529–546, December 1916. ISSN 1941-5982, 1941-

5990. doi: 10.1080/14786441608635602. URL https://www.tandfonline.com/doi/full/10.1080/14786441608635602.